UNIVERSITÀ
DEGLI STUDI
DELL'AQUILA

DSFC
Dipartimento
di Scienze Fisiche
e Chimiche

UNIVERSITÀ DEGLI STUDI DELL'AQUILA

Dipartimento di Scienze Fisiche e Chimiche

Dottorato di Ricerca in Fisica
XXXVIII ciclo

Numerical modelling of dark matter-admixed compact objects

Lorenzo Cipriani

Supervisor
Prof. Fabrizio Nesti

Coordinator
Prof. Massimiliano Aschi

Academic Year 2024/2025

Table of Contents

Abstract

This thesis explores how dark matter might reveal itself through the structure and dynamics of compact stars. A unified framework in which ordinary matter and a self-interacting dark component coexist inside the same star is developed, influencing each other only through gravity. Within this setting three connected problems are studied: compact objects made entirely of dark matter; rapidly rotating neutron stars that contain a dark component; and differentially rotating remnants that resemble the aftermath of neutron-star mergers.

Methodologically, the work extends the RNS code to handle two fluids that can rotate differently. This allows a systematic scan of plausible configurations and a clean comparison with standard one-fluid neutron star models. Even modest amounts of dark matter can shift global stellar properties in ways that resemble changes in the nuclear equation of state. Mass-radius relations, tidal deformability, and moments of inertia are all affected, and the imprint depends on how the dark component is distributed and rotates. These trends create degeneracies that single measurements cannot resolve, but they also open new opportunities: combining gravitational-wave observations, X-ray timing, and late-time post-merger signals offers a realistic path to distinguish dark-matter effects from purely hadronic physics.

Overall, the thesis indicates that allowing for a dark component can be important for obtaining unbiased inferences about dense matter, especially in environments where dark-matter accumulation is plausible. At the same time, compact stars emerge as potential laboratories for the dark sector: by tracing how their observable properties react to a hidden fluid, the results outline targets for future multimessenger searches.

Introduction

The understanding of the microscopic nature of dark matter remains at the forefront of modern physics. Despite its overwhelming presence in the cosmic energy budget, the absence of direct detection has left the fundamental properties of dark matter largely unconstrained. Compact stellar objects, with their extreme densities and multimessenger visibility, provide an ideal environment to probe dark matter physics in a regime far removed from traditional cosmological or collider-based approaches.

Recent multimessenger observations provide a first step in the study of these systems. The discovery of two-solar-mass pulsars sets a robust lower bound on the maximum mass supported by any viable equation of state. X-ray and radio timing missions such as NICER and SKA focus on measuring pulse profiles that translate into radius constraints, directly probing the compactness of neutron stars. Gravitational-wave detections of binary neutron star mergers, most notably GW170817 [1, 2], constrain tidal deformabilities and offer a glimpse of the post-merger dynamics. Together, these measurements define a landscape in which the presence of dark matter may leave subtle but detectable signatures, motivating theoretical explorations across a wide parameter space.

The theoretical framework adopted in this thesis relies on relativistic two-fluid models, in which baryonic matter and dark matter interact solely through gravity. The dark matter is modelled as a self-interacting bosonic fluid, described in the mean-field limit, leading to an equation of state that captures the macroscopic behaviour of a condensed Bose system. Baryonic matter is treated through well-established nuclear physics equations of state consistent with astrophysical constraints. Rotation, a key ingredient in neutron star phenomenology, is incorporated through different laws: uniform rotation for isolated pulsars and differentially rotating profiles appropriate for merger remnants. These models allow for the systematic exploration of

dark matter's role in shaping equilibrium sequences, extending from isolated stars to merger dynamics.

A number of simplifying assumptions guide the analysis. Matter is taken to be at zero temperature, reflecting the thermally relaxed state of old neutron stars. Configurations are assumed to be stationary and axisymmetric, appropriate for equilibrium studies. No direct non-gravitational couplings between dark matter and baryonic matter are included, consistent with current experimental limits. Finally, the focus is on equilibrium sequences rather than dynamical evolution, though comparisons to merger simulations and observations are drawn where appropriate.

The study of compact objects raises several open questions. A fundamental issue is whether self-interacting dark matter can assemble into compact, long-lived equilibrium structures, and under what conditions such configurations would form in the universe. Even when such objects are assumed to exist, uncertainties remain regarding how an embedded dark matter component modifies the internal structure of neutron stars and influences macroscopic observables and the onset of instabilities. An equally pressing problem is disentangling these effects from those due to the baryonic equation of state, which itself remains uncertain at supranuclear densities. Identifying which observational channels can break this degeneracy is central to advancing both astrophysics and particle physics.

This thesis is organized around three major lines of investigation, each corresponding to a published study. The first concerns superfluid dark stars, compact configurations made entirely of self-interacting bosons. Their equilibrium sequences display simple scaling relations between physical parameters, and their tidal deformabilities fall within the reach of next-generation interferometers. Numerical simulations of binary mergers reveal distinctive gravitational-wave signatures, offering a novel observational channel for detecting or constraining such objects.

The second study turns to rapidly rotating neutron stars admixed with dark matter. Millisecond pulsars, with their extreme rotation rates and long evolutionary timescales, are natural laboratories for dark matter accumulation. Here we model two-fluid configurations in which dark matter and baryonic matter rotate independently, allowing for co- and counterrotating scenarios. We investigate how differ-

ent dark matter masses and fractions, in both core and halo distributions, affect macroscopic observables such as the maximum mass, the mass-shedding limit, and the moments of inertia. These results highlight the potential for X-ray timing and gravitational-wave observations to constrain dark matter parameters through their impact on rotational equilibria.

The third work extends this framework to differentially rotating dark matter-admixed neutron stars, which serve as equilibrium proxies for post-merger remnants in binary neutron star coalescences. Using rotation laws that reproduce the profiles observed in numerical relativity simulations, we study how dark matter cores influence the stability, maximum mass, and deformation of differentially rotating configurations. These models provide a theoretical bridge between equilibrium studies and the rich post-merger phenomenology observed in gravitational waves.

The following chapters provide the necessary background and present the main research contributions of this thesis. Chapter 1 introduces the fundamental physics of compact objects in general relativity, covering both spherical and axisymmetric configurations, and includes a brief overview of how baryonic matter equations of state are constructed. Chapter 2 then reviews what is known about dark matter, summarizing the evidence for its existence and highlighting specific models, with particular attention to the advantages and challenges posed by self-interacting dark matter. The core research presented in this work is detailed in Chapters 3 to 5, while Appendix A provides the implementation details of the numerical code used in Chapters 4 and 5.

Chapter 1

Structure and physics of neutron stars

The exploration of the properties of matter at extreme densities, the equation of state, is hindered by both experimental and theoretical challenges.

Experimentally, our knowledge is limited by the maximum densities achievable in laboratory conditions. For instance, heavy-ion collisions at RHIC can reach densities up to $\sim 10^{15}\,\mathrm{g\,cm^{-3}}$, but these conditions are at high temperature and exist only for an extremely short time [3], making it impossible to probe the cold, dense matter found in neutron star (NS) interiors.

Theoretically, a major obstacle is our incomplete understanding of quantum chromodynamics at low energies. At low densities ($\rho \lesssim \rho_{\mathrm{sat}} = 2.68 \times 10^{14}\,\mathrm{g\,cm^{-3}}$), the equation of state is relatively well constrained by nuclear experiments and effective theories such as chiral effective field theory [4]. At very high densities ($\gtrsim 50\rho_{\mathrm{sat}}$), quantum chromodynamics enters the so-called "asymptotic freedom" regime, where perturbative calculations become reliable [5]. In the intermediate range, quantum chromodynamics is strongly interacting, and the equation of state must be modelled using nuclear many-body approaches, either phenomenological or ab initio. This regime contains the densities reached in the cores of neutron stars and represents the most uncertain and model-dependent part of the equation of state. Many physical configurations can be considered: models can include the appearance of new particle species, such as pions or hyperons, as well as phase transitions to deconfined quark matter.

For this reason, neutron stars have proven to be an invaluable natural laboratory for modern physics. Their extreme densities and rich internal composition make them ideal systems to study both nuclear physics and general relativity.

In the following sections, we introduce the theoretical tools necessary to describe them. Section 1.1 briefly introduces neutron stars and describes the textbook prob-

lem of a static self-gravitating perfect fluid and derives the Tolman-Oppenheimer-Volkov (TOV) equations [6, 7]. In light of the requirements of Chapters 4 to 5, we will slightly generalize the derivation to an arbitrary number of perfect fluids. In Section 1.2, we will then describe three equations of state that we will employ to model both baryonic matter and dark matter. Finally, in Section 1.3, we describe rapidly rotating neutron stars in a fully relativistic formalism, discussing the theoretical framework that is later adapted for the numerical approach used in the RNS software, described in Appendix A.

1.1 Essentials of relativistic stellar structure

1.1.1 Neutron stars: formation and phenomenology

Neutron stars are among the most compact and energetic objects in the Universe, second only to black holes. They were first predicted theoretically by Baade and Zwicky in 1934 [8], shortly after the discovery of the neutron by Chadwick [9]. They proposed that these objects would form from the collapse of massive stars, a hypothesis that was confirmed decades later with the discovery of pulsars.

Neutron stars are the remnants of core-collapse supernovae (Type II, Ib, or Ic). When a massive star ($8\,\mathrm{M}_\odot \lesssim M \lesssim 25\,\mathrm{M}_\odot$) [10] exhausts its nuclear fuel, the thermal pressure generated by fusion can no longer support the star against its own gravity. As the core density surpasses nuclear saturation density, protons and electrons merge via inverse beta decay ($p + e^- \to n + \nu_e$) to form a neutron-rich fluid. The inner core eventually stiffens due to the repulsive component of the strong nuclear force and neutron degeneracy pressure, halting the collapse and generating a shockwave that ejects the outer envelope of the star [11].

The resulting proto-neutron star is initially hot ($T \sim 10^{11}\,\mathrm{K}$) [12]. Over a timescale of seconds to minutes, it becomes transparent, releasing nearly 99% of the supernova's binding energy ($\sim 10^{53}\,\mathrm{erg}$) in the form of neutrinos. This cooling phase transitions the object into a cold, stable neutron star. The conservation of angular momentum during the collapse of the progenitor star spins the remnant

up to rotation periods ranging from milliseconds to seconds, while magnetic flux conservation amplifies the magnetic field to intensities of $10^8 \div 10^{15}$ G [13, 14].

Although often approximated as a uniform fluid of neutrons, a neutron star possesses a complex, stratified internal structure [15]. The density spans several orders of magnitude, from $\sim 10^6\,\mathrm{g\,cm^{-3}}$ at the surface to exceeding $10^{15}\,\mathrm{g\,cm^{-3}}$ in the core.

The outermost layer is the *atmosphere*, a thin plasma layer only a few centimetres to meters thick, which shapes the thermal photon spectrum. Below this lies the *crust*, which is divided into an outer and an inner region. The *outer crust* consists of a Coulomb lattice of heavy nuclei (mostly iron-peak elements) embedded in a degenerate electron gas. As the density increases with depth, the electron Fermi energy rises, making electron capture energetically favourable and resulting in increasingly neutron-rich nuclei. At the *neutron drip* density ($\rho_{\mathrm{drip}} \approx 4 \times 10^{11}\,\mathrm{g\,cm^{-3}}$), neutrons begin to leak out of the nuclei, marking the transition to the *inner crust*. Here, a lattice of neutron-rich clusters coexists with a superfluid gas of free neutrons. At the base of the crust, competition between Coulomb repulsion and nuclear attraction may lead to the formation of complex non-spherical nuclear shapes, known as "nuclear pasta" phases [16].

The *core* constitutes approximately 99% of the star's mass. The *outer core* (densities $\rho \sim 0.5\rho_{\mathrm{sat}}$ to $2\rho_{\mathrm{sat}}$, where $\rho_{\mathrm{sat}} \approx 2.8 \times 10^{14}\,\mathrm{g\,cm^{-3}}$ is the nuclear saturation density) is a fluid of neutrons, protons, electrons, and muons in beta-equilibrium. The protons are likely superconducting, while the neutrons are superfluid. The composition of the *inner core* remains one of the greatest open questions in modern physics. Depending on the stiffness of the equation of state, densities may reach 5–10 times ρ_{sat}. Under these extreme conditions, it is hypothesized that exotic degrees of freedom may appear, such as hyperons (Λ, Σ, Ξ), Bose-Einstein condensates of pions or kaons, or a phase transition to deconfined quark matter (up, down, and strange quarks). The presence of these components generally softens the equation of state, reducing the maximum mass the star can support against collapse.

Observational Status Observations of NSs began in 1967 with the discovery of the first pulsar by Jocelyn Bell and Antony Hewish [17]. Pulsars are rapidly rotating,

highly magnetized neutron stars that emit beams of electromagnetic radiation. As the star spins, these beams sweep across the Earth appearing as periodic pulses. Precise timing of these pulses has provided some of the most stringent tests of General Relativity. Notably, the Hulse-Taylor binary (PSR B1913+16) demonstrated orbital decay consistent with the emission of gravitational waves.

Today, we observe neutron stars across the electromagnetic spectrum, from radio to gamma rays. X-ray missions such as NICER (Neutron star Interior Composition Explorer) monitor the thermal emission from hotspots on the surface of rotating pulsars. By modeling the relativistic light-bending effects on these pulse profiles, it is possible to infer both the mass and the radius of the star simultaneously, placing tight constraints on the dense-matter equation of state [18, 19].

Since 2017, the study of neutron stars has entered the multimessenger era. The detection of gravitational waves from the binary neutron star merger GW170817 by the LIGO and Virgo collaborations [2], followed by the observation of its electromagnetic counterpart (a kilonova), provided the first direct measurement of the tidal deformability of neutron stars. This quantity describes how easily a star is deformed by the gravitational field of its companion and is directly related to its radius and internal composition.

Despite these advances, many questions remain. The so-called "hyperon puzzle" (i.e., the difficulty in reconciling the theoretical appearance of hyperons with the observation of massive $\sim 2\,M_\odot$ stars) suggests our understanding of strong interactions is incomplete. Furthermore, the potential existence of dark matter trapped within neutron stars, the central topic of this thesis, offers an intriguing solution to some of these anomalies and a novel probe of the dark sector.

1.1.2 The Tolman-Oppenheimer-Volkov equations

Because neutron stars are compact objects with densities reaching several times that of atomic nuclei, Newtonian gravity is an insufficient description of their gravitational attraction: a fully relativistic treatment is required. In this section, we introduce the essential elements of relativistic stellar structure, starting from the derivation of the

TOV equations for static, self-gravitating fluids.

Throughout this work, unless otherwise specified, we adopt geometrized units such that $G = c = 1$.

The equilibrium configuration results from a balance between the gravitational pull, described by Einstein's equations, and the pressure gradients of each fluid component, determined by the corresponding equation of state.

For the moment, we assume the equation of state is derived from a stress-energy tensor of the form

$$T^{\alpha\beta} = \sum_i T^{\alpha\beta}_{(i)} = \sum_i \left(\varepsilon_i + P_i\right) u_i^\alpha u_i^\beta + P_i g^{\alpha\beta}, \tag{1.1}$$

with

$$P_i = P_i(\varepsilon_i), \tag{1.2}$$

where $i = 1, \ldots, N$ labels the N fluids in the system, P_i is the pressure, ε_i the energy density and u_i^μ the four-velocity of the fluid. This choice of $T_{\alpha\beta}$ imposes a strong constraint: the fluids do not interact with each other, so the conservation equations

$$\nabla_\beta T_i^{\alpha\beta} = 0 \tag{1.3}$$

hold independently for each fluid. Consequently, all energy exchange between the fluids is neglected, and they coexist within the same gravitational well.

We begin by modelling the system as a spherically symmetric distribution of matter. The most general static, spherically symmetric metric that describes this system is

$$\mathrm{d}s^2 = -\,\mathrm{e}^{\nu(r)}\mathrm{d}t^2 + \,\mathrm{e}^{\lambda(r)}\mathrm{d}r^2 + r^2\mathrm{d}\Omega^2, \tag{1.4}$$

where $\mathrm{d}\Omega^2 = \mathrm{d}\theta^2 + \sin^2\theta\mathrm{d}\phi^2$, and $\nu(r)$ and $\lambda(r)$ are functions to be determined from Einstein's equations

$$G^{\alpha\beta} = 8\pi T^{\alpha\beta}. \tag{1.5}$$

Analogously to the standard one-fluid case [6, 7], the relevant Einstein equations reduce to the (t,t) and (r,r) components. Representing derivatives with respect to

r by a prime, the (t,t) component is generally written as

$$\frac{\mathrm{e}^{\nu-\lambda}\left(\mathrm{e}^{\lambda}+\lambda'-1\right)}{r^2}=8\pi\,\mathrm{e}^{\nu}\sum_i\varepsilon_i. \tag{1.6}$$

After straightforward algebra, this can be rewritten as

$$\mathrm{e}^{-\lambda(r)}=1-2\frac{m_{\mathrm{tot}}(r)}{r},\quad m_{\mathrm{tot}}(r)=4\pi\int_0^r \mathrm{d}\tilde{r}\,\tilde{r}^2\sum_i\varepsilon_i(\tilde{r})=\sum_i m_i(r), \tag{1.7}$$

where m_{tot} is the total mass enclosed within a sphere of radius r, considering all fluids. The (r,r) component, in turn, reads

$$\frac{-\mathrm{e}^{-\lambda}+r\nu'+1}{r^2}=8\pi\,\mathrm{e}^{\lambda}\sum_i P_i, \tag{1.8}$$

which can be reformulated, employing Eq. (1.7), as

$$\nu'(r)=\frac{1}{r}\left(1-2\frac{m_{\mathrm{tot}}(r)}{r}\right)^{-1}\left[2\frac{m_{\mathrm{tot}}(r)}{r}+8\pi r^2\sum_i P_i(r)\right]. \tag{1.9}$$

When combined with the continuity equation for each fluid,

$$P_i'=-\frac{1}{2}(P_i+\varepsilon_i)\nu', \tag{1.10}$$

this leads to the multi-fluid generalisation of the TOV equation:

$$P_i'(r)=-\frac{\left[P_i(r)+\varepsilon_i(r)\right]\left[m_{\mathrm{tot}}(r)+4\pi r^3 P_{\mathrm{tot}}(r)\right]}{r\left[r-2m_{\mathrm{tot}}(r)\right]}, \tag{1.11}$$

where again $P_{\mathrm{tot}}=\sum_i P_i$ is the total pressure on a sphere of radius r.

Equation (1.7), coupled with Eq. (1.11) and the equation of state Eq. (1.2) completely closes the system of $2N$ ordinary differential equations. The required initial

conditions at the centre of the star are

$$\begin{cases} m_i(r=0) = 0 \\ P_i(r=0) \ = P_i(\varepsilon_c^i) \end{cases} \tag{1.12}$$

where ε_c^i is a set of input parameters that uniquely determine the solution and represent the central energy density of each fluid. The system is then integrated outwards from the centre using standard numerical techniques, such as the Runge-Kutta method. Integration for each fluid is stopped once its pressure becomes negative; the corresponding matter fields are then set to zero for the remainder of the integration. This procedure effectively defines the outer boundary of that fluid component. Finally, the metric fields are reconstructed from all the matter fields and the spherically symmetric spacetime is fully determined.

Isotropic coordinates Forseeing what will be useful in Appendix A, we will now introduce an alternative formulation of Eqs. (1.7) and (1.11), in which the TOV equations will be rewritten in isotropic coordinates.

Isotropic coordinates are specific kind of coordinate systems in which the metric appears as

$$\mathrm{d}s^2 = -\,\mathrm{e}^{2\phi}\mathrm{d}t^2 + \,\mathrm{e}^{2\Lambda}\left(\mathrm{d}\bar{r}^2 + \bar{r}^2\mathrm{d}\Omega^2\right), \tag{1.13}$$

where $\mathrm{e}^{2\phi}$ plays the role of a lapse function, $\mathrm{e}^{2\Lambda}$ that of a conformal factor and $\bar{r}$ is the isotropic radius. In contrast to the Schwarzschild coordinates, the metric scales the same in all directions and as the name implies is isotropic in the spacial directions.

Isotropic coordinates offer several practical advantages: the spatial metric becomes conformally flat, simplifying the treatment of Einstein's equations; the metric functions remain smooth and well-behaved at the origin and near the stellar surface, avoiding coordinate singularities; and the isotropic radial coordinate allows for uniform angular resolution and straightforward implementation of boundary conditions at infinity. These features together improve the accuracy, stability, and efficiency of numerical solutions for compact stars.

Comparing Eqs. (1.4) and (1.13), it is obvious to match

$$\begin{aligned} r^2 &= \mathrm{e}^{2\Lambda}\bar{r}^2 \\ \mathrm{e}^{\lambda}\mathrm{d}r^2 &= \mathrm{e}^{2\Lambda}\mathrm{d}\bar{r}^2 \end{aligned} \tag{1.14}$$

The former fixes the conformal factor $\mathrm{e}^{\Lambda} = r/\bar{r}$. The latter can be expanded on the left hand side using Eq. (1.7). This results in a new differential equation that needs to be solved:

$$\frac{\mathrm{d}\log\left(\bar{r}/r\right)}{\mathrm{d}r} = \frac{r^{1/2} - (r - 2m_{\mathrm{tot}})^{1/2}}{r(r - 2m_{\mathrm{tot}})^{1/2}} \tag{1.15}$$

In the exterior of the outermost fluid, where m_{tot} is constant, Eq. (1.15) has an analytic solution

$$r = \bar{r}\left(1 + \frac{2m_{\mathrm{tot}}}{\bar{r}}\right)^2. \tag{1.16}$$

Inside the star, we instead rewrite Eq. (1.15) as

$$\frac{\mathrm{d}r}{\mathrm{d}\bar{r}} = \frac{r}{\bar{r}}\sqrt{1 - \frac{2m_{\mathrm{tot}}}{r}} \tag{1.17}$$

and write Eqs. (1.7) and (1.11) as

$$\begin{aligned} \frac{\mathrm{d}m_i}{\mathrm{d}\bar{r}} &= 4\pi r^2 \varepsilon_i \frac{\mathrm{d}r}{\mathrm{d}\bar{r}} \\ \frac{\mathrm{d}P_i}{\mathrm{d}\bar{r}} &= -\frac{\left[P_i + \varepsilon_i\right]\left[m_{\mathrm{tot}} + 4\pi r^3 P_{\mathrm{tot}}\right]}{r\left[r - 2m_{\mathrm{tot}}(r)\right]}\frac{\mathrm{d}r}{\mathrm{d}\bar{r}} \end{aligned} \tag{1.18}$$

Equations (1.17) and (1.18) together form the system of equations that we solve numerically in the RNS code to obtain the initial conditions for rotating neutron star configurations.

Equilibrium sequences In the study of compact objects, the construction of equilibrium sequences represents one of the central tools to connect the microphysical properties of matter to macroscopic, observable quantities. An equilibrium sequence is defined as a continuous family of stationary solutions of the TOV equations cou-

pled to a given equation of state, obtained by varying a control parameter (e.g., the central density) while holding other physical quantities fixed in accordance with the astrophysical scenario under consideration. For instance, sequences at constant baryon mass describe the secular evolution of an isolated neutron star as it cools and spins down, whereas sequences at constant angular momentum are better suited to study stability in the context of binary mergers and remnants. Along these sequences, global quantities such as the gravitational mass, radius, moment of inertia, or quadrupole deformation can be traced as functions of the control parameter. These quantities are the macroscopic signature of the equation of state and mark the critical points beyond which systems at hydrostatic equilibrium are no longer possible.

The analysis of equilibrium sequences provides powerful stability diagnostics. A central tool is the *turning-point criterion* for secular stability, formulated by Friedman, Ipser, and Sorkin [20]. Along a one-parameter equilibrium sequence, stability against axisymmetric perturbations changes when an extremum is reached in the sequence of a conserved quantity. For example, in a sequence of nonrotating stars with increasing central density, the maximum of the gravitational mass marks the onset of instability to radial collapse: configurations on the ascending branch are stable, whereas those beyond the maximum are unstable. In rotating sequences, the same principle applies but with angular momentum held fixed. This criterion provides a computationally inexpensive method to determine stability boundaries without evolving the full dynamical system.

From the observational side, equilibrium sequences and the corresponding Mass-Radius (MR) curves provide the bridge between microscopic theory and experimental or astrophysical constraints. Precision radio-timing of pulsars in binary systems has led to measurements of neutron star masses above $2\,\mathrm{M}_\odot$ [21–23], setting stringent lower limits on the stiffness of the equation of state at supranuclear densities. Conversely, measurements of radii, though more difficult, are now increasingly accessible through X-ray pulse profile modelling with NICER [18, 19, 24–26] and from thermal emission of quiescent low-mass X-ray binaries. These observations restrict the allowed region in the MR space, ruling out models that predict stars too small or too large for the measured masses.

In addition, gravitational-wave observations from binary neutron star mergers, have introduced *tidal deformabilities* as new observational constraints, which can also be mapped consistently onto equilibrium sequences. The dimensionless tidal deformability Λ [27, 28] of a star quantifies how much it deforms under an external tidal field and is defined as

$$\Lambda = \frac{2}{3} k_2 \mathcal{C}^5, \tag{1.19}$$

where k_2 is the second Love number and $\mathcal{C} = M/R$ is the compactness parameter. Both R and M are extracted from equilibrium configurations, while k_2 is determined by solving linear perturbation equations on top of the equilibrium solution [29]. Since Λ depends very sensitively on the compactness $\mathcal{C}$, even small differences in the equilibrium sequences produced by different equations of state lead to significant variations in tidal deformability. The detection of GW170817 [2] and GW190425 [30], which constrained the combined tidal deformability of the binary system, has therefore ruled out extremely stiff or extremely soft equations of state that would predict stars with too large or too small Λ. Future gravitational-wave detections will sharpen these constraints further, effectively mapping allowed regions of the MR diagram and, through the turning-point criterion, narrowing down the range of possible maximum masses and stability limits for compact stars.

Laboratory experiments complement these astrophysical probes: heavy-ion collision experiments provide information about the symmetry energy and its density dependence, which directly feeds into the equation of state and alters the equilibrium sequences.

Equilibrium sequences form the essential framework by which microphysical models of dense matter are confronted with astrophysical observations and terrestrial experiments. By systematically constructing and analysing such sequences, it is possible to identify features of compact stars and discriminate among competing equations of state, opening a window on otherwise unreachable state of matter.

1.2 Microphysics and the equation of state

To obtain an expression for the equation of state as in Eq. (1.2) is not trivial. First approximations are often obtained using polytropic equations of state of the form

$$P = K\varepsilon^{\Gamma}, \tag{1.20}$$

where Γ is a polytropic index; values of Γ between 2 and 3 produce mass-radius relations consistent with observations [31] but don't include any physics and are commonly employed in testing numerical codes.

A practical improvement is to build a *piecewise polytropic* equation of state by joining several polytropes across density intervals:

$$P = K_i\,\varepsilon^{\Gamma_i}, \qquad \varepsilon \in [\bar{\varepsilon}_i,\, \bar{\varepsilon}_{i+1}), \tag{1.21}$$

each interval having its own Γ_i. The constants K_i are fixed to guarantee continuity of P across joining densities, while the sets $(\Gamma_i,\, \bar{\varepsilon}_i)$ are fitted to reproduce a tabulated microphysical equation of state. Both can also be supplied with an appropriate description of the thermal component based on the first principle of thermodynamics, in which we can write the pressure as

$$P_{th}(\varepsilon) = P(\varepsilon) + (\Gamma_{th} - 1)\varepsilon_{th} \tag{1.22}$$

where Γ_{th} is another constant and ε_{th} is an arbitrary function of the thermodynamical state that has the property of being zero at $T = 0$. While this procedure yields a compact parametrisation that is straightforward to implement numerically, one must keep in mind that the macroscopic predictions are extremely sensitive to the choices of break densities and polytropic indices. Piecewise polytropes are therefore regarded as controlled approximations rather than fundamental equation of state models.

We therefore need to resort to more physically sound, albeit approximate, methods to describe matter properties. For neutron stars, the assumptions of charge neutrality, zero temperature, and beta-equilibrium are fundamental in simplifying

the complex many-body problem.

Stars older than a few minutes typically cool to temperatures well below $\sim 1\,\mathrm{MeV}$ via neutrino emission [31, 32]. This is negligible compared with nuclear energy scales, allowing thermal effects to be ignored. Beta-equilibrium ensures that all chemical potentials of constituent particles are fixed through relations such as $\mu_n = \mu_p + \mu_e$. This leads to very low proton fractions in the core (typically $< 10\%$ [3]), producing highly neutron-rich matter, a defining characteristic of neutron star interiors. Charge neutrality, applied either locally or globally, requires the sum of all charges vanish, ensuring stability against strong electric fields.

In the neutron star crust, local charge imbalance can exist, leading to structured phases such as the lattice of nuclei in the outer crust or the complex "pasta phases" [16] in the inner crust, where free neutrons form a superfluid and entrainment effects influence transport properties. As density increases toward the core, nuclei dissolve into homogeneous nuclear matter. The outer core consists of a degenerate Fermi liquid of neutrons, protons, and electrons, with muons appearing at higher densities, while the inner core at supranuclear densities may host exotic particles and phases, including hyperons, meson condensates, nuclear resonances and deconfined quark matter, each of which can significantly soften the equation of state and alter mass-radius relations.

We will now proceed to explore two specific equations of state, namely the DD2, and IST, which will be employed in Chapters 3 to 5 to describe the baryonic matter component.

DD2 Within the relativistic mean field framework, the DD2 parametrization [33] is a widely used density-dependent effective model for describing dense baryonic matter under astrophysical conditions. In this model, nucleons (neutrons and protons) interact via the exchange of minimally coupled mesons (σ, ω_μ, and $\vec{\rho}_\mu$). Meson self-interactions are not included; instead, the couplings are assumed to be functions of the nucleon currents, simulating the medium dependence of the interaction. Light clusters corresponding to the ground states of the deuteron (d = ^{2}H), triton (t = ^{3}H), helion (h = ^{3}He), and alpha particles (α = ^{4}He) are introduced as spin 1 (d), spin

1/2 (t, h), and spin 0 (α) fields. The influence of the medium on cluster properties is described by density- and temperature-dependent shifts of their binding energies.

The starting point is a Lorentz-invariant Lagrangian density:

$$\mathcal{L} = \mathcal{L}_{\text{fermion}} + \mathcal{L}_{\text{boson}} + \mathcal{L}_{\text{meson}} + \mathcal{L}_{\text{lepton}} , \tag{1.23}$$

where each term describes a different component of the system. Defining a covariant derivative

$$iD_i^\mu = i\partial^\mu - g_\omega A_i \omega^\mu - g_\rho |N_i - Z_i| \vec{\tau} \cdot \vec{\rho}^\mu, \tag{1.24}$$

with g_i the density-dependent coupling and (A_i, Z_i, N_i) the mass, proton, and neutron numbers of the particle, we can write

$$\mathcal{L}_{\text{fermion}} = \sum_{i=n,p,t,h} \bar{\psi}_i \left(\gamma_\mu i D_i^\mu - m_i^*\right) \psi_i. \tag{1.25}$$

Here, ψ_i denotes a Dirac field and m_i^* the associated effective mass. The boson term $\mathcal{L}_{\text{boson}}$ contains the α and d particles, described by Klein-Gordon and Proca fields:

$$\begin{aligned} \mathcal{L}_{\text{boson}} =& \frac{1}{2} \left(iD_\alpha^\mu \phi_\alpha\right)^* \left(iD_{\alpha\mu} \phi_\alpha\right) - \frac{1}{2} m_\alpha^{*2} \phi_\alpha^2 + \\ & \frac{1}{4} \left(iD_d^\mu \phi_\alpha^\nu - iD_d^\nu \phi_\alpha^\mu\right)^* \left(iD_{d\mu} \phi_{\alpha\nu} - iD_{d\nu} \phi_{\alpha\mu}\right) - \frac{1}{2} m_d^{*2} \phi_d^{\mu *} \phi_{d\mu}. \end{aligned} \tag{1.26}$$

The meson term $\mathcal{L}_{\text{meson}}$ contains the free mesonic contributions:

$$\mathcal{L}_{\text{meson}} = \frac{1}{2} \left(\partial^\mu \sigma \partial_\mu \sigma - m_\sigma^2 \sigma^2 - G^{\mu\nu} G_{\mu\nu} + m_\omega^2 \omega^\mu \omega_\mu - \frac{1}{2} \vec{H}^{\mu\nu} \vec{H}_{\mu\nu} + m_\rho^2 \vec{\rho}^\mu \cdot \vec{\rho}_\mu \right), \tag{1.27}$$

where the field strength tensors are $G_{\mu\nu} = \partial_\mu \omega_\nu - \partial_\nu \omega_\mu$ and $\vec{H}_{\mu\nu} = \partial_\mu \vec{\rho}_\nu - \partial_\nu \vec{\rho}_\mu$. Finally, $\mathcal{L}_{\text{lepton}}$ accounts for electrons and muons, which are described as free relativistic gases ensuring charge neutrality.

The novelty of density-dependent models lies in the meson-nucleon couplings, which are explicit functions of the baryon number density n_B. In DD2, they take rational forms for the isoscalar mesons and exponential forms for the isovector meson,

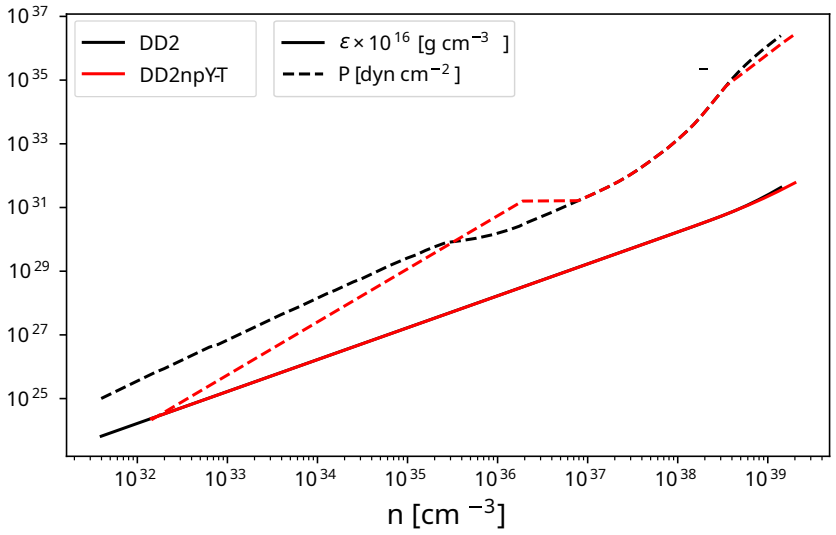

Figure 1.1: Comparison of DD2 and DD2npY-T equations of state. To facilitate a direct visual comparison between the two quantities, the energy density has been rescaled by a factor of 10^{16}.

e.g.,

$$g_i(n_B) = g_i(n_{\rm sat})\, f_i(x), \qquad x = \frac{n_B}{n_{\rm sat}}, \tag{1.28}$$

where $n_{\rm sat}$ is the saturation number density and $f_i(x)$ are fitted functions ensuring empirical consistency.

Applying the Euler-Lagrange equations and adopting the mean-field approximation, the meson fields are replaced by their classical expectation values, leading to a set of coupled algebraic equations:

$$m_\sigma^2\, \sigma = g_\sigma(n_B) n_\sigma, \tag{1.29}$$

$$m_\omega^2\, \omega^0 = g_\omega(n_B)\, n_\omega - h_\omega(B_i), \tag{1.30}$$

$$m_\rho^2\, \rho_3^0 = g_\rho(n_B)\, n_\rho - h_\rho(B_i), \tag{1.31}$$

where n_σ, n_ω, and n_ρ are computed from the scalar and vector densities of each particle in Eq. (1.23), and $h_\omega(B_i)$ and $h_\rho(B_i)$ are functions of the cluster binding energies (i.e., zero for protons and neutrons) and the scalar densities.

The total energy density and pressure follow from the energy-momentum tensor, completely defining the equation of state.

The DD2 model is relatively stiff at supra-nuclear densities and has a symmetry energy slope within the accepted phenomenological range. It forbids the nucleonic direct Urca process for typical neutron star compositions [34], provides a unified equation of state (covering both crust and core), and predicts a maximum neutron star mass of $\sim 2.4\,\mathrm{M}_\odot$. For a canonical $1.4\,\mathrm{M}_\odot$ star, the DD2 equation of state yields a radius of $R \simeq 13.3\,\mathrm{km}$. It is consistent with the maximum mass requirement for neutron stars [21–23], the tidal deformability constraints inferred from the LIGO/Virgo observations of the GW170817 and GW190425 binary NS mergers [2, 30], and the NICER measurements of pulsars [18, 19, 24–26].

A major uncertainty in dense nuclear matter is the appearance of hyperons in the core of neutron star, known as the "hyperon problem": the additional degrees of freedom tend to soften the equation of state and reduce the maximum mass, often below the observed $2\,\mathrm{M}_\odot$ limit. One way to address this is by introducing density-dependent couplings for the hyperons. The DD2npY-T model [35] implements this approach, including the full baryon octet (Λ, Σ, Ξ) with couplings constrained by SU(6) symmetry relations and hypernuclear data. Despite the presence of hyperons, this parametrization remains consistent with the $2\,\mathrm{M}_\odot$ constraint and provides a realistic extension of DD2 suitable for neutron star calculations. Figure 1.1 shows the pressure and energy density of the DD2npY-T equation of state used in the following chapters, comparing it with the original DD2 equation of state presented above.

IST The Induced Surface Tension (IST) equation of state [36, 37] provides an alternative approach to obtain a microphysically motivated description of dense baryonic matter, improving upon conventional excluded-volume and mean-field models by treating repulsive interactions in a thermodynamically consistent way. It is based on the statistical multifragmentation model, where the virial expansion of nucleons and clusters with finite hard-core radii generates contributions to the free energy proportional both to their volume and to their surface area. The latter naturally gives rise

to an *induced surface tension* term, which encodes higher-order correlations between constituents. The IST framework introduces the surface tension coefficient σ as an additional thermodynamic variable and couples it to the pressure through a closed set of equations. This extension allows the model to describe compressible nuclear matter at both sub-saturation and supranuclear densities, while simultaneously avoiding the pathological extrapolations inherent in conventional mean-field schemes.

At zero temperature, in the grand canonical ensemble, the IST equation of state for a β-equilibrated, charge-neutral mixture of neutrons, protons, and electrons reads

$$p = \sum_{A=n,p,e} p^{\mathrm{id}}\Big(m_A, \nu_A^{(1)}\Big) - p_{\mathrm{int}}\big(n_B^{\mathrm{id}}\big) + p_{\mathrm{sym}}\big(n_B^{\mathrm{id}}, I^{\mathrm{id}}\big)\,, \tag{1.32}$$

$$\sigma = \sum_{A=n,p} p^{\mathrm{id}}\Big(m_A, \nu_A^{(2)}\Big)\, R_{\mathrm{nucl}}, \tag{1.33}$$

where $p^{\mathrm{id}}(m,\mu)$ denotes the pressure of a free degenerate Fermi gas of mass m and chemical potential μ. Neutrons and protons are treated as hard spheres with a common radius $R_{\mathrm{nucl}} \simeq 0.3{-}0.5$ fm, while electrons are included as pointlike fermions with $R_e = 0$.

The effective chemical potentials $\nu_A^{(1,2)}$ include the contributions of excluded-volume repulsion, mean-field attraction, and nuclear symmetry energy,

$$\nu_A^{(1)} = \mu_A - pV - \sigma S + U\big(n_B^{\mathrm{id}}\big) \mp U_{\mathrm{sym}}\big(n_B^{\mathrm{id}}, I^{\mathrm{id}}\big)\,, \tag{1.34}$$

$$\nu_A^{(2)} = \mu_A - pV - \alpha\sigma S + U_0, \tag{1.35}$$

with eigenvolume $V = \frac{4}{3}\pi R_{\mathrm{nucl}}^3$ and surface $S = 4\pi R_{\mathrm{nucl}}^2$. The parameter α is calibrated to reproduce the virial expansion of hard spheres up to the fourth virial coefficient, with $\alpha \simeq 1.245$, thus ensuring a faithful description of repulsive correlations. The mean-field attraction is parametrised as

$$U\big(n_B^{\mathrm{id}}\big) = C_d^2\,\big(n_B^{\mathrm{id}}\big)^{\kappa}, \qquad p_{\mathrm{int}}\big(n_B^{\mathrm{id}}\big) = \int_0^{n_B^{\mathrm{id}}} \ell\,\frac{\partial U(\ell)}{\partial \ell}\,d\ell, \tag{1.36}$$

where n_B^{id} is the baryon density of the corresponding free gas. An additional constant

shift U_0 contributes to $\nu_A^{(2)}$ but cancels from the pressure.

The isospin-asymmetric sector is described via the symmetry-energy pressure term $p_{\rm sym}$, for which a convenient parametrisation is

$$p_{\rm sym}(n_B^{\rm id}, I^{\rm id}) = \frac{A_{\rm sym}\,(n_B^{\rm id} I^{\rm id})^2}{\left[1 + (B_{\rm sym} n_B^{\rm id} I^{\rm id})^2\right]^2}, \tag{1.37}$$

with the asymmetry parameter $I^{\rm id} = (n_n^{\rm id} - n_p^{\rm id})/n_B^{\rm id}$. The corresponding mean-field potential $U_{\rm sym}$ is obtained from thermodynamic consistency.

All model parameters are constrained by empirical information: the saturation density $n_0 \simeq 0.16$ fm^{-3}, binding energy per nucleon $E/A \simeq -16$ MeV, incompressibility K_0, and symmetry energy J and slope L, as well as heavy-ion collision data on proton flow and hadron multiplicities. Two representative parameter sets, A and B, reproduce these constraints while differing in stiffness: the stiffer set A yields larger neutron star radii, whereas the softer set B, that will be used in Chapter 4, results in more compact configurations, both remaining consistent with the astrophysical constraints from GW170817 [2]. Importantly, the IST equation of state also provides a physically consistent description of the nuclear liquid-gas phase transition and its critical endpoint. In this way, it offers a unified framework connecting nuclear physics, heavy-ion collisions, and neutron star astrophysics within a single thermodynamically consistent model.

1.3 Axisymmetric equilibria

In many relevant astrophysical scenarios, such as immediately after the birth of a proto-neutron star or following the merger of two neutron stars into an hypermassive neutron star remnant, the approximation of spherical symmetry is no longer valid, and Eqs. (1.17) and (1.18) must be generalised to include rotation.

One possible approach is the Hartle–Thorne approximation for slowly rotating stars [38, 39]. In this framework, the configuration is characterised by a uniform angular velocity that is sufficiently small so that the rotational corrections to pressure,

energy density, and the gravitational field remain perturbative. The field equations are then expanded in powers of the angular velocity, with first- and second-order terms retained to capture the leading effects of rotation.

While highly useful, this approximation is limiting. This regime is indeed valid for many systems, where an isolated neutron star is old and nearly spherical. However, for more energetic configurations, such as millisecond pulsars or merger remnants, the assumption

$$R\Omega \ll c, \tag{1.38}$$

where R is the radius of the unperturbed configuration, Ω an the typical angular velocity and c the speed of light, no longer holds. In these cases, a fully relativistic description of rotation becomes unavoidable. At present, however, no closed-form analytic solution exists for a rotating neutron star with a realistic equation of state, and one must resort to numerical methods.

Following [31], we begin by describing the general equations governing axisymmetric spacetimes and the relativistic hydrostatic equilibrium equation. In Appendix A we will turn to the specific Komatsu–Eriguchi–Hachisu (KEH) scheme [40] and the RNS code[1] [41, 42], which implements it with the modifications of [43–45].

The spacetime To describe the spacetime of an axisymmetric star, we impose three conditions on the metric:

(i) the spacetime is asymptotically flat;

(ii) it is stationary and axisymmetric, admitting a timelike Killing vector t^α and a spacelike rotational Killing vector ϕ^α;

(iii) there exists a discrete isometry that simultaneously reverses the directions of time and rotation.

Conditions (ii) and (iii) imply that t^α and ϕ^α commute, i.e. $[t, \phi] = 0$. This guarantees the existence of coordinates $x^0 = t$ and $x^3 = \phi$ adapted to the symmetries, such

[1] github.com/cgca/rns

that

$$t^\alpha = \boldsymbol{\partial}_t, \qquad \phi^\alpha = \boldsymbol{\partial}_\phi, \tag{1.39}$$

and the metric components are independent of t and ϕ themselves. Unlike in the spherically symmetric case, where time-reversal symmetry enforces $g_{t\phi} = 0$, a rotating star admits a non-vanishing $g_{t\phi}$ component: there is no family of hypersurfaces orthogonal to the timelike Killing vector t^α. This lack of orthogonality is quantified by the potential ω, which encodes the dragging of inertial frames.

A convenient choice for the remaining two coordinates is given by quasi-isotropic coordinates $x^1 = r$, $x^2 = \theta$, defined such that $g_{r\theta} = 0$ and $g_{\theta\theta} = r^2 g_{rr}$. In this gauge, the most general stationary, axisymmetric metric can be written as

$$\mathrm{d}s^2 = -\,\mathrm{e}^{\nu}\mathrm{d}t^2 + \mathrm{e}^{2\alpha}\big(\mathrm{d}r^2 + r^2\mathrm{d}\theta^2\big) + \mathrm{e}^{2\psi}\big(\mathrm{d}\phi - \omega\,\mathrm{d}t\big)^2, \tag{1.40}$$

where $\nu(r,\theta)$, $\alpha(r,\theta)$, $\psi(r,\theta)$, and $\omega(r,\theta)$ are metric functions depending only on r and θ. The function e^{ψ} corresponds to the proper circumferential radius; in the nonrotating limit it reduces to $R\sin\theta$, where R is the Schwarzschild radial coordinate.

The 4-velocity of a fluid element can be expressed as a linear combination of the two Killing vectors,

$$u^\alpha = u^t\big(t^\alpha + \Omega\,\phi^\alpha\big), \tag{1.41}$$

with $\Omega = \mathrm{d}\phi/\mathrm{d}t$ the angular velocity of the fluid as measured by an observer at rest at infinity.

To obtain a tractable form of the Einstein field equations for axisymmetric, rotating stars, we introduce a family of *zero angular momentum observers* (ZAMOs), whose 4-velocity at each point reads

$$u^\alpha_{\mathrm{ZAMO}} = \mathrm{e}^{-\nu}\,(t^\alpha + \omega\,\phi^\alpha)\,. \tag{1.42}$$

In this reference frame, the physical 3-velocity of the fluid relative to the ZAMOs is $v = (\Omega - \omega)\,\mathrm{e}^{\psi-\nu}$. Consider now, as in Section 1.1, a collection of N fluids that interact only gravitationally with $T^{\alpha\beta} = \sum_i T^{\alpha\beta}_{(i)}$. For the i-th perfect fluid, the

stress-energy tensor in this frame takes the form

$$T^{\alpha\beta}_{(i)} = \begin{pmatrix} \frac{\varepsilon_i + P_i v_i^2}{1-v_i^2} & \frac{(\varepsilon_i + P_i) v_i}{1-v_i^2} & 0 & 0 \\ \frac{(\varepsilon_i + P_i) v_i}{1-v_i^2} & \frac{\varepsilon_i v_i^2 + P_i}{1-v_i^2} & 0 & 0 \\ 0 & 0 & P_i & 0 \\ 0 & 0 & 0 & P_i \end{pmatrix}. \tag{1.43}$$

Following [46], we define a new metric function $\zeta = \alpha + \nu$, and introduce $\mathrm{e}^{\psi+\nu} = r \sin\theta \, B(r,\theta)$, as in [47]. In terms of these variables, the Einstein field equations reduce to a set of coupled elliptic equations for the metric potentials. The (t,t) and (r,t) equations are respectively:

$$\begin{aligned} \boldsymbol{\nabla} \cdot (B \, \boldsymbol{\nabla} \nu) = & \frac{1}{2} r^2 \sin^2\theta \, B^3 \, \mathrm{e}^{-4\nu} \, \boldsymbol{\nabla}\omega \cdot \boldsymbol{\nabla}\omega \\ & + 4\pi B \, \mathrm{e}^{2\zeta - 2\nu} \sum_i \left[(\varepsilon_i + P_i) \frac{1+v_i^2}{1-v_i^2} + 2P_i \right], \end{aligned} \tag{1.44}$$

$$\boldsymbol{\nabla} \cdot \left(r^2 \sin^2\theta \, B^3 \, \mathrm{e}^{-4\nu} \, \boldsymbol{\nabla}\omega \right) = -16\pi r \sin\theta \, B^2 \, \mathrm{e}^{2\zeta - 4\nu} \sum_i \frac{(\varepsilon_i + P_i) v_i}{1-v_i^2}. \tag{1.45}$$

The third equation is instead given as a combination (t,t) - (r,r):

$$\boldsymbol{\nabla} \cdot (r \sin\theta \, \boldsymbol{\nabla} B) = 16\pi r \sin\theta \, B \, \mathrm{e}^{2\zeta - 2\nu} \sum_i P_i. \tag{1.46}$$

The system is supplemented by a first-order differential equation for ζ,

$$\begin{aligned}
\partial_\mu \zeta = &- \left\{ \left(1-\mu^2\right) \left(1 + rB^{-1}\partial_r B\right)^2 + \left[\mu - \left(1-\mu^2\right) B^{-1}\partial_\mu B\right]^2 \right\}^{-1} \\
&\times \Bigg[\!\!\Bigg[\frac{1}{2} B^{-1} \left\{ r^2 \partial_r^2 B - \partial_\mu \left[\left(1-\mu^2\right) \partial_\mu B \right] - 2\mu \partial_\mu B \right\} \left\{ -\mu + \left(1-\mu^2\right) B^{-1} \partial_\mu B \right\} \\
&+ rB^{-1}\partial_r B \left[\frac{1}{2}\mu + \mu r B^{-1}\partial_r B + \frac{1}{2}\left(1-\mu^2\right) B^{-1}\partial_\mu B \right] \\
&+ \frac{3}{2} B^{-1}\partial_\mu B \left[-\mu^2 + \mu \left(1-\mu^2\right) B^{-1}\partial_\mu B \right] - \left(1-\mu^2\right) r B^{-1} \partial^2_{r\mu} B \left(1 + rB^{-1}\partial_r B\right) \\
&- r^2 \mu \left(\partial_r \nu\right)^2 - 2\left(1-\mu^2\right) r \partial_\mu \nu \partial_r \nu + \mu \left(1-\mu^2\right) \left(\partial_\mu \nu\right)^2 \\
&- 2\left(1-\mu^2\right) r^2 B^{-1} \partial_r B \partial_\mu \nu \partial_r \nu + \left(1-\mu^2\right) B^{-1} \partial_\mu B \left[r^2 \left(\partial_r \nu\right)^2 - \left(1-\mu^2\right) \left(\partial_\mu \nu\right)^2 \right] \\
&+ \left(1-\mu^2\right) B^2 \, \mathrm{e}^{-4\nu} \left\{ \frac{1}{4} \mu r^4 \left(\partial_r \omega\right)^2 + \frac{1}{2} \left(1-\mu^2\right) r^3 \partial_\mu \omega \partial_r \omega \right. \\
&- \frac{1}{4} \mu \left(1-\mu^2\right) r^2 \left(\partial_\mu \omega\right)^2 + \frac{1}{2} \left(1-\mu^2\right) r^4 B^{-1} \partial_r B \partial_\mu \omega \partial_r \omega \\
&\left. - \frac{1}{4} \left(1-\mu^2\right) r^2 B^{-1} \partial_\mu B \left[r^2 \left(\partial_r \omega\right)^2 - \left(1-\mu^2\right) \left(\partial_\mu \omega\right)^2 \right] \right\} \Bigg]\!\!\Bigg]
\end{aligned} \tag{1.47}$$

In Eqs. (1.44) to (1.46), the operator $\boldsymbol{\nabla}$ represents the flat 3-dimensional derivative in (r, θ, ϕ) coordinates and in Eq. (1.47) we defined, for computational convenience, $\mu = \cos\theta$ (see Appendix A).

The fluid These equations for the metric field need to be supplemented with a hydrostatic equilibrium equation that determines the profile of the ε and P fields.

The dynamical evolution of the fluid is governed by the vanishing of the divergence of the stress-energy tensor

$$\nabla_\beta T^{\alpha\beta} = 0\,. \tag{1.48}$$

Projecting this equation orthogonally to the 4-velocity u^α, we obtain

$$0 = p^\alpha{}_\gamma \nabla_\beta T^{\beta\gamma} = p^\alpha{}_\gamma \nabla_\beta \left[P p^{\beta\gamma} + \varepsilon u^\beta u^\gamma \right]\,, \tag{1.49}$$

where $p^{\alpha\beta} = g^{\alpha\beta} + u^\alpha u^\beta$ is the projector operator. Expanding this expression, we obtain the relativistic Euler equation

$$u^\beta \nabla_\beta u^\alpha = -p^{\alpha\beta} \frac{\nabla_\beta P}{\varepsilon + P} \,. \tag{1.50}$$

Since all quantities depend only on the variables r and θ, we get that $p_\alpha{}^\beta \nabla_\beta P = \nabla_\alpha P$. Moreover, the directional derivative on the left hand side can be expressed in terms of the scalar quantities $u^t = u^\alpha \nabla_\alpha t$ and $u_\phi = u_\alpha \phi^\alpha$. The Euler equation for a stationary, axisymmetric star then becomes

$$\frac{\nabla_\alpha P}{\varepsilon + P} = \nabla_\alpha \ln u^t - u^t u_\phi \nabla_\alpha \Omega \,. \tag{1.51}$$

We now reformulate this equation in a way that is convenient for numerical treatment. We start by defining the specific enthalpy as

$$h = \frac{\varepsilon + P}{\rho} \,, \tag{1.52}$$

where ε and P are functions of the rest-mass density ρ and the specific entropy s. For barotropic equations of state, we introduce

$$H(P) = \int_0^P \frac{\mathrm{d}\tilde{P}}{\varepsilon(\tilde{P}) + \tilde{P}} \,, \tag{1.53}$$

such that

$$\nabla H = \frac{\nabla P}{\varepsilon + P} \,. \tag{1.54}$$

In the more general non-barotropic case, one has instead $\nabla H = \nabla \ln h - \frac{T}{h} \nabla s$. The operator ∇ here denotes the 2-dimensional gradient in the (r, θ) subspace. Using this definition, Eq. (1.51) can be written as

$$\nabla \left(H - \ln u^t \right) = -j(\Omega) \, \nabla \Omega, \qquad j(\Omega) = u^t u_\phi \,. \tag{1.55}$$

For homoentropic stars ($s = \text{const.}$), one has $H = \ln h$, and the Euler equation takes

the form

$$\nabla\left(\ln\frac{h}{u^t}\right) = -j(\Omega)\,\nabla\Omega\,, \tag{1.56}$$

which admits the global first integral

$$H - \ln u^t + \int_{\Omega_{\rm pole}}^{\Omega} j(\Omega')\,\mathrm{d}\Omega' = \text{const}\,. \tag{1.57}$$

The lower bound of the integral is chosen at the point where both H and the 3-velocity v vanish. Equation (1.57) is the formulation that is implemented in the RNS code to compute the specific enthalpy h, which is related through the equation of state to both the energy density and the pressure fields.

The rotation law The last ingredient needed to close the system of Eqs. (1.44) to (1.46) and (1.57) is an explicit form of the rotation law $j(\Omega) := u^t u_\phi$. This quantity encodes the angular velocity distribution inside the star, and thus defines the class of rotating equilibria being modelled.

Uniform angular velocity minimizes the total mass-energy of a configuration [48, 49], so for most of their lifetimes neutron stars are expected to rotate uniformly. On the other hand, immediately after birth, neutron stars are expected to be differentially rotating. Comparisons with numerical relativity simulations [50] show that the angular profile is well approximated in this scenario by the law

$$j(\Omega) = A^2(\Omega_c - \Omega) \tag{1.58}$$

introduced by [40] and called *j-constant* law. Here A is a positive constant that sets the length scale over which the angular velocity varies within the star, and Ω_c is the angular velocity on the rotation axis. In particular, $A \to \infty$ recovers uniform rotation, while decreasing A enhances the degree of differential rotation.

Another interesting scenario in which the neutron star is expected to be differentially rotating is the remnant formed after a binary neutron star merger. However, Eq. (1.58) does not adequately capture the resulting rotation profile [51, 52], and

a more complex form of $j(\Omega)$ is required. A particularly rich family was proposed in [53], characterized by an almost uniformly rotating inner core, a sharp peak, and a Keplerian fall-off $\left(\Omega \sim r^{-3/2}\right)$. Two members of this family are of particular interest and have been extensively used:

$$\Omega(j) = \Omega_c \frac{1 + \left(\frac{j}{B^2\Omega_c}\right)^p}{1 + \left(\frac{j}{A^2\Omega_c}\right)^{p+q}} \tag{1.59}$$

and

$$\Omega(j) = \Omega_c \left[1 + \left(\frac{j}{B^2\Omega_c}\right)^p\right] \left(1 + \frac{j}{A^2\Omega_c}\right) . \tag{1.60}$$

For computational convenience (see Appendix A), these relations have been formulated in the inverse form $\Omega = \Omega(j)$; accordingly, the integral in Eq. (1.57) must be rewritten as

$$\int_{\Omega_{\rm pole}}^{\Omega} j(\Omega')\mathrm{d}\Omega' = \int_0^j j' \frac{\mathrm{d}\Omega}{\mathrm{d}j'} \mathrm{d}j' . \tag{1.61}$$

Equation (1.59) depends on four parameters (A, B, p, q), while the second, Eq. (1.60), involves only three (A, B, p). Different choices of these parameters correspond to distinct physical scenarios [54]; in particular, the maximum of the energy density can shift away from the stellar centre, leading to either spheroidal or toroidal configurations, depending on the degree and nature of differential rotation.

Throughout Chapters 4 and 5, we will restrict our analysis to two cases: uniform rotation, for which the integral in Eq. (1.61) vanishes, and the differential law of Eq. (1.59) with the specific choice $p = 1$ and $q = 3$, the only combination that admits an analytical solution of the integral and ensures a Keplerian fall-off of the angular velocity profile.

Chapter 2

Dark matter and its role in compact objects

Dark matter is a generic term encompassing a wide range of standard and new physics aimed at resolving some of the major discrepancies found in astrophysical observations. Its story begins with the observations of Kelvin, Poincaré, Öpik, Kapteyn and Oort (see [55] for a historical introduction), who used the dynamics of stars in the Milky Way to estimate the total mass of matter in the Galaxy: they found that in the local vicinity of the Solar System stars dominate the matter content [56, 57]. Meanwhile, Zwicky estimated that within the Abell 1656 galaxy cluster (commonly known as the Coma Cluster), the velocity dispersion of galaxies, computed using the virial theorem, differs by an order of magnitude from the experimentally measured value [58, 59].

A significant clue about the presence of dark matter came from the observations of Vera Rubin and others [60–64]. They showed that beyond the radius in which baryonic matter is concentrated, the velocity of stars remains largely independent of the radial position, in contrast with the expected Newtonian profile $v \sim r^{-1/2}$. To explain this behaviour, they proposed that the galactic mass is dominated by a spherical halo of matter, not detectable with electromagnetic observations, which extends far beyond the visible bounds of the galaxy. This behaviour is visible, for example, in Fig. 2.1.

Another evidence of the existence of dark matter comes from gravitational lensing. Since gravity can distort the trajectory of light, a distant luminous object might be observed from Earth as distorted in ways predicted by general relativity.

Clowe [65] used this effect to study the mass distribution of the 1E 0657-56 cluster (commonly known as the Bullet Cluster). Gravitational lensing observations reveal that the total mass distribution does not coincide with the distribution of baryonic

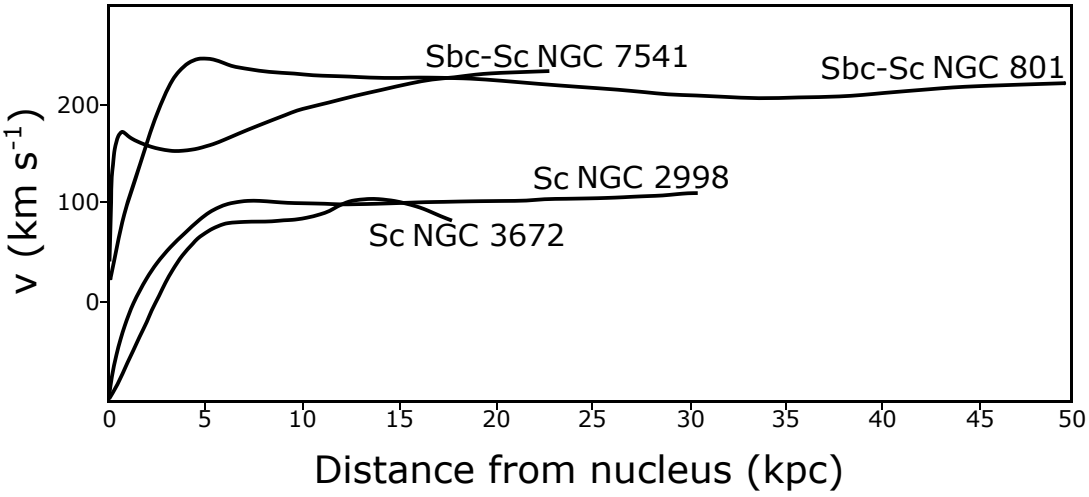

Figure 2.1: Galactic rotation curves as function of the radial distance from the nucleus for four different galaxies. Figure adapted from [64].

matter. In particular, the baryonic matter is concentrated closer to the centre of the system, while the dominant mass component, attributed to dark matter, remains more spread out. This is consistent with the fact that baryonic matter interacts during the merger, whereas dark matter, being collisionless or very weakly interacting, passes through. The predicted distribution is shown in Fig. 2.2. This is a strong evidence of the non-baryonic nature of dark matter and it has been confirmed by observations of other galaxy cluster mergers [66].

Lastly, evidence for the existence of dark matter also comes from cosmology, in particular from the cosmic microwave background (CMB). The CMB is a relic photon gas permeating the universe, which decoupled from baryonic matter about 3.8×10^5 yr after the Big Bang. It provides a snapshot of the photon-baryon fluid at the time of recombination, when photons and baryons shared a common density pattern.

In the framework of general relativity, spatial fluctuations in the matter density are expected to grow linearly with the scale factor, or equivalently as $1/(1+z)$, where z is the redshift parameter. Since recombination occurred at $z \approx 1100$, one would

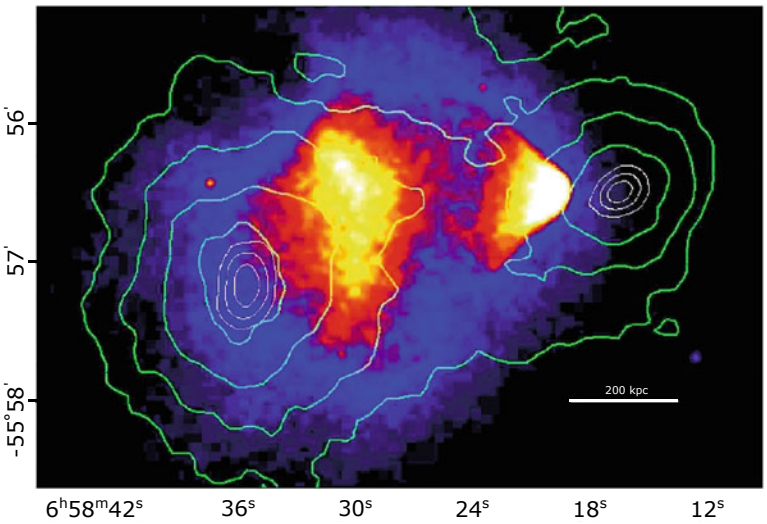

Figure 2.2: Image of the 1E 0657-56 cluster. The colorscale represent the measured X-ray emission by the hot gas. The green contours represent the estimated matter distribution from gravitational lensing. Image adapted from [65].

expect density fluctuations in the CMB of order 10^{-2} [67]. Observations, however, show much smaller fluctuations, of order 10^{-5}, which would be insufficient to allow the formation of the structures (galaxies and clusters) we observe today.

This discrepancy can be resolved by introducing a component of nonrelativistic cold dark matter (CDM), interacting only weakly with baryons. CDM would have begun to collapse gravitationally well before recombination, while baryons remained tightly coupled to radiation. After decoupling, baryons fell into the already-formed dark matter potential wells, allowing galaxy formation to proceed efficiently [68, 69].

All the evidence reported above (and more [70]) consistently points to the same conclusion: around 84% of the matter content of the Universe is composed of dark matter.

Dark matter candidates The identification of the nature of this component is another matter entirely. From very general considerations, it is possible to determine absolute bounds on the dark matter candidate mass, $M \in (10^{-49}, 10^{45})\ \mathrm{M_{Pl}}$, where $\mathrm{M_{Pl}} \approx 2 \times 10^{-8}\,\mathrm{kg}$ is the Planck mass, spanning 94 orders of magnitude.

The lower limit is set by quantum mechanics, which requires the particle's de Broglie wavelength to be smaller than the radius of dwarf galaxies [71], $R \sim 1\,\mathrm{kpc}$, assuming a virialized velocity of the dark matter particle $v_{\mathrm{DM}} \sim 300\,\mathrm{km\,s^{-1}}$ [72]. The upper bound, instead, exceeds the Planck mass limit, i.e. the maximum mass a fundamental particle can have before collapsing into a black hole, when considering compound objects. In particular, one must impose that the mass of such a compound object is smaller than that of a dwarf galaxy, while ensuring there are a sufficient number of them to approximate a smooth halo reproducing the observed galactic dynamics.

Among the plethora of dark matter models [70], some have emerged as more favourable candidates, although none perfectly addresses all the complexities associated with astrophysical measurements. Observational evidence suggests that dark matter particles should be electrically neutral, while their self-interactions must remain sufficiently weak to satisfy constraints from structure formation and from galaxy cluster observations, which currently impose limits of order $\sigma/m < 1\,\mathrm{cm^2/g}$. This upper limit is, however, large enough to encompass all interactions that are weaker than the baryonic strong force.

The first class of models worth exploring describes Weakly Interacting Massive Particles (WIMPs). Initially, the adjective *weakly* referred specifically to interactions mediated by the $SU(2)_L$ gauge group, but today it is understood in a broader sense, encompassing particles that interact with at most weak-scale strength. WIMPs are particularly attractive because of the so-called "WIMP miracle": particles with electroweak-scale masses and cross-sections naturally freeze out of thermal equilibrium in the early Universe with a relic abundance that is remarkably close to the observed dark matter density. Despite decades of dedicated searches in direct detection experiments, collider facilities, and indirect probes, no conclusive signal has been found, which has motivated the exploration of non-WIMP scenarios.

Non-WIMP candidates encompass a variety of possibilities with distinct production mechanisms and phenomenology. Axions and axion-like particles, originally introduced to solve the strong CP problem in quantum chromodynamics, are very light bosons produced non-thermally in the early Universe, behaving as cold dark

matter on cosmological scales. Sterile neutrinos, neutral fermions interacting only via mixing with active neutrinos, can be produced through oscillation mechanisms and typically constitute warm dark matter, with potential astrophysical signatures in galaxy formation and X-ray observations.

Other constructions invoke hidden or dark sectors with their own force carriers, such as dark photons, where dark matter particles are produced through very feeble interactions with the Standard Model, for instance via freeze-in processes.

Finally, distinct from these particle physics scenarios is the domain of macroscopic dark matter candidates. The most prominent hypothesis is that of Primordial Black Holes (PBHs) [73, 74], formed from the collapse of large density fluctuations in the early Universe. Other macroscopic possibilities include exotic solitonic states like Q-balls [75] or nuggets of strange quark matter (strangelets/nuclearites) [76, 77]. While this thesis focuses on fluid-like dark matter capable of forming stable admixtures with baryonic matter, these macroscopic candidates are nonetheless relevant in the context of compact objects. The capture of a PBH or a strangelet by a neutron star would typically lead to the rapid consumption or conversion of the host [78, 79], providing constraints on their abundance that are complementary to the accumulation scenarios studied in the following chapters.

2.1 Self interacting dark matter

Despite decades of extensive searches, all evidence for collisionless cold dark matter comes from its gravitational influence on cosmological and galactic scales. Since the 1990s, numerical simulations of a universe composed solely of dark matter have revealed four key discrepancies with observations.

The most famous is the core-cusp problem. Simulations predict that the dark matter density profile should rise steeply toward the centre, resulting in a cusp $\rho_{\rm DM} \propto r^{-1}$ [80, 81]. Observations, however, often favour constant-density cores, with $\rho_{\rm DM} \propto r^{0}$ [82, 83]. This tension is most evident in dwarf and low-surface-brightness galaxies [84–93], where the dark matter dominates the mass budget and thus provides a clean test of cold dark matter predictions.

Two related issues are the missing satellites and the too-big-to-fail problems. The missing satellites problem arises because galactic halos form hierarchically from smaller halos that should survive as substructure [94]. Simulations therefore predict hundreds to thousands of dwarf galaxies around Milky Way sized halos, whereas only about ten were known when the issue was first raised [95, 96]. The too-big-to-fail problem refers instead to the existence of simulated subhalos that are so massive and dense that they should inevitably have formed visible dwarf galaxies, yet no luminous counterparts are observed.

Lastly, another discrepancy was identified in the predicted self-similarity of the cosmological structures. Halos of galaxies in the same mass range should look alike in their inner dynamics [81, 97]; observations suggest instead a great variety. Some galaxies rise steeply (as predicted), others rise very slowly (suggesting a cored profile), even though they have comparable global properties [98].

A possibility is that baryonic processes themselves may resolve these small-scale challenges without invoking new dark matter physics [99]. For instance, repeated episodes of supernova feedback can expel gas from the central regions of galaxies, leading to rapid fluctuations in the gravitational potential that heat and redistribute dark matter, flattening cusps into cores. Similarly, stellar winds and dynamical friction from baryonic clumps have been proposed as mechanisms capable of reshaping dark matter profiles. However, these baryonic solutions are not without limitations. Simulations show that core formation by feedback is most effective in galaxies with sufficient star formation activity, but it is less clear whether ultra-faint dwarfs can undergo the required level of feedback.

Figure 2.3, adapted from [102], shows the impact of baryonic physics on the inner dark matter densities, plotting the relation between the exponent of the $\rho_{\rm DM}$ radial scaling, α, and the ratio of stellar to halo mass, $M_\star/M_{\rm halo}$ for a series of galaxies. Three different sets of simulations are compared: [100] in green, [101] in blue and [102] in red. The black filled circles represent the simulated FIRE-2 [103, 104] galaxies of [102] and the black open circles are the results for the dark matter only simulations. Both ultra-faint and classical dwarf galaxies retain cuspy slopes ($\alpha \sim -1.5$), consistent with collisionless cold dark matter predictions. Core formation

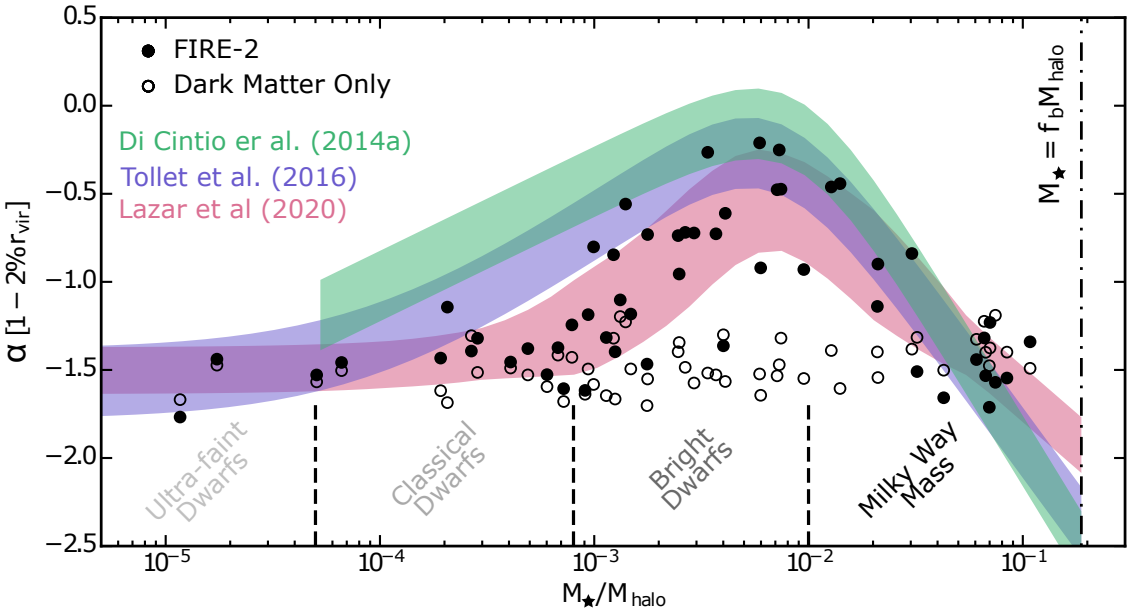

Figure 2.3: Numerical simulations of the impact of baryonic feedback on the inner slope of the dark matter density profile. Shaded area represent three different analysis [100–102], black dots the results of the numerical simulations and black open dots results from dark matter only simulations. Image adapted from [102].

($\alpha \sim -0.25$) emerges around $M_\star/M_{\rm halo} \sim 5 \times 10^{-3}$, but the trend reverses again toward Milky Way-sized systems.

Baryonic mechanisms alone seem to struggle to simultaneously resolve all the small-scale problems across different mass scales without fine-tuning the efficiency of feedback processes. While it is possible to alleviate these discrepancies building ad-hoc stellar initial mass functions, e.g. [105], a possibility is that the cold dark matter paradigm itself may break down on galactic scales. Among the many extensions proposed to address these issues, a particularly relevant candidate is self-interacting dark matter. For comprehensive reviews, see e.g. [99, 106].

This model proposes that dark matter particle scatter with each other through $2 \to 2$ interactions, leading to drastically different predictions for the halo structure. Self-interaction would transport heat from the hotter exterior to the colder interior, thermalizing the inner halo and driving the dark matter particle velocity to a constant

value. This, in turn, would also lead to a reduction of the central density and thus cure the cusp at the centre of the halo. Self-interaction could also affect subhalos, reducing their mass function and solving the missing satellites problem.

To have an effect on the halo, the scattering self interaction per units mass should be at least $\sigma/m \sim 1\,\mathrm{cm}^2\,\mathrm{g}^{-1}$, corresponding to at least one scattering per particle over a 10 Gyr period. Self-interaction is therefore negligible during structure formation in the early universe, retaining the success for the cold mark matter model at large scale and only affecting small scale structures at late times.

Colpi Model As an example, chosen both for its simplicity and for its use in Chapter 3, we consider the Colpi model [107]. Matter is described as a real scalar field undergoing spontaneous symmetry breaking, forming a self-gravitating bosonic superfluid condensate. We start from the Lagrangian density

$$\mathcal{L} = D_\alpha \phi D^\alpha \phi - m_{\mathrm{DM}}^2 \phi^2 - \lambda \phi^4, \tag{2.1}$$

where the covariant derivative is $D_\alpha = \partial_\alpha - i\mu\delta_{\alpha 0}$, the parameter μ is identified with the chemical potential, m_{DM} is the boson mass, and λ the self-interaction strength. In this work, we exclusively consider the case of repulsive self-interactions, corresponding to $\lambda > 0$. This choice is due to fundamental stability requirements. For a scalar field theory described by a potential truncated at the quartic term, a negative coupling constant (attractive interaction) would render the potential unbounded from below for large field values. To consistently model attractive interactions, the Lagrangian would require higher-order stabilizing terms (e.g., $\propto |\phi|^6$), which goes beyond the scope of the minimal model considered here. Furthermore, from an astrophysical perspective, repulsive self-interactions are essential for generating the pressure support needed to stabilize compact objects with masses comparable to neutron stars. Attractive interactions, by contrast, generally reduce the maximum stable mass and induce gravitational collapse at much lower mass thresholds.

Expanding the covariant derivative and using the identity $\delta_{\alpha 0}\delta^{\alpha 0} = -1$, Eq. (2.1)

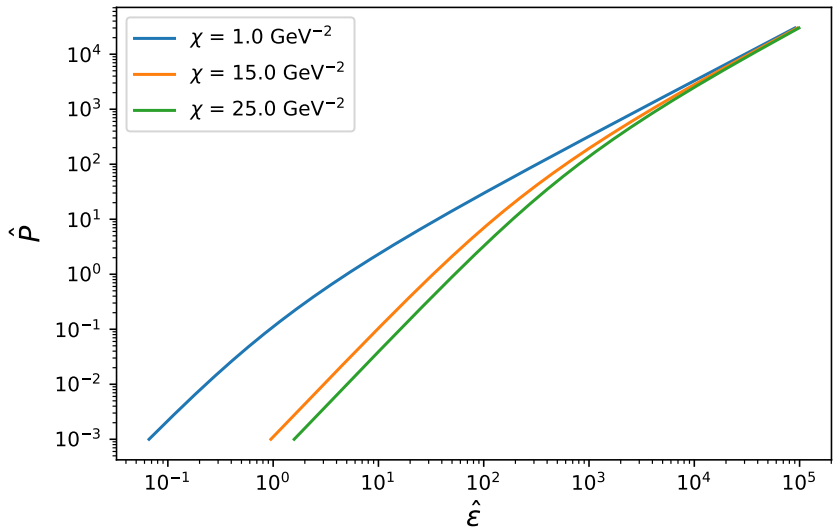

Figure 2.4: Colpi equation of state for different values of the ratio $\chi = m_{\rm DM}^4/\lambda$, defined such that both $\hat{P} = P/\chi$ and $\hat{\varepsilon} = \varepsilon/\chi$ are dimensionless.

can be rewritten as the sum of a kinetic term $\partial_\alpha\phi\partial^\alpha\phi$ and an effective potential

$$V = (m_{\rm DM}^2 - \mu^2)\phi^2 + \lambda\phi^4. \tag{2.2}$$

Following the standard symmetry breaking procedure, we minimise the potential by solving $\partial V/\partial|\phi| = 0$, obtaining

$$\phi^2 = \begin{cases} \dfrac{\mu^2 - m_{\rm DM}^2}{2\lambda}, & \text{if } |\mu| \geq m_{\rm DM}, \\ 0, & \text{if } |\mu| < m_{\rm DM}, \end{cases} \tag{2.3}$$

where the second solution corresponds to the unbroken phase and will not be of interest here.

We now turn to the stress-energy tensor, which in quantum field theory is defined in terms of the Lagrangian as

$$T^{\alpha\beta} = 2\frac{\partial\mathcal{L}}{\partial g_{\alpha\beta}} - g^{\alpha\beta}\mathcal{L} \equiv 2\partial^\alpha\phi^*\partial^\beta\phi - g^{\alpha\beta}\mathcal{L}. \tag{2.4}$$

Comparing this with the perfect fluid form in Eq. (1.1), we can extract the energy density and pressure as

$$\begin{aligned} \varepsilon &= T_{\alpha\beta} u^\alpha u^\beta, \\ P &= \tfrac{1}{3} \left(g_{\alpha\beta} + u_\alpha u_\beta \right) T^{\alpha\beta}, \end{aligned} \tag{2.5}$$

which, together with the condition $\partial_\alpha \phi = 0$ and Eqs. (2.3) and (2.4), yield the equation of state:

$$P = \frac{1}{4\lambda} \left(\mu^2 - m_{\mathrm{DM}}^2 \right)^2 , \tag{2.6}$$

$$\varepsilon = 3P + 2 m_{\mathrm{DM}}^2 \sqrt{\frac{P}{\lambda}}, \tag{2.7}$$

$$n = \frac{\mu}{\lambda} \left(\mu^2 - m_{\mathrm{DM}}^2 \right) , \tag{2.8}$$

$$h = \log \left(\frac{\mu}{m_{\mathrm{DM}}} \right) . \tag{2.9}$$

representing, respectively, the fluid pressure, energy density, number density and specific enthalpy. Figure 2.4 shows three possible realizations of the equation of state, plotting the dimensionless pressure $\hat{P} = P/\chi$ as a function of the dimensionless energy density $\hat{\varepsilon} = \varepsilon/\chi$; the normalization constant χ is defined as $\chi = m_{\mathrm{DM}}^4/\lambda$, and allows to write Eqs. (2.6) to (2.9) as a function of only one parameter.

This simple, analytically tractable equation of state provides a convenient model for the dark matter component in the next chapters. It is worth noting that, for the parameter space explored in this work, the bosonic dark matter equation of state remains consistently softer than the stiff hadronic models (such as DD2) at supranuclear densities. In this regime, the dark fluid generates significantly less pressure for a given energy density compared to the baryonic component. Although the two fluids interact only gravitationally, the presence of this softer, highly compressible component deepens the stellar gravitational potential without providing commensurate pressure support. This forces the baryonic fluid to compress further to maintain hydrostatic equilibrium, ensuring that the qualitative results remain robust across

the considered configurations.

Self-interaction cross section To make contact with the usual self-interaction constraints, it is instructive to compute the $2 \to 2$ scattering cross section directly from Eq. (2.1). Although this regime does not describe the condensed fluid relevant for our stellar models, the experimental bounds on self-interaction, $\sigma/m \lesssim 1\,\mathrm{cm}^2\,\mathrm{g}^{-1}$, is derived in galaxy clusters from the scattering of dilute, nonrelativistic particles. It is important to emphasize that this calculation relies on a perturbative expansion around the vacuum state, valid only in the dilute limit where the mean inter-particle distance is large compared to the scattering length. This is the relevant regime for comparing the model parameters against astrophysical constraints derived from galactic halos and galaxy clusters (e.g., the Bullet Cluster), where dark matter densities are low.

However, the physical conditions inside the compact stars considered in the following chapters are drastically different. There, the dark matter density is high and the field acquires a large vacuum expectation value, forming a Bose-Einstein condensate. In this high-density regime, the perturbative cross-section derived below is no longer a valid description of the particle dynamics. Instead, the system is governed by many-body effects and collective excitations. Fortunately, the computation of the stellar structure in hydrostatic equilibrium relies solely on the thermodynamic properties of the fluid, i.e., the equation of state derived in Eqs. (2.6) to (2.9). This equation of state is obtained within the mean-field approximation, which correctly captures the non-perturbative behaviour of the condensate and remains valid at the high densities encountered in the stellar core.

At tree level, the only contributing diagram is the quartic contact interaction shown in Fig. 2.5, with amplitude

$$\mathcal{M} = -i\,24\lambda. \tag{2.10}$$

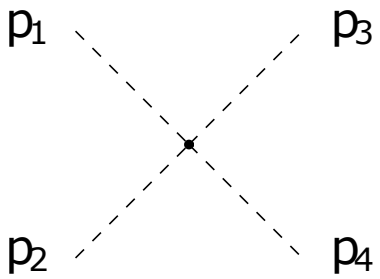

Figure 2.5: Tree-level Feynman diagram for $2 \to 2$ scattering in the real scalar ϕ^4 theory. The interaction proceeds via the quartic contact vertex with coupling λ.

In the centre-of-mass frame, the differential cross section for two identical scalars is

$$\frac{\mathrm{d}\sigma}{\mathrm{d}\Omega} = \frac{|\mathcal{M}|^2}{128\pi^2 s}, \tag{2.11}$$

where s is the Mandelstam variable, approximated in the nonrelativistic limit as $s \simeq 4m_{\mathrm{DM}}^2$. Integration over the solid angle yields

$$\frac{\sigma}{m_{\mathrm{DM}}} = \frac{9\lambda^2}{2\pi m_{\mathrm{DM}}^3}. \tag{2.12}$$

While in Chapter 3, where only the ratio χ enters and no explicit benchmark values were required, we adopted the equation of state in the notation shown above, in Chapters 4 and 5 we follow the more conventional choice $m_{\mathrm{DM}}^2 \to m_{\mathrm{DM}}^2/2$ and $\lambda \to \lambda/4$. This redefinition changes the vertex normalization and introduces an additional factor of 16 in the denominator of the cross section. For the benchmark values adopted there, $(m_{\mathrm{DM}}, \lambda) = (1\,\mathrm{GeV}, 24\pi)$ and $(250\,\mathrm{MeV}, 24\pi)$, this corresponds to $\sigma/m_{\mathrm{DM}} = 0.11\,\mathrm{cm}^2\,\mathrm{g}^{-1}$ and $\sigma/m_{\mathrm{DM}} = 7.12\,\mathrm{cm}^2\,\mathrm{g}^{-1}$, respectively. The first value is within current bounds, while the second slightly exceeds them. This does not affect our conclusions, however, because the stellar models in the following chapters depend exclusively on the mean-field equation of state Eqs. (2.6) to (2.9), appropriate for a zero-temperature condensate. The bounds on σ/m constrain vacuum scattering in dilute halos and do not enter the stellar structure problem. Moreover, since the equation of state depends only on the ratio $m_{\mathrm{DM}}^4/\lambda$, the parameters can always be

rescaled as

$$(m,\, \lambda) \;\longrightarrow\; (m',\, \lambda' = \lambda(m'/m)^4), \tag{2.13}$$

which leaves the equation of state (and thus all stellar predictions) unchanged, while rescaling the scattering cross section as

$$\left(\frac{\sigma}{m}\right)' = \left(\frac{m'}{m}\right)^5 \frac{\sigma}{m}. \tag{2.14}$$

Any benchmark point can therefore be mapped to an equivalent pair that satisfies a desired halo constraint, ensuring the robustness of the stellar results.

2.2 Dark matter-admixed neutron stars

Given the model presented above, it follows that in the presence of a strong gravitational field, self-interacting dark matter could be captured and form stable self-gravitating structures, provided a balancing force is present (e.g., degeneracy pressure or repulsive interactions). In particular, we focus on accretion around a neutron star.

The first point to analyse is how dark matter can be accreted by a neutron star. One of the primary mechanisms is gravitational capture: as the star orbits around the galaxy, it encounters fluxes of dark matter particles. Interactions (either purely gravitational or via direct scattering) with stellar matter can lead to energy loss, eventually allowing dark matter particles to become bound to the star's gravitational field. For a dark matter particle, regardless of its microscopic nature, an estimate of the capture rate is given by [108]

$$\dot{M} = \rho_\chi v_\chi \pi b^2 P_V P_\sigma, \tag{2.15}$$

where the overdot denotes a time derivative, ρ_χ the local dark matter density, v_χ the velocity of the dark matter particle at infinity, πb^2 the effective scattering cross-section with impact parameter b, P_V the probability that the particle χ becomes bound, and P_σ the probability of scattering.

Particularly important are ρ_χ and v_χ, which may vary significantly across cos-

mic regions. For example, in the Solar neighbourhood one typically assumes $\rho_\chi \approx 0.4\,\mathrm{GeV\,cm^{-3}}$ and $v_\chi \approx 300\,\mathrm{km\,s^{-1}}$ [72], leading to a flux of approximately $\dot{M} \approx 3 \times 10^{25}\,\mathrm{GeV\,s^{-1}}$, or equivalently around $53\,\mathrm{g\,s^{-1}}$, as estimated in [108]. Importantly, Eq. (2.15) implicitly depends on the dark matter particle mass through the scattering probability P_σ. There is also a lower bound on the particle mass set by the neutron star's core temperature: if the dark matter mass is too small, thermal energy transfer can provide the particle with sufficient kinetic energy to escape the star's gravitational potential.

Beyond steady-state capture mechanisms, several astrophysical and cosmological channels can lead to the formation of a neutron star with a substantial dark component already at birth [109]. One possibility is dark matter production during the supernova explosion itself [110, 111]. The extreme temperatures ($T \sim 10 \div 100\,\mathrm{MeV}$) and densities reached in the proto-neutron star phase may enable efficient dark matter generation, with a fraction of the produced particles becoming gravitationally trapped during the rapid collapse of the outer shells. Another channel involves the accretion of primordial dark clumps, i.e. small-scale bound structures that may have formed in the early Universe. A compact object passing through such a clump can inherit an already concentrated dark matter component. Typical clump masses and densities are highly model-dependent, but in general the effective local dark matter density can exceed the smooth-halo value by many orders of magnitude, greatly enhancing accretion [111, 112]. Finally, star formation itself can proceed around a preexisting dark core [111, 113]. If baryonic collapse occurs inside a potential well dominated by dark matter, the proto-stellar cloud may settle around a central dark matter concentration, so that the newborn neutron star is effectively born embedded in a dense dark environment.

Moreover, local non-homogeneities in the dark-matter distribution, whether produced by hierarchical structure formation or the survival of compact primordial overdensities, can further increase the dark matter fraction around individual compact objects [113–119]. In extreme cases this can lead to the formation of purely dark compact objects often termed "dark stars" [120, 121].

Taken together, these formation and environmental channels imply that the

capture-only picture can drastically underestimate the possible dark content of some neutron stars. Quantitatively, while smooth-halo capture in the Solar neighbourhood might lead to accumulated masses of order $10^{-10} \div 10^{-15}\,M_\odot$ over Gyr timescales (depending on cross-sections and particle mass), formation-seeded scenarios or passages through dark matter spikes can plausibly raise this by orders of magnitude, in extreme cases approaching orders of a per cent of the star's mass on astrophysical timescales, with correspondingly large effects on structure and evolution.

The thermal evolution of dark matter-admixed neutron stars differs markedly from that of ordinary neutron stars because of the changes that dark matter induces in the stellar composition, density distribution, and heat transport. Even if the dark component interacts with baryons only through gravity, its presence modifies the conditions under which neutrino-emitting reactions operate. In particular, the inward pull of a dense dark core tends to compress the baryonic fluid and increase the central proton fraction. This can lower the threshold mass at which the direct Urca process becomes kinematically allowed, producing a transition from slow to rapid cooling at significantly smaller stellar masses [122]. In stars where the dark matter fraction is small and distributed in a dilute halo, the opposite occurs: the nuclear core is partially diluted, the central density decreases, and the direct Urca reactions are suppressed, leading instead to slower cooling dominated by modified Urca and nucleon bremsstrahlung processes.

At early times, when neutrino emission dominates the energy loss, the interplay between density compression and proton pairing determines whether a dark matter-admixed neutron stars cools along a "fast" or "standard" track. Numerical simulations based on realistic nuclear equations of state and self-gravitating fermionic dark matter show that even a few per cent of dark mass can shift the critical density for the direct Urca onset by tens of per cent [123]. The resulting surface temperatures after $10^4 \div 10^5$ yr may therefore differ by up to an order of magnitude compared to pure neutron stars of the same total mass. In configurations where the dark matter forms an extended halo, the thermal coupling between the baryonic crust and the outer dark layers can also delay the internal relaxation phase, producing a prolonged plateau in the observable luminosity curve [124].

If the dark sector is self-interacting, the qualitative trends remain the same as in the collisionless case but are quantitatively amplified. Repulsive self-interactions stiffen the dark equation of state, partially counteracting the gravitational compression of the baryonic core. For a given dark-mass fraction, this results in larger dark volumes and a weaker enhancement of the central proton fraction compared with the collisionless case [123, 125]. In the limit of strong self-repulsion, the effect even reverses: the star becomes less compact and cools more slowly, demonstrating that SIDM essentially extremizes the same structural influence already produced by collisionless dark matter.

At later epochs, when photon emission from the surface dominates, the smaller radius and higher compactness typical of dark matter core stars further accelerate the decline in luminosity, while in dark matter halo stars the opposite effect can yield warmer late-time temperatures. Observationally, unusually cold young neutron stars or, conversely, warm old remnants may both hint at substantial dark admixtures, making thermal evolution studies a sensitive probe of dark matter in compact objects.

Equilibrium configurations Equilibrium configurations, due to the low scattering cross-section of dark matter with normal matter, can be described using the multifluid formalism presented in Section 1.3 with $N = 2$.

The presence of a significant dark matter component alters the equilibrium properties of a neutron star. Depending on the particle mass and interaction strength, dark matter can form two stable configurations: either as a dense core at the centre of the star or as an extended halo surrounding it [128]. In general, and particularly in the core case, the dark matter contributes as an additional source of gravitational pull on the baryonic matter while providing negligible internal pressure. The net effect is a reduction of the maximum mass sustainable by a stable configuration and, for fixed gravitational mass, a reduction of the neutron star radius.

This behaviour is illustrated in the left panel of Fig. 2.6, which shows equilibrium sequences parametrized by the baryonic central energy density for four different baryonic equations of state, with dark matter described by the bosonic model of Section 2.1. The dark matter self-interaction strength is set to $\lambda = 24\pi$: this choice is

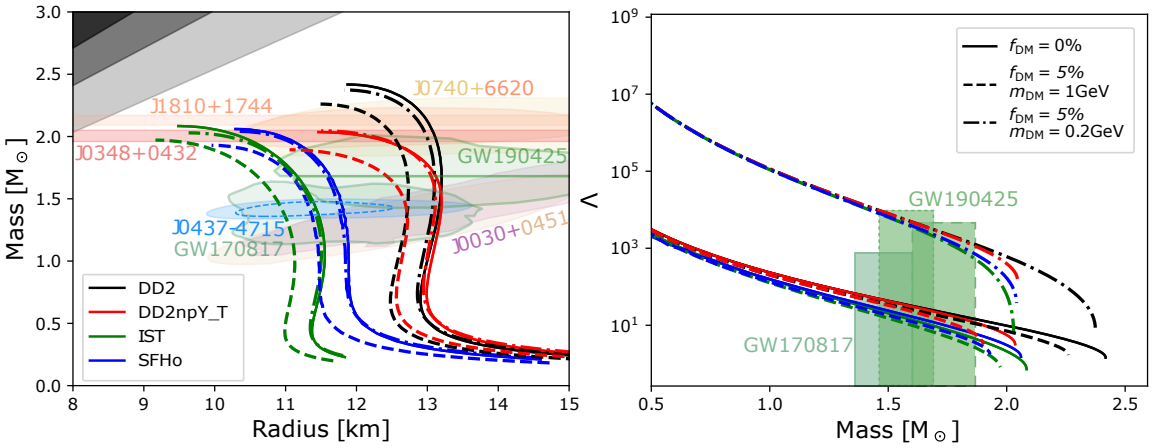

Figure 2.6: Left: Mass-radius relations for different equations of state of the baryonic matter. Solid lines report the pure baryonic matter case, dashed lines include a dark matter fraction of 5% and mass $m_{\rm DM} = 1\,\text{GeV}$ (core configurations) while dash-dotted line the same fraction and a particle mass $m_{\rm DM} = 0.2\,\text{GeV}$ (halo configurations). The gray shaded areas represent the GR limit $R > 2M$, finite pressure condition $R > 9M/4$ and causality condition $R > 8M/3$, respectively. The pink and light red bands represent the 1σ constraints on the mass of PSR J1810+1744 [22], and PSR J0348+0432 [21]. The NICER measurement of PSR J0030+0451 [18, 19] is shown with the purple and yellow contours, the gold and orange contours represent the PSR J0740+6620 measurement [24, 25], while light blue (95% CL) and light blue dashed (68% CL) contours represent the PSR J0437-4715 measurement [26]. LIGO-Virgo detections of GW170817 [2] and GW190425 [30] binary NS mergers are shown in light green. **Right:** Tidal deformability-mass relations for the same equations of state of the previous panel. The same line pattern applies. The boxes represents the 90% confidence upper bound from GW170817 [126] and the two bounded by dashed lines correspond to the same bounds for the primary and secondary compact objects of GW190425 [30, 127] (assuming low-spin priors).

arbitrary and made in order to obtain in the nonrotating core limit a maximum mass close to $2\,\text{M}_\odot$. The abscissa corresponds to the radius of the baryonic star, the only directly observable quantity, while the ordinate reports the total gravitational mass $M_{\rm tot} = M_{\rm BM} + M_{\rm DM}$. Different colours correspond to different baryonic equations of state: DD2 [33], DD2npY-T [35], IST [36, 37], and SFHo [129–131]. Solid lines represent the one-fluid case. Dashed lines show systems characterized by a total dark

matter content equal to 5% of the total gravitational mass [109] and a dark matter particle mass of 1 GeV, corresponding to the formation of a core. Lastly, dash-dotted lines show systems with the same dark matter fraction but a dark matter particle mass of 200 MeV, corresponding to the formation of an halo.

The presence of dark matter effectively softens the baryonic equation of state. This effect is not unique to bosonic dark matter: for instance, a fermionic component with interactions mediated by a dark scalar and/or vector field produces qualitatively similar shifts in the mass-radius relation.

This behaviour can be explained looking at the local propagation of pressure perturbations within the two-fluid system. In configurations where the two components interact only through gravity, the total pressure response to density variations can be described by an effective speed of sound lying between those of the baryonic and dark fluids, $c^2_{s,\mathrm{eff}} = \eta\, c^2_{s,\mathrm{BM}} + (1-\eta)\, c^2_{s,\mathrm{DM}}$ [132], where η quantifies the relative contribution of each component to the total compressibility. Because bosonic dark matter is characterized by a particularly low sound speed, $c^2_{s,\mathrm{DM}} \lesssim 0.1$, regions containing a significant dark fraction exhibit a smaller $c_{s,\mathrm{eff}}$ than the purely baryonic case. The pressure support therefore reacts more weakly to compression, leading to an effective softening of the combined equation of state and to the systematic reduction in maximum mass and radius observed in Fig. 2.6. The same argument holds for any two-fluid mixture with negligible non-gravitational coupling and therefore represents a general property of multifluid equilibrium rather than a model-specific feature of bosonic dark matter.

The right panel of Fig. 2.6 shows, for the same configurations, the dimensionless tidal deformability Λ computed from Eq. (1.19) as a function of the total mass. In these calculations, the radius R is taken to be the outermost radius between the two fluids. For a fixed gravitational mass, the presence of a dark matter core lowers the tidal deformability. This follows directly from the scaling $\Lambda \propto \left(\frac{M}{R}\right)^{-5}$: the reduction in radius dominates over the reduction in mass, so that the compactness increases and Λ decreases accordingly. This behaviour again mimics a softening of the equation of state. In contrast, the formation of a dark matter halo increases the outermost radius, and thus enhances Λ.

However, without additional observational evidence, the mass-radius-Λ curves alone are not sufficient to unambiguously identify dark matter admixed neutron stars. Within plausible choices of dark matter parameters, such systems remain degenerate with purely hadronic equations of state. In many cases, the dark matter fraction is too small to yield appreciable effects, or current observational uncertainties are large enough to accommodate both scenarios, as illustrated in both panels of Fig. 2.6. The apparent softening of the equation of state could equally well originate from nuclear physics effects, such as a phase transition to quark matter or the emergence of hyperonic degrees of freedom.

Chapter 3

Superfluid dark stars

This chapter has been published in near-identical form.
Phys. Rev. D **110**, L021301 - **Published 8 July, 2024**
DOI: https://doi.org/10.1103/PhysRevD.110.L021301

Boson stars [133–135] are hypothetical objects entirely made of bosons, see [136–138] for reviews. The idea originated from the work of Wheeler on geons [139], appropriately adapted to Einstein-Klein-Gordon solitons. Indeed, in the literature boson stars are mainly identified with localized solitonlike configurations stabilized by gravity [133, 134, 140–143]. They can be viewed as macroscopic quantum systems subject to their own gravitational attraction where the collapse is typically prevented by the Heisenberg uncertainty principle. In solitonlike stars, interactions significantly determine the stellar configuration but do not play an essential role in their gravitational stability.

In this chapter we discuss the equilibrium configuration of a fluid of self-interacting dark matter bosons subject to their own gravitational attraction. Besides the gravitational pull, bosons statistically attract each other, hence a short-range repulsion is needed to prevent the collapse. Such approach parallels the observation that stable stars made of charged pions [144–147] may be realized if the pion electric charge is balanced [148]. In that case, the configuration is not a soliton, but can be viewed as a standard gas of self-gravitating matter.

The focus is on a simple system of dark bosons, completely decoupled from the Standard Model. We assume that the system features a global number symmetry that is spontaneously broken, so that a superfluid is formed. The interparticle repulsion is modelled by a two-body self-interaction [149, 150], allowing to determine analytically the equation of state (EoS). In the low-temperature limit, hydrostatically stable configurations, hereafter superfluid dark stars, have masses and radii linearly scaling with the ratio between the square root of the self-coupling and the square of the boson mass.

Since superfluid dark stars have arbitrarily low masses, they are compatible with the possible observation of low-mass compact objects. For instance, the component masses in the SSM200308 merger event [151] are estimated to be $M_1 = 0.62^{+0.46}_{-0.20}\, M_\odot$ and $M_2 = 0.27^{+0.12}_{-0.10}\, M_\odot$, with $M_\odot$ the solar mass. Such low masses challenge the standard paradigm of hadronic compact stars [152–157] originating from supernova explosion [152, 158–160].

This chapter addresses the tidal deformability and studies numerically the evo-

lution of equal-mass binary systems, considering canonical $1.4M_\odot$, as well as lighter $0.6M_\odot$, masses. The results include the corresponding gravitational waveforms and amplitude spectral densities, as well as an estimate of the ejected matter.

The astrophysical formation of superfluid dark star binaries represents an interesting scenario in the context of self-interacting dark matter. While these objects have not yet been observationally confirmed, their formation could be rooted in primordial density perturbations that decouple from the expansion of the early universe, eventually undergoing gravitational collapse into compact clumps. Alternatively, in the late-time universe, dark sector interactions might provide dissipative mechanisms allowing dark matter halos to fragment into stellar-mass structures. Within high-density environments, such as galactic centres or dense sub-halos, dynamical capture could facilitate the assembly of the binary systems studied in this work. Investigating the merger of such systems thus provides a proactive strategy to identify unique gravitational signatures that could distinguish exotic dark matter structures from standard baryonic compact stars.

We use natural units $\hbar = c = G_N = 1$.

3.1 Hydrostatic equilibrium

To describe bosonic matter, use is made of the model described in Section 2.1. Knowing the EoS, one can determine the hydrostatic equilibrium configuration for non-rotating mass distributions by solving the spherical Tolman-Oppenheimer-Volkoff (TOV) equations [6, 7]. To this end, the following rescaling is useful

$$\epsilon = \frac{m_{\rm B}^4}{\lambda}\hat{\epsilon}\,, \qquad P = \frac{m_{\rm B}^4}{\lambda}\hat{P}\,, \tag{3.1}$$

$$r = \frac{\sqrt{\lambda}}{m_{\rm B}^2}\hat{r}\,, \qquad M = \frac{\sqrt{\lambda}}{m_{\rm B}^2}\hat{M}\,, \tag{3.2}$$

where r is the radial distance from the origin and $M \equiv M(r)$ is the gravitational mass within r. Both $\hat{\epsilon}$ and $\hat{P}$ are dimensionless in natural units. Upon substituting

the above expressions in Eq. (2.7), we have the dimensionless EoS

$$\hat{\epsilon} = 3\hat{P} + 2\sqrt{\hat{P}}\,, \tag{3.3}$$

while the TOV equations are

$$\frac{d\hat{M}}{d\hat{r}} = 4\pi\hat{r}^2\hat{\epsilon}\,, \qquad \frac{d\hat{P}}{d\hat{r}} = (\hat{\epsilon}+\hat{P})\frac{\hat{M}+4\pi\hat{r}^3\hat{P}}{2\hat{M}\hat{r}-\hat{r}^2}\,, \tag{3.4}$$

which can be solved for a given central energy density, $\hat{\epsilon}_0$. Differently from solitonic-like stars [136–138], superfluid dark stars have a well-defined radius, R, determined by the vanishing pressure condition [152]. The gravitational mass is $M(R)$.

In Fig. 3.1 are shown the mass-radius diagrams of the superfluid dark stars for different values of

$$x = \frac{\sqrt{\lambda}}{m_{\rm B}^2}\,, \tag{3.5}$$

which is the parameter determining the scaling of masses and radii in Eqs. (3.2). These results are compared with those obtained using few hadronic EoSs. For given x, lowering the central density, the mass decreases while the radius increases. In the low density limit, the EoS (2.7) is approximated by the polytrope $P = \frac{x^2}{4}\epsilon^2$ so that the radius is given by $R = x\sqrt{\frac{\pi}{8}}$, which is confirmed in Fig. 3.1 for vanishing M. It is also found that at low densities M scales linearly with the central density.

The maximal mass of superfluid dark stars scales linearly with x, reaching the neutron star observational limit of about $2.1M_\odot$, for $x \simeq 20$ GeV^{-2}. Compared to hadronic EoSs, the corresponding stellar radius is here about a factor 2 larger. Since both R and M scale linearly with x, extremely massive superfluid dark stars have radii much larger than standard NSs. On the other extreme, if x is very small, light clumps of superfluid dark matter with very small radii may be realized. This would happen for small values of λ and/or for heavy dark bosons, namely large $m_{\rm B}$.

The thin straight lines in Fig. 3.1, indicate two different values of the stellar compactness, $\mathcal{C} = M/R$. Given the scaling in Eq. (3.2), the compactness is independent of x, therefore these lines join configurations with the same dimensionless central

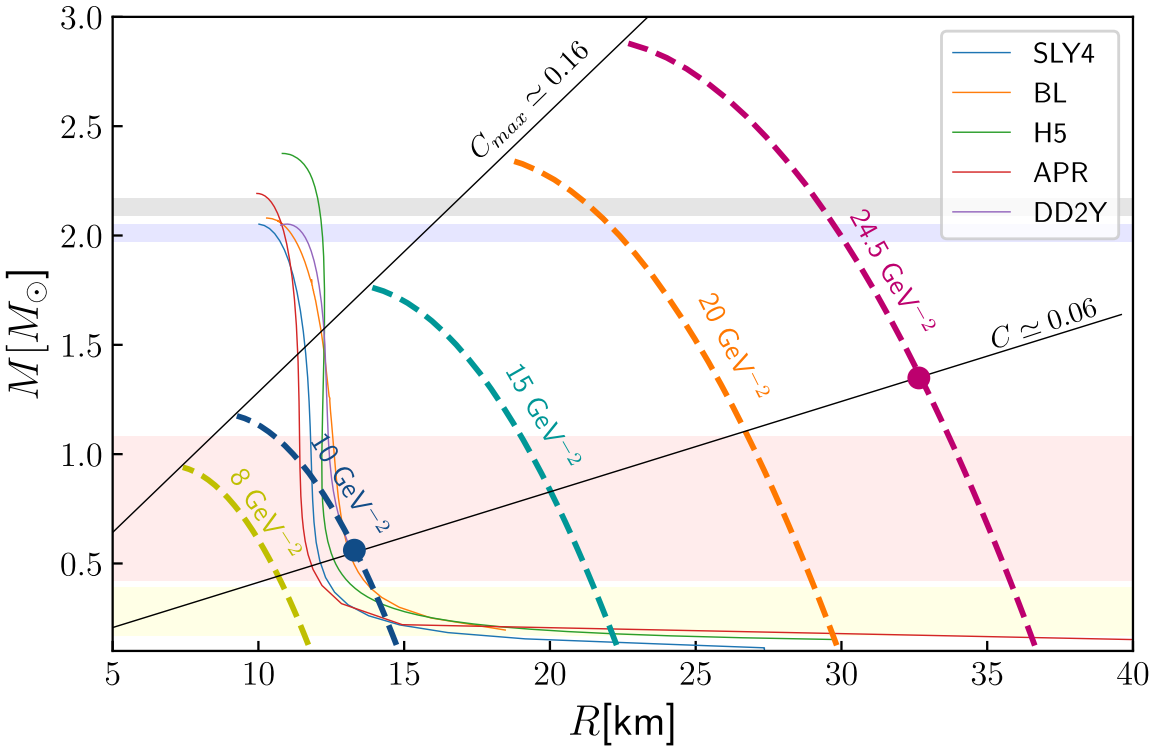

Figure 3.1: Masses and radii of superfluid dark stars for different $x = \sqrt{\lambda}/m_{\rm B}^2$ (dashed) compared with various hadronic EoSs (solid) [33, 161–164]. The top gray (blue) band corresponds to the observational limits on pulsar masses in [22]([21]). The bottom pink and yellow bands show the component masses in the SSM200308 event [151]. The dots correspond to the configurations used in the merger simulations. The two thin straight lines indicate the maximum compactness (upper line) and the one used in the merger simulations (lower line).

energy density but different x. Since $M \propto \hat{M}\, x$ and $\epsilon \propto \hat{\epsilon}\, x^{-2}$, stars having the same compactness but larger masses (and radii) have smaller central densities. The maximum compactness is $\mathcal{C}_{\rm max} \simeq 0.16$, which is smaller than the values obtained with hadronic matter—the dark boson EoS is relatively soft. Thanks to this upper limit, future evidence of higher compactness may rule out superfluid dark stars obtained with Eq. (2.1). Higher compactness can be obtained with different contact interactions [169]. Such a measurement should result from gravitational observations since dark bosons are not expected to emit light. Hence, bounds from NICER [19] as well

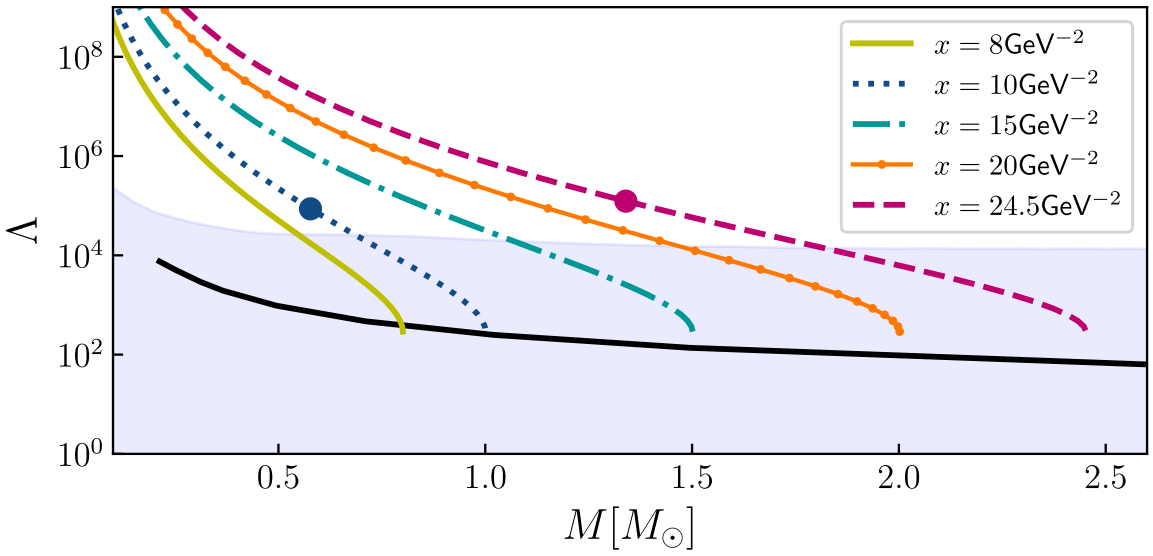

Figure 3.2: Dimensionless tidal deformability Λ, see Eq. (3.6), as a function of the stellar gravitational mass M. For any x in Eq. (3.5), the curves are obtained changing the dimensionless central energy density. The lowest value $\Lambda_{\rm min} \simeq 290$ is reached for the maximal mass, while Λ diverges for low masses. The dots correspond to the configurations used in the merger simulations. The shaded area delimits the 3σ upper bound at fixed signal to noise ratio SNR$=12$ in the O4 observational run in LVK [165–167]. The black line corresponds to the 1σ tidal deformability at 100 Mpc for the $\Delta - 10$ km HFLF-Cryo configuration of ET [168].

as from GW170817 [1], which was followed by a kilonova [170], cannot constrain the present model.

Another possibility is to assess the existence of superfluid dark stars by tidal deformation measurements. The tidal Love number k_2 is calculated as in [28, 29, 171, 172]: it ranges from about 0.045 to 0.25 for decreasing compactness. In Fig. 3.2, the plot shows the mass dependence of the dimensionless tidal deformability parameter

$$\Lambda = \frac{2}{3\mathcal{C}^5}\, k_2\,, \tag{3.6}$$

together with the expected reach of the O4 run at Ligo-Virgo-Kagra (LVK) [165, 166] and the estimated sensitivity of the Einstein Telescope (ET) [168]. It is observed that for each value of x there is a range of masses for which a measurement should

be possible. In particular, ET should be able to probe the entire range of tidal deformabilities of superfluid dark stars. For vanishing masses, all Λ curves in Fig. 3.2 diverge. Toward maximal M, the lowest value $\Lambda_{\rm min} \simeq 290$ is obtained, regardless of x, consistent with the fact that the external part of the star can be described by a $\Gamma \simeq 2$ polytrope [29]. The two dots correspond to the stars used in the merger simulations. Since these two configurations have similar dimensionless central densities $\hat{\epsilon}_0 \sim 10^{-4}$, they also have similar tidal deformabilities $\sim 10^5$. It should be remarked that as Einstein's equations for a superfluid dark star can be written in dimensionless units with the appropriate rescaling of Eqs. (3.1) and (3.2), it is expected that the value of any dimensionless observable, e.g. the tidal deformability, at fixed central density, $\hat{\epsilon}_0$, should be independent of x.

3.2 Binary Mergers

Considering dark bosons decoupled from Standard Model particles, the only way to probe superfluid dark stars is by their gravitational effects [173], see however the discussion in [174] for possible light emission mechanisms.

In the context of solitonlike models, merging of boson stars was considered in [175–177]. In this section, the merging is studied for two equal-mass inspiraling superfluid dark stars, with compactness $\mathcal{C} \simeq 0.06$, corresponding to the two dots in Figs. 3.1 and 3.2. The first simulation is done with stars having constituent mass[1] $M_b \simeq 1.4\,M_\odot$ and radius $R \simeq 32.5\,$km at an initial distance of 90 km, while the second has stars with $M_b \simeq 0.6\,M_\odot$ and $R \simeq 13.1\,$km at an initial distance of 50 km.

The dynamical evolution of the binary systems is performed using the open-source EINSTEIN TOOLKIT [178], which is built upon the component-based CACTUS framework [179, 180]. The computational domain is discretized using the adaptive mesh refinement (AMR) driver CARPET [181].

We evolve Einstein's field equations in the BSSN formulation [182, 183] using the `McLachlan` module [184]. The gauge conditions are handled via a $1 + \log$ slicing

[1] This is the stellar mass computed integrating the energy density over the proper volume.

condition for the lapse function and a Gamma-driver condition for the shift vector. The general relativistic hydrodynamics equations are solved in the Valencia formulation [185, 186] via the `GRHydro` module [187, 188]. To handle the matter fields, we utilize a high-resolution shock-capturing finite-volume scheme that employs the HLLE Riemann solver [189, 190] combined with the WENO reconstruction method [191, 192]. An artificial atmosphere with a density floor of $\rho_{\rm atmo} \approx 10^{-12} M_\odot^{-2}$ is imposed to handle vacuum regions. Time integration is carried out using the Method of Lines with a fourth-order conservative Runge-Kutta scheme (RK4) and a Courant-Friedrichs-Lewy (CFL) factor of 0.4.

The computational grid consists of 6 levels of fixed mesh refinement. The outer boundary is located at $720\,M_\odot$ ($\approx 1060\,$km) and π-symmetry is applied across the orbital plane. The finest refinement level has a spatial resolution of $\Delta x = 0.375\,M_\odot \approx 553\,$m. This resolution is selected to balance computational feasibility with the physical requirements of the specific systems analysed. For the $1.4\,M_\odot$ models, the stars possess extended radii that are well-resolved at this spacing. For the more compact $0.6\,M_\odot$ models ($R \approx 15\,$km), this resolution covers the stellar radius with approximately 30 grid points. While this is at the lower limit of typical resolution standards for realistic neutron stars, it is sufficient in this context due to the simplified nature of the equation of state. These stars exhibit smooth internal density profiles without the complex, small-scale structural features found in realistic baryonic EOS models, allowing the macroscopic dynamics to be accurately captured. To further verify numerical robustness, we performed a comparison with coarser resolution setups, finding consistent dynamical behaviour.

Figure 3.3 shows a summary of the two simulations. None of the systems collapses to a black hole in the simulated time, as expected from the low value of the compactness. The top panels contain snapshots of the density distribution at different times; the bottom one shows the extracted h_{22} component of the gravitational wave (GW) in magenta and blue for the higher and lower mass respectively– see [193] for detailed extraction procedure. x

For $M_b = 1.4\,M_\odot$, the magenta line in Fig. 3.3(c) shows the typical chirp, followed by the merger and the formation of a bar-deformed remnant. Its imprint on the GW

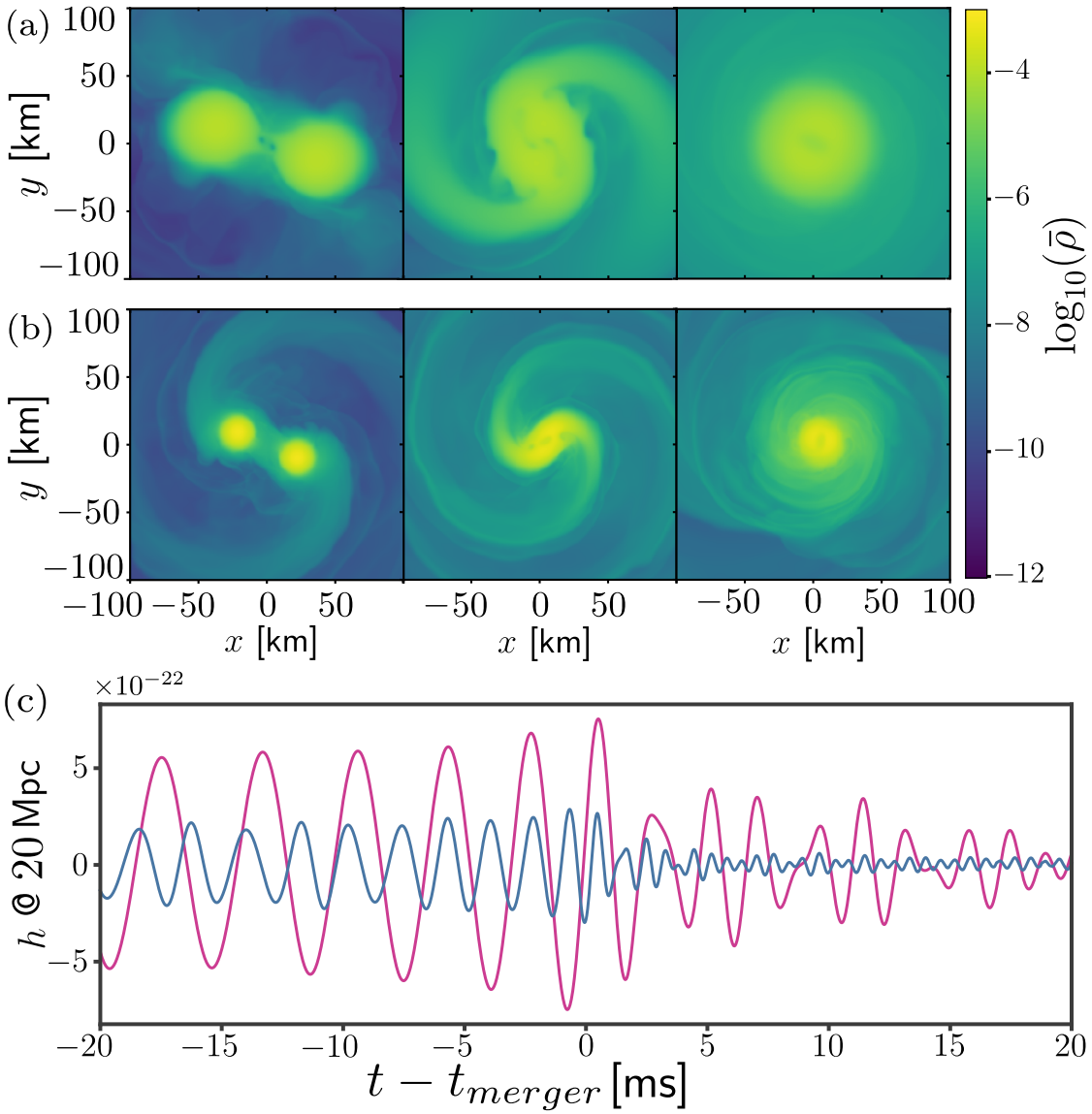

Figure 3.3: Results of the merger simulations. (a-b) Three snapshots of the matter density distribution $\bar{\rho} = \rho G^3 M_\odot^2 c^{-6}$, taken during inspiral, merger and postmerger for $M_b = 1.4\,M_\odot$ (a), and $M_b = 0.6\,M_\odot$ (b). (c) The extracted GW signals in magenta and blue corresponding to (a) and (b), respectively. The merger time $t_{\rm merger}$ is defined as the time at which the gravitational wave strain reaches its maximum amplitude.

can be seen in the spectral density Fig. 3.4(left), where two dominant frequencies appear: one at $f \simeq 475\,\mathrm{Hz}$ and the other at $f \simeq 670\,\mathrm{Hz}$. They turn on in the postmerger phase, as shown by the spectrum of the waveform computed after t_{merger}. It is confirmed that the peaks originate from the $m = 1$ and $m = 2$ matter oscillation modes, see e.g. [194].

For $M_b = 0.6\,M_\odot$, a more peculiar behaviour emerges, see the blue line in Fig. 3.3(c). Somewhat evident are the oscillations due to the residual eccentricity in the initial data. They are expected to be pronounced for soft EoS models and small stellar masses. In order to test the reliability of the method, the residual eccentricity was estimated in the Newtonian approximation (following the distance of one star from the origin, see for instance [195, 196]). The result is about 5×10^{-2}, compatible with residuals from initial data. The right panel in Fig. 3.4 shows the corresponding spectrum. It is qualitatively similar to the left one; the two peaks are only shifted to higher frequencies, $f \simeq 1.1\,\mathrm{kHz}$ and $f \simeq 1.54\,\mathrm{kHz}$, and appear less intense due to the shorter GW signal. The results show that in both simulations the peak frequencies are well within the observational window of LVK [197], and for high mass objects are at lower frequencies with respect to NS mergers [198–200].

The obtained results confirm that for fixed compactness observables scale with x. The ratio of the initial masses (or equivalently, initial radii) is equal to the ratio of the used values of x (in this case, 2.45). The spectral pattern is peaked at frequencies that increase with decreasing x: the peaks in the two plots of Fig. 3.4 have a ratio $\simeq 2.3$. A similar value comes from the minimization of the L_2 norm between the two strains of Fig. 3.3(c), that is given by

$$\arg\min_d \|h_{1.4} - d\,h_{0.6}\|_2 \simeq 2.3\,, \tag{3.7}$$

where d is a scaling factor. A relative error of about 6% may be in part due to differences in the initial data (the exact values of the two compactness differ by $\sim 4\%$) and in part to numerical errors accumulated during the simulations, the extraction procedure and the Fourier transform.

The formation of a disk of ejected matter surrounding the remnant is visible in

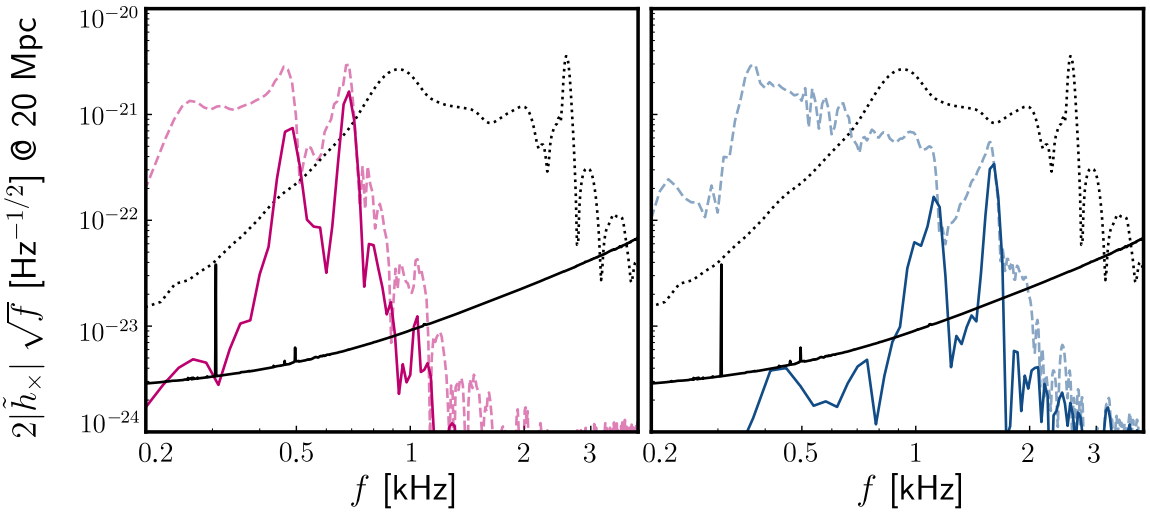

Figure 3.4: Amplitude spectral densities $2|\tilde{h}_\times|\sqrt{f}$ (see e.g. [201]) at 20Mpc for binary merging of equal mass stars, for $M = 1.4(0.6)\,M_\odot$ respectively in the left (right) panel and magenta (blue) lines. Dashed lines represent the spectrum computed considering the entire gravitational wave signal, while solid lines are obtained from the postmerger phase only. The dotted black lines show the spectrum for DD2 EoS [198]. The solid black lines are the sensitivity curve of Advanced LIGO [166].

both Fig. 3.3(a)-(b). Its constituent mass can be computed as the three-dimensional integral of the conserved rest-mass density $D = \sqrt{g}\bar{\rho}\gamma$ [202] from the minimum value to some upper limit $D_{\rm cut}$. Here g is the determinant of the 3-metric g_{ij}, γ the Lorentz factor and $\bar{\rho}$ the density in geometrized units. However, there is no unambiguous way to choose the threshold to separate the remnant from the disk.

To this end, the analysis considers the density profile of the fluid on the XY plane at a time in which the mass density reaches a steady state and the $m = 2$ deformation is subdominant with respect to the overall axial symmetry. Fig. 3.5(left) shows, for both simulations, its average over the entire azimuthal angle

$$D^*(r) = \frac{1}{2\pi}\int_{-\pi}^{\pi} D\,\mathrm{d}\phi\,, \tag{3.8}$$

in magenta for $M_b = 1.4\,M_\odot$ and in blue for $M_b = 0.6\,M_\odot$. Looking at this plot together with the third panel of Fig. 3.3(a) and (b), it is possible to distinguish the

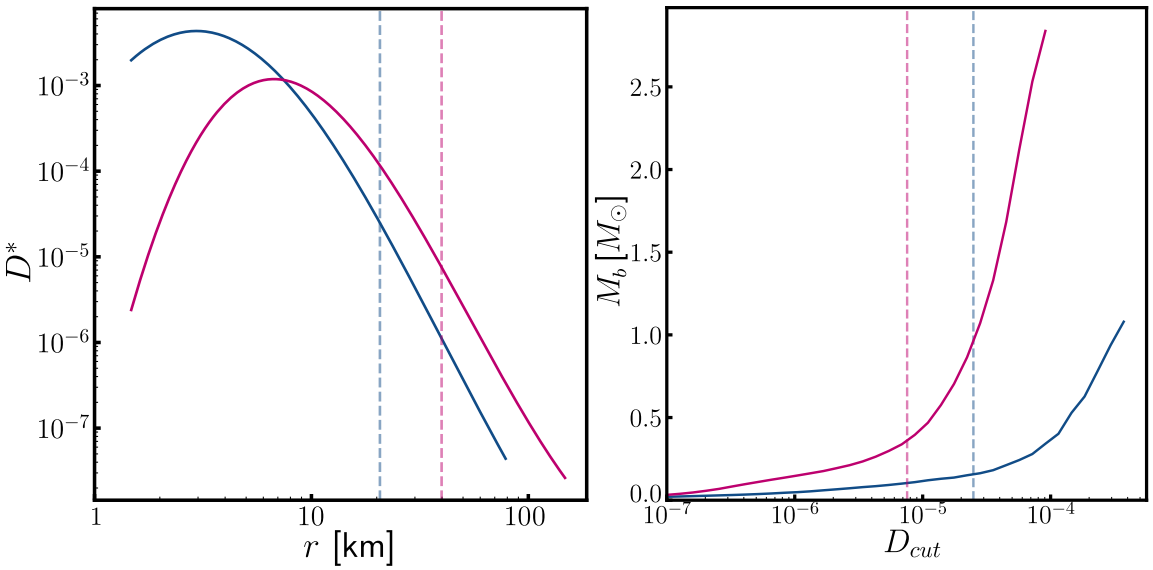

Figure 3.5: Left: azimuthal average of $\bar{\rho}$ as function of the radial distance r. The dashed line represents the radius at which its logarithmic derivative is -4.53 for $M_b = 1.4\,M_\odot$ in magenta and $M_b = 0.6\,M_\odot$ in blue. Right: total constituent mass computed integrating densities up to $D_{\rm cut}$.

main features of the remnant: in the centre there is a region of lower density around which two clumps of matter rotate, slowly dissipating energy (in our simulations only via GW emission). The density threshold is set looking for the distance at which the logarithmic derivative of the density is

$$\frac{\mathrm{d}\log(\mathrm{D}^*)}{\mathrm{d}\log(\mathrm{r})} = -4.53\,, \tag{3.9}$$

where the numerical value guarantees that disk masses in the two simulations satisfy the x–scaling. In Fig. 3.5(right) the plot shows how the computed disk mass varies when the upper limit in the density integration is changed, and where our estimates lie. The values found are marked as dashed vertical lines. As can be seen from the right panel of Fig. 3.5, they approximately capture the change in slope of the mass profiles. The corresponding disk masses are $M_{\rm disk} \simeq 0.36\,M_\odot$ and $M_{\rm disk} \simeq 0.16\,M_\odot$, respectively. They are about 13% of the initial total mass.

3.3 Conclusions and outlook

In this chapter, a star model was presented composed of self-gravitating superfluid dark matter, showing that its stellar structure depends on just two parameters: the central density and the x parameter given by the ratio of the square root of the coupling to the square boson mass. The observational $\sim 2.1 M_\odot$ constraint on the compact star mass is compatible with these findings only if their radius is larger than ~ 20 km. Large and massive superfluid dark stars may be realized for large value of the x parameter, see Eq. (3.5). Given that superfluid dark stars are not expected to emit light and neutrinos as standard NSs, the only viable way to assess their existence and constraint their masses, radii and tidal deformations is by gravitational observations. In this respect, this study reported a study of superfluid dark-stars merger, showing that for relatively low masses the final object is gravitationally stable. The GW signal is quite different from that of hadronic star mergers and possibly detectable by LVK.

This analysis can be extended and improved in various different ways. One could simulate merging events of two very massive superfluid dark stars, having masses of $20 M_\odot$, or even larger, and then compare the GW signal with that of a black hole merger. For such large masses, the uncertainty in the determination of the tidal deformability in ET [168] should be low enough to allow to distinguish superfluid dark stars from black holes. Hybrid compact stars in which standard hadronic matter coexists with superfluid dark matter may be realized, as well. Such hybrid models have been already discussed in several cases [108–111, 124, 132, 203–210], in particular dark matter in the Bose-Einstein condensed BEC phase has been considered in [109, 132, 205, 209], showing a softening of the EoS as a consequence of the dark matter presence.

The results of the merging simulation show that observables scale with x. However, it is worth remarking that these results were obtained for fixed m_B. Varying the value of the boson mass while keeping x constant should produce a number of effects. The particle velocities are expected to change resulting in the condensate depletion. Rotating superfluids host quantized vortices with core size of the order

$\xi \simeq (\sqrt{2} m_{\rm B} c_s)^{-1}$ [211], while the velocity circulation is quantized in units of $1/m_{\rm B}$. Changing $m_{\rm B}$, the whole vortex structure changes, hence, rotation properties of superfluid dark stars are not scalable with x but explicitly depend on the boson mass. For sufficiently low $m_{\rm B}$, rotating boson stars are expected to host a small number of very large vortices. In this case, the phenomenology can be forecast from cold atom experiments; for instance vortex core precession could take place as observed in ultracold dilute gases [212].

Since in this model it is possible to have light dark matter lumps, heavy superfluid dark stars may result from sequential merging of small droplets. While we assume a zero-temperature superfluid, we must verify that the system remains below the critical temperature even in the worst-case scenario where the virial kinetic energy is fully thermalized [213]. Using the virial relation $k_B T_{\rm vir} \sim GMm_{\rm B}/R = m_{\rm B}\mathcal{C}$, we see that $T_{\rm vir} \propto m_{\rm B}\mathcal{C}$. Conversely, the BEC critical temperature is $T_c \propto n^{2/3}/m_{\rm B}$ (corrections due to interactions are negligible for sufficiently small λ [214, 215]). The condition for the condensate to survive, $T_{\rm vir} \ll T_c$, implies $m_{\rm B}\mathcal{C} \ll n^{2/3}/m_{\rm B}$. This inequality is satisfied for sufficiently small values of the boson mass. Upon substituting the numerical values of the parameters we find an upper bound on the boson mass of hundreds of MeV. During the binary merging, due to the high energies involved, part of matter could evaporate. In principle, if the two colliding objects are sufficiently light, they may evaporate even before the merging is concluded. Hence, arbitrary small dark lumps of condensed bosons are not expected to form unless they are ultracold and survive encounters. In this respect, it would be interesting to study whether viscous effects [216] may influence the thermal and hydrodynamic evolution of merging dark droplets. One should analyse their collisions to infer whether they merge or dissolve. In the latter case they may contribute to the cold dark matter component. Indeed, self-interacting dark matter happens to be a good candidate to alleviate some of dark-matter problems [99, 217], see as well the discussion in [218, 219]. A guidance in the study of dark droplet interactions can derive from studies of colliding ultracold atom droplets [220], which result in either merging or separation depending on their incoming relative velocity.

If the merging droplets of dark bosons are sufficiently compact and cold, they

may create tiny black holes. This would be of great astrophysical interest due to the quick evaporation by Hawking emission, resulting in a mechanism to turn dark matter into Standard Model particles. The present model may be extended to include appropriate self-interactions that drive the system in a supersolid phase [221–224], and rotating supersolid dark stars may be quantum simulated as in [225].

Chapter 4

Rapidly spinning dark matter-admixed neutron stars

This chapter has been published in near-identical form.
Phys. Rev. D **111**, 123005 - **Published 3 June, 2025**
DOI: https://doi.org/10.1103/qcl7-m5kf

Neutron stars (NSs) are among the most extreme astrophysical bodies, serving as invaluable natural laboratories for modern physics. While predicted already in 1934 [226], their first observation was made possible by the radio pulses of the star today known as PSR B1919+21 [17]. In 1982 the first millisecond pulsar, PSR B1937+21, was discovered [227], characterized by a period of around 1.55 ms; the fastest-spinning pulsars currently known are PSR J1748-2446ad, discovered in 2004 [228], with a period of only 1.4 ms (716.36 Hz) and 4U 1820-30 (J1820-30A) with a spin frequency of 716 Hz [229].

Such rapid rotation can be attained as a result of stellar evolution in closely interacting binary systems, whereas the NS not only accretes mass but also gains angular momentum from its nondegenerate companion star due to the conservation of angular momentum. This mechanism is called "recycling" spin-up [230].

The millisecond pulsars have a weak magnetic field, exhibit extremely slow spin-down rates, and can be several billion years old [230–232]. If these long-lived stars reside in regions such as the cores of galaxies or globular clusters, their strong gravitational field could allow them to accrete a significant fraction of dark matter (DM) [233, 234], as described in Section 2.2. All these processes become particularly important in the case of millisecond pulsars. The long lifespans provide sufficient time for interactions with surrounding DM, leading to potentially substantial DM fraction. Over such extended periods, even feeble DM-BM interactions or low local DM densities could result in non-negligible DM accumulation.

Studying rapidly rotating DMANSs is especially interesting in the framework of the X-ray observations by the NICER telescope. Thus, as it was shown in Refs. [209, 235–238] DM could affect the X-ray pulsar pulse profiles, and consequently the mass-radius constraints inferred from the NICER observations.

The properties of nonrotating DMANSs have been thoroughly studied for both isolated and binary configurations [239–243] and the first results have been published for the rotating case [244–247]. In this work, we investigate the impact of rotation on the macroscopic properties of DMANSs. Using an in-house developed extended version of the `RNS` code [41, 42], we investigate scenarios with varying DM fractions, particle masses, and rotation. We analyze both core and halo configurations of DM,

focusing on their influence on the maximum mass and rotational properties of NSs.

In contrast to [244, 245], we do not restrict our analysis to the slowly rotating limit, allowing us to explore configurations up to the mass-shedding limit. This broader approach enables a more comprehensive examination of the parameter space, capturing a wider range of astrophysical scenarios. Moreover, unlike [246], we extend beyond core configurations, encompassing structures from small, compact cores to very large halos. In addition, we systematically explore the maximally rotating, Kepler limit, models.

The paper is organized as follows. Section 4.1 outlines the framework for constructing rotating DMANS models along with the modifications implemented in the `RNS` code. In Sec. 4.2, we analyse representative configurations and discuss their characteristics. Finally, Sec. 4.3 provides a summary of our findings and future perspectives. We use, unless otherwise specified, natural units in which $\hbar = c = G = 1$.

4.1 Numerical framework

Two ideal fluids in hydrostatic equilibrium can be described within a simple model when they uniformly rotate along the same axis and interactions among them are neglected. Writing the total energy-momentum tensor as

$$T^{\mu\nu}_{\rm tot} = T^{\mu\nu}_{\rm BM} + T^{\mu\nu}_{\rm DM}\,, \tag{4.1}$$

that is to say, ignoring energy transfer between the two fluids, the continuity equation $\nabla_\mu T^{\mu\nu}_{\rm tot} = 0$ implies that both $\nabla_\mu T^{\mu\nu}_{\rm BM} = 0$ and $\nabla_\mu T^{\mu\nu}_{\rm DM} = 0$. For nonrotating configurations it is easy to recover a generalized form of the Tolman-Oppenheimer-Volkoff

(TOV) equations [6, 7]:

$$\frac{\mathrm{d}P_{\mathrm{BM}}}{\mathrm{d}r} = -\frac{(\varepsilon_{\mathrm{BM}} + P_{\mathrm{BM}})(m_{\mathrm{tot}} + 4\pi r^3 P_{\mathrm{tot}})}{r^2(1 - \frac{2m_{\mathrm{tot}}}{r})}\,, \tag{4.2a}$$

$$\frac{\mathrm{d}P_{\mathrm{DM}}}{\mathrm{d}r} = -\frac{(\varepsilon_{\mathrm{DM}} + P_{\mathrm{DM}})(m_{\mathrm{tot}} + 4\pi r^3 P_{\mathrm{tot}})}{r^2(1 - \frac{2m_{\mathrm{tot}}}{r})}\,, \tag{4.2b}$$

$$\frac{\mathrm{d}m_{\mathrm{BM}}}{\mathrm{d}r} = 4\pi r^2 \varepsilon_{\mathrm{BM}}\,, \tag{4.2c}$$

$$\frac{\mathrm{d}m_{\mathrm{DM}}}{\mathrm{d}r} = 4\pi r^2 \varepsilon_{\mathrm{DM}}\,, \tag{4.2d}$$

where $m_{\mathrm{tot}}(r) = m_{\mathrm{BM}}(r) + m_{\mathrm{DM}}(r)$ and similarly $P_{\mathrm{tot}}(r) = P_{\mathrm{BM}}(r) + P_{\mathrm{DM}}(r)$.

Masses of DM and BM star components can be also defined as an integral over the entire stellar volume of $\sqrt{-g}(-2T^0_0 + T^\mu_\mu)$, which can be computed for each fluid as

$$M_{\mathrm{X}} = 4\pi \int_0^\infty \mathrm{d}r\, r^2 \int_0^{\pi/2} \mathrm{d}\theta \sin\theta\; \mathrm{e}^{2\alpha+\gamma}\,(\varepsilon_{\mathrm{X}} + 3P_{\mathrm{X}})\,, \tag{4.3}$$

where we indicate with the subscript X either the BM or the DM and the metric fields α and γ are defined below in Eq. (4.5). The total mass of the system is defined as $M_{\mathrm{tot}} = M_{\mathrm{BM}} + M_{\mathrm{DM}}$.

In general, it is true that the total mass, obtained either from Eqs. (4.2c) and (4.2d) or through Eq. (4.3), is equivalent since this is an invariant quantity for the system. However, this is not valid for the single components (i.e., $m_{\mathrm{X}}(r \to \infty) \neq M_{\mathrm{X}}$).

These equations can be solved simultaneously by employing the standard Runge-Kutta method. Initial conditions are specified at $r = 0$ imposing zero mass and central pressures interpolated from the respective EOS for a given central energy density. The metric fields can finally be reconstructed from the matter fields and complete the construction of a spherically symmetric spacetime.

The radii of each of the components are found using the zero-pressure condition at the surface. At the same time, the BM and DM distributions defined by the central energy density or chemical potential values scale proportionally. As was

shown in [206] the values of the chemical potentials of BM and DM are related as

$$\frac{\mathrm{d}\ln\mu_{\rm BM}}{\mathrm{d}r} = \frac{\mathrm{d}\ln\mu_{\rm DM}}{\mathrm{d}r} = -\frac{M_{\rm tot}+4\pi r^3 P_{\rm tot}}{r^2(1-\frac{2M_{\rm tot}}{r})}. \tag{4.4}$$

To consider rotating configurations, the Einstein field equations can be solved in axial symmetry by employing the Komatsu-Eriguchi-Hachisu (KEH) scheme [40], incorporating the modifications proposed in [43]. In particular we have modified the `RNS`[1] code [41, 42], straightforwardly generalizing the original algorithm as follows.

The general line element is expressed in quasi-isotropic coordinates as

$$\begin{aligned}\mathrm{d}s^2 = &-\mathrm{e}^{\gamma+\rho}\mathrm{d}t^2 + \mathrm{e}^{2\alpha}(\mathrm{d}r^2 + r^2\mathrm{d}\theta^2)\\ &+ \mathrm{e}^{\gamma-\rho}r^2\sin^2\theta(\mathrm{d}\phi-\omega\mathrm{d}t)^2\,,\end{aligned} \tag{4.5}$$

where γ, ρ, α, and ω represent the metric potentials, each depending on r and θ. The circumferential radius is recovered from r as

$$R = r\,\mathrm{e}^{\frac{\gamma-\rho}{2}}\,. \tag{4.6}$$

Each fluid's four-velocity $u^\mu_{\rm X}$ is defined as

$$u^\mu_{\rm X} = \frac{\mathrm{e}^{-(\gamma+\rho)/2}}{\sqrt{1-v_{\rm X}^2}}\,(1,0,0,\Omega_{\rm X})\,, \tag{4.7}$$

where $v_{\rm X} = (\Omega_{\rm X}-\omega)r\sin\theta\,\mathrm{e}^{-\rho}$ and $\Omega_{\rm X}$ is the fluid angular velocity. The sign of $\Omega_{\rm X}$ determines if the fluid rotates counterclockwise or clockwise. For most of our studies we will assume that both fluids rotate in a counterclockwise rotation ($\Omega_{\rm X} > 0$); in Sec. 4.2.2 we will explore the other interesting case in which the DM fluid counterrotates with respect to the BM ($\Omega_{\rm DM} < 0$).

Equation (4.7) implies that even if one of the two components has zero angular velocity $\Omega_{\rm X}$, the linear velocity $v_{\rm X}$ remains nonzero as a result of the frame-dragging effect induced by the other component.

[1] github.com/cgca/rns

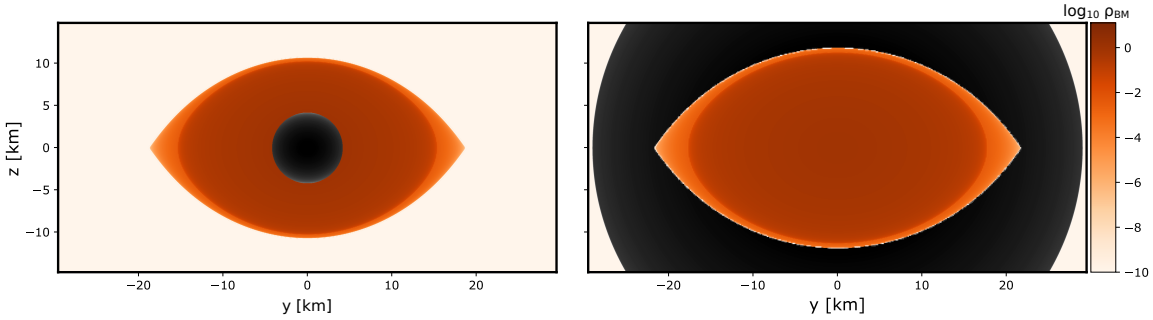

Figure 4.1: Density profiles in the $y-z$ plane at $x=0$ for a NS rotating at $\Omega_{\rm K}^{\rm BM}$, $\Omega_{\rm DM}=0$ and $f_{\rm DM}=5\%$. The black shaded regions indicate the dark matter density field. **Left**: core configuration, $M_{\rm tot}=2\,{\rm M}_\odot$, $m_{\rm DM}=1\,{\rm GeV}$, $\Omega_{\rm K}^{\rm BM}=8068\,{\rm Hz}$. **Right**: halo configuration, $M_{\rm tot}=2.08\,{\rm M}_\odot$, $m_{\rm DM}=250\,{\rm MeV}$, $\Omega_{\rm K}^{\rm BM}=6841\,{\rm Hz}$.

The four-velocity $u_{\rm X}^\mu$ enters in the energy-momentum tensor as

$$T_{\rm X}^{\mu\nu}=(\varepsilon_{\rm X}+P_{\rm X})u_{\rm X}^\mu u_{\rm X}^\nu+P_{\rm X}g^{\mu\nu}\,, \tag{4.8}$$

where $g^{\mu\nu}$ is the inverse metric tensor.

Studying the nonvanishing Einstein field equations, it is possible to show that the structure of the equations to be solved is analogous to the one-fluid case reported in [40]. The explicit form of these equations is reported in Appendix A.

The computation of the metric fields, alongside the matter distribution, begins with an initial guess, typically a previous iteration or a nonrotating star. From the initial metric fields, a value of the angular velocity is determined through the first integral of the hydrostationary equilibrium

$$h_{\rm X}-\ln u_{\rm X}^t={\rm const}\,, \tag{4.9}$$

where $h_{\rm X}$ is the specific enthalpy. By coupling Eq. (4.9) with a prescribed ratio $r_{\rm ratio}^{\rm X}$ between the polar radius ($r_p^{\rm X}$) and equatorial radius ($r_e^{\rm X}$) for each fluid, it is possible to compute

$$\Omega_{\rm X} = \omega_e^{\rm X} \pm \sqrt{1 - \mathrm{e}^{\frac{\gamma_p^{\rm X} + \rho_p^{\rm X} - \gamma_e^{\rm X} - \rho_e^{\rm X}}{2}}} \frac{\mathrm{e}^{\rho_e^{\rm X}}}{r_e^{\rm X}} \tag{4.10}$$

and thus $v_{\rm X}$. The metric fields are evaluated at either the equatorial radius of the respective fluid (subscript e) or the polar radius (subscript p)–e.g.

$$\gamma_e^{\rm BM} = \gamma\left(r = r_e^{\rm BM},\, \theta = \pi/2\right) , \tag{4.11}$$

$$\gamma_p^{\rm BM} = \gamma\left(r = r_p^{\rm BM},\, \theta = 0\right) . \tag{4.12}$$

Note that when $\Omega_{\rm X} < 0$ the square root in Eq. (4.10) acquires the negative sign.

The specific enthalpy distribution is computed using

$$h_{\rm X} = \frac{1}{2}\left[\gamma_p^{\rm X} + \rho_p^{\rm X} - \gamma - \rho - \ln(1 - v_{\rm X}^2)\right] . \tag{4.13}$$

The matter distributions, i.e. the energy densities $\varepsilon_{\rm X}$ and pressures $P_{\rm X}$, are computed from Eq. (4.13) starting from a fixed value of the central energy density $\varepsilon_c^{\rm X}$. The metric potentials are then recalculated, and this iterative process is repeated until convergence is achieved.

Of particular importance for our studies is the choice of a definition for the DM fraction

$$f_{\rm DM} = \frac{M_{\rm DM}}{M_{\rm tot}} . \tag{4.14}$$

It is well known [248] that in general relativity there is no unique definition of an object's mass. In the previous paragraph, we discussed the different mass definitions of the nonrotating case. While Eq. (4.3) can be readily generalized to rotating stars, there is no straightforward rotating version of Eqs. (4.2c) and (4.2d). Thus, for rotating stars, we define the DM and BM masses as

$$\begin{aligned} M_{\rm X} = 4\pi \int_0^\infty \mathrm{d}r\, r^2 \int_0^{\pi/2} \mathrm{d}\theta \sin\theta\ \mathrm{e}^{2\alpha+\gamma} \times \\ \left[\frac{\varepsilon_{\rm X} + P_{\rm X}}{1 - v_{\rm X}^2}\left(1 + v_{\rm X}^2 + 2\omega r v_{\rm X}\, \mathrm{e}^{-\rho}\sin\theta\right) + 2P_{\rm X}\right] , \end{aligned} \tag{4.15}$$

and of course, the total mass is the sum of the two.

The rest mass of each component $M_{\rm X}^0$ can also be calculated using an integral throughout the star

$$M_{\rm X}^0 = 4\pi \int_0^\infty {\rm d}r \int_0^{\pi/2} {\rm d}\theta \sqrt{-g} W \rho_{\rm X}^0 \,, \tag{4.16}$$

where $W = 1/\sqrt{1-v_{\rm X}^2}$ denotes the Lorentz factor of the fluid element, and $\rho_{\rm X}^0 = (\varepsilon_{\rm X} + P_{\rm X})\ {\rm e}^{-h_{\rm X}}$ represents the rest mass density. Naturally, the total rest mass of the star is the sum of the two components.

Another important parameter of the rotating stars is the Keplerian angular velocity $\Omega_{\rm K}$. It represents the angular velocity of a particle on a circular orbit around the star's equator at zero altitude and is the maximum angular velocity allowed for stable configurations. For the metric element given in Eq. (4.5) it can be expressed as

$$\Omega_{\rm K}^{\rm X} = \omega_e^{\rm X} + \frac{v_e^{\rm X}}{r_e^{\rm X}}\, {\rm e}^{\rho_e^{\rm X}} \,, \tag{4.17}$$

where $v_e^{\rm X}$ is the equatorial orbital velocity measured by an observer with zero angular momentum in the ϕ-direction. $\Omega_{\rm K}^{\rm X}$, in general, depends parametrically on both the central energy density of the fluid X and its angular velocity $\Omega_{\rm X}$. Note that Eq. (4.17) can be used to compute the Keplerian angular velocity regardless of the configuration we choose for the DM since the velocity of a particle in circular orbit on the equator depends only on the metric fields:

$$\begin{aligned} v_e(r) = {} & \frac{e^{-\rho} r^2 \partial_r \omega}{2 + r\left(\partial_r \gamma - \partial_r \rho\right)} \pm \\ & \sqrt{\frac{r\left(\partial_r \gamma + \partial_r \rho\right)}{2 + r\left(\partial_r \gamma - \partial_r \rho\right)} + \frac{e^{-2\rho} r^4 (\partial_r \omega)^2}{\left[2 + r\left(\partial_r \gamma - \partial_r \rho\right)\right]^2}} \,. \end{aligned} \tag{4.18}$$

As before, the minus sign is acquired when the fluid X is counterrotating.

Another important quantity to study for rotating NSs is their moment of inertia, defined as

$$I_{\rm X} = \frac{J_{\rm BM} + J_{\rm DM}}{\Omega_{\rm X}} \,, \tag{4.19}$$

where the angular momentum $J_{\rm X}$ is computed from

$$\begin{aligned} J_{\rm X} &= \int \mathrm{d}^3x\,\sqrt{-g}\,T_{\rm X}{}^0{}_\phi \\ &= 4\pi \int_0^\infty \mathrm{d}r\, r^3 \int_0^{\pi/2} \mathrm{d}\theta \sin^2\theta\, \mathrm{e}^{2\alpha+\gamma-\rho}\,(\varepsilon_{\rm X}+P_{\rm X})\,\frac{v_{\rm X}}{1-v_{\rm X}^2}\,. \end{aligned} \tag{4.20}$$

In the two-fluid system the moment of inertia could be defined for each of the components separately, or the total one [245, 249]. Since this quantity measures the object's resistance to changes in rotational frequency and depends on the mass distribution of both components, it serves as a potential probe of DM, which will be discussed in the following section.

Interestingly, the core configurations of DM are impressively similar to superfluid NSs where the two fluids correspond to the normal and superfluid components [250, 251]. This similarity could bring new insights to the DM topic.

4.2 Results

In this section, we present the results of our analysis of rotating DMANSs at the mass-shedding limit. Unless otherwise specified, we employ the DD2npY-T equation of state to describe the baryonic component. Hereafter, as the most representative case, we employ two distinct DM configurations: a DM core obtained for the particle mass $m_{\rm DM} = 1\,\mathrm{GeV}$ and a halo for $m_{\rm DM} = 250\,\mathrm{MeV}$. Note that the self-interaction strength value in both cases is fixed to $\lambda = 24\pi$. This choice is arbitrary and made in order to obtain in the nonrotating core limit a maximum mass close to $2\,\mathrm{M}_\odot$.

4.2.1 Nonrotating dark matter

Figure 4.1 shows a slice of the density profiles for both BM and DM on the $x = 0$ plane for two representative configurations: a core (left panel) and a halo (right panel). These models correspond to systems with a total gravitational mass of $2\,\mathrm{M}_\odot$ (left) and $2.08\,\mathrm{M}_\odot$ (right), and a DM fraction of $f_{\rm DM} = 5\%$, $\Omega_{\rm DM} = 2\,\mathrm{Hz}$, and

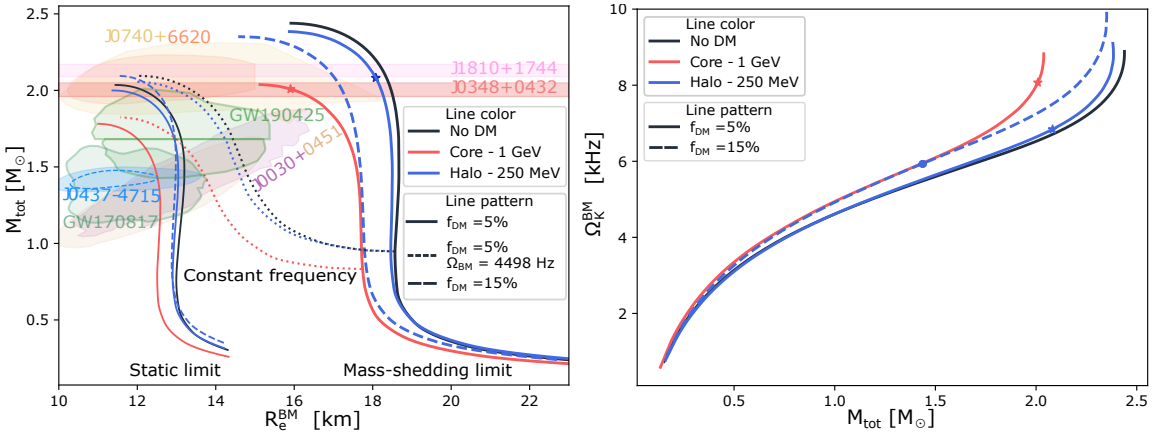

Figure 4.2: Sequences of configurations with nonrotating DM $\Omega_{\rm DM} = 0$ and two fixed DM fractions $f_{\rm DM} = 5\%$ (solid lines) and $f_{\rm DM} = 15\%$ (dashed lines). With red (blue) we indicate the curve that characterizes a core (halo) case with particles of 1 GeV (250 MeV). The two star symbols represent the models reported in Fig. 4.1. **Left:** The total NS mass as a function of its equatorial radius. Thin lines represent nonrotating BM as a reference. Dotted lines show the sequences rotating at constant angular frequency $\nu_{\rm BM} = 716$ Hz (or equivalently an angular velocity $\Omega_{\rm BM} = 4498$ Hz). The pink and light red bands represent the 1σ constraints on the mass of PSR J1810+1744 [22], and PSR J0348+0432 [21]. The NICER measurement of PSR J0030+0451 [18, 19] is shown with the purple and yellow contours, the gold and orange contours represent the PSR J0740+6620 measurement [24, 25], while light blue (95% CL) and light blue dashed (68% CL) contours represent the PSR J0437-4715 measurement [26]. LIGO-Virgo detections of GW170817 [2] and GW190425 [30] binary NS mergers are shown in light green. **Right**: Mass dependence of the Keplerian angular velocity for DMANS with nonrotating DM (thick lines on the left panel).

$\Omega_{\rm BM} = \Omega_K^{\rm BM}$. Both panels highlight the characteristic cusp that develops at the BM mass-shedding limit because of the very rapid increase of the equatorial radius $R_{\rm BM}$ when increasing $\Omega_{\rm BM}$ [252]. We can notice how the deformation due to DM, at least for this particular choice of parameters, is very weak. This is a reflection of the fact that the DM and BM components interact only gravitationally.

A first analysis of the impact of nonrotating DM on spinning NSs can be carried looking at the left panel of Fig. 4.2. Here we report the relation between the total

mass given by Eq. (4.15) and the equatorial radius $R_e^{\rm BM}$ for static DMANSs (thin lines) and maximally rotating stars (thick lines). Thin dotted lines between the two depict sequences with fixed rotational rate, namely $f = 716$Hz, corresponding to the fastest spinning pulsar as discussed above. Naturally, for low masses, it ends at the Kepler limit sequences. The colors distinguish the different DM configurations: Red shows a core configuration, blue is a halo, and finally black is the standard case of no DM. All allowed uniformly rotating stars with $f_{\rm DM} = 5\%$ (solid lines) lie in the region bounded by these curves. Finally, the dashed blue lines show another realization of the halo configuration for $f_{\rm DM} = 15\%$. Note that such a high DM fraction was chosen to illustrate the effect at its extreme.

Rotation generally tends to increase the maximum mass by approximately 20% and the radius by about 40% for pure BM NSs [252]. In the case of a DM core, in the static limit the additional mass present with respect to the $f_{\rm DM} = 0$ case mimics a softening of the nucleonic EOS. The effect is a reduction of the maximum mass and radius. Rotation of the BM at the Kepler frequency has the same effect as before, increasing the maximum mass and radius by approximately 15% and 40% respectively. The case of a DM halo exhibits a more peculiar behavior. In the static limit for $f_{\rm DM} = 5\%$, we do not observe the expected increase in mass and radius, as predicted by previous studies [110, 111, 253]. This deviation arises from the specific choice of parameters $f_{\rm DM}$, $m_{\rm DM}$, and λ. Thus, lighter DM particles of $m_{\rm DM} \sim 100\,$MeV would form a more extended and dilute halo [109]. Notably, if we keep $m_{\rm DM}$ and λ fixed while increasing the DM fraction beyond 10%, the expected growth in mass and radius emerges, as illustrated by the dashed blue line for $f_{\rm DM} = 15\%$. When BM rotates at its Kepler angular velocity, the maximum mass and radius for $f_{\rm DM} = 5\%$ increase by approximately 20% and 40%, respectively.

The DM component, currently assumed to be nonrotating, is only marginally affected by the rotation of the NS, except in the most massive systems. In both core and halo configurations, low-mass systems are associated with a small Keplerian angular velocity $\Omega_{\rm K}^{\rm BM}$ and a weak frame-dragging potential ω. This results in a minimal deformation of the DM distribution: The equatorial radius $R_e^{\rm DM}$ exceeds the polar radius $R_p^{\rm DM}$ by less than 0.1%. Near the last stable configuration this

deformation increases but remains modest, with a maximum difference of approximately 2%. In contrast, the BM exhibits significantly larger deformations, with the equatorial radius exceeding the polar radius by about 50% even for low-mass systems. This percentage gradually increases as the system approaches the last stable configuration.

Higher DM fractions partially change this consideration, e.g. the blue dashed line in Fig. 4.2 for a halo configuration with $f_{\rm DM} = 15\%$. While the deformation from spherical symmetry remains small, the change in $R_e^{\rm DM}$ that is found with the current setup is much bigger, leading to the formation of a mixed sequence where at low masses the DM forms a halo. In contrast, at high masses, it is characterized by $R_e^{\rm BM} > R_e^{\rm DM}$ but $R_p^{\rm BM} < R_p^{\rm DM}$. This is what happens for the dashed line on the upper panel of Fig. 4.2; the switch happens at a mass of $1.44\,{\rm M}_\odot$. The blue dot highlights the specific configuration marking this transition.

The right panel of Fig. 4.2 shows a comparison between the Kepler frequencies across the three configurations for varying total gravitational masses. Core configurations consistently exhibit higher rotational frequencies compared to both the halo and $f_{\rm DM} = 0$ cases. The stronger gravitational pull at the equator requires an increased centrifugal force to reach the mass-shedding limit, and hence a higher angular frequency. Halos show instead much smaller deviations from the pure BM case: Only for masses above $1.5\,{\rm M}_\odot$ there is an appreciable difference between the two. Increasing the DM fraction in this last case has the expected behavior of increasing the maximum angular velocity while maintaining the same qualitative trajectory. A higher DM fraction at the fixed total mass implies a higher DM mass, thus a lower radius and a higher angular velocity.

Figure 4.3 show the two key aspects of the maximally rotating sequences, presenting the oblateness, defined as

$$e = \sqrt{1 - \left(\frac{R_p^{\rm BM}}{R_e^{\rm BM}}\right)^2}\,. \tag{4.21}$$

It is important to clarify that the quantity e defined above represents the geometric

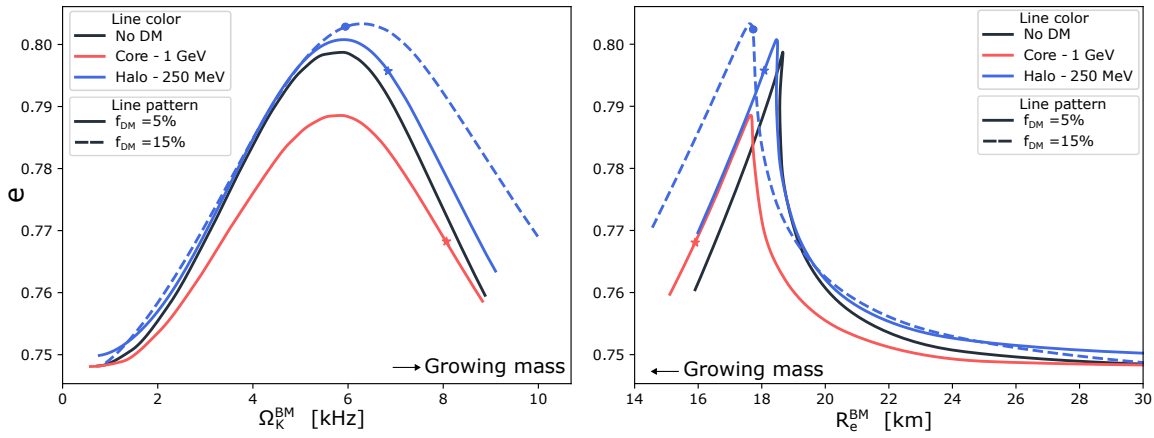

Figure 4.3: Both panels show the stable configurations of maximally rotating (Kepler) sequences with varying central energy density e_c^{BM}. **Left:** Oblateness as a function of the angular velocity $\Omega_{\mathrm{BM}} = \Omega_{\mathrm{K}}^{\mathrm{BM}}$. **Right**: Oblateness as a function of the BM equatorial radius R_e^{BM}.

oblateness of the stellar surface. However, this is not necessarily the quantity relevant for gravitational interactions. The gravitationally relevant oblateness is instead determined by the multipole moments of the spacetime, specifically the quadrupole moment, which encodes the deformation of the mass distribution and the moment of inertia.

While for the fluid models considered here the geometric and gravitational deformations are expected to be correlated, this is not always the case. For instance, relativistic stars with strong toroidal magnetic fields can exhibit a "prolate-oblate" behaviour, where the magnetic tension induces a prolate mass distribution (negative quadrupole moment) even while rotation keeps the surface oblate (positive surface oblateness) [254]. In this work, we restrict our analysis to non-magnetized fluids, focusing on the geometric deformation as a proxy for the stellar shape.

The left panel of Fig. 4.3 shows the surface oblateness e as a function of the angular velocity $\Omega_{\mathrm{BM}} = \Omega_{\mathrm{K}}^{\mathrm{BM}}$. e as a function of the angular velocity $\Omega_{\mathrm{BM}} = \Omega_{\mathrm{K}}^{\mathrm{BM}}$. All four profiles show similar behaviour. Low-mass stars rotating at angular velocities on the order of hundreds of Hz exhibit only a slight increase in oblateness with growing angular velocity Ω_{BM}–and hence with the total mass. As Ω_{BM} increases,

the oblateness reaches a maximum value. The angular velocity at which this peak occurs is consistent among all configurations: They closely follow the $f_{\rm DM} = 0$ reference at $\Omega_{\rm BM} \approx 6\,{\rm kHz}$. Then the oblateness tends to decrease until the last stable configuration is reached.

The right panel of Fig. 4.3 illustrates a comparison of oblateness against the baryonic equatorial radius of the maximally rotating configurations. At high radii–i.e., low masses and low angular velocities–the configurations show a similar trend toward slowly changing values of the oblateness. It is intriguing to observe that as the systems approach lower radii, halos, and cores become degenerate while decreasing linearly with the radius. They exhibit the same deformation, despite having drastically different masses, angular velocities, and DM configurations. Specifically, as the difference between the configurations becomes very small, the DM halo has a radius several kilometers larger than the NS, while the DM core is always such that $R_e^{\rm BM} \approx 3R_e^{\rm DM}$. Changing the DM fraction shifts the location of this linear regime to lower radii while keeping the slope approximately the same. Note that when the oblateness reaches its maximum the system is already in the mixed configuration characterized by $R_e^{\rm BM} > R_e^{\rm DM}$ but $R_p^{\rm DM} > R_p^{\rm BM}$.

Finally, Fig. 4.4 presents the moment of inertia of BM, $I_{\rm BM}$, as defined in Eq. (4.19), for the different NSs configurations as a function of the total gravitational mass. Solid lines represent maximally rotating stars with the DM fraction of 5%, dotted lines represent the sequences of stars at a constant angular frequency of $\nu_{\rm BM} = \Omega_{\rm BM}/2\pi = 716\,{\rm Hz}$, and the dashed line corresponds to the maximally rotating halo sequence for the 15% DM fraction. For low-mass stars, the moment of inertia changes at the same rate regardless of the configuration considered. Core configurations tend to significantly decrease, together with the maximum mass, the maximum moment of inertia allowed for stable configurations. Halos similar to before follow closely the pure BM case, only slightly decreasing the values of $I_{\rm BM}$ allowed for stable configurations. Increasing the DM content from $f_{\rm DM} = 5\%$ to $f_{\rm DM} = 15\%$ results in a deviation from the BM case for a given mass, effectively decreasing the maximum $I_{\rm BM}$ allowed.

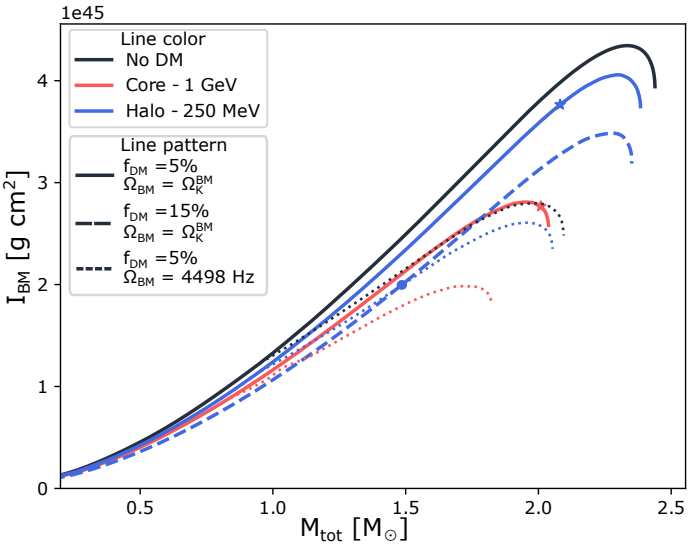

Figure 4.4: Moment of inertia for various configurations of DMANSs as a function of the total mass. Here $J_{\rm DM} = 0$. Dotted lines illustrate the sequences rotating at constant angular velocity $\Omega_{\rm BM} = 4498\,{\rm Hz}$ (or equivalently an angular frequency of $\nu_{\rm BM} = 716\,{\rm Hz}$), while the rest of the lines correspond to maximally rotating configurations.

4.2.2 Rotating dark matter

In the previous subsection, we considered DMANSs configurations with a rotating BM component and a nonrotating DM component. This approach allowed us to establish a baseline for understanding how DM impacts the structure of NSs without contributing directly to the rotational dynamics. Here, we lift the assumption of nonrotating DM, enabling both components to rotate independently.

Figure 4.5 reproduces Fig. 4.2 with the same colour scheme and line styles as in the previous subsection; dash-dotted lines represent the configurations characterized by $f_{\rm DM} = 5\%$, $\Omega_{\rm BM} = \Omega_{\rm K}^{\rm BM}$ and $\Omega_{\rm DM} = \Omega_K^{\rm DM}$. This is practically the fastest rotation of the DM component that can be imposed and is thus useful to see the maximum difference with the $\Omega_{\rm DM} = 0$ regime.

First, it is important to highlight that the blue dash-dotted line in Fig. 4.5 does not represent a halo of DM surrounding an NS anymore. It is instead a very large core with $R_e^{\rm DM} \approx R_e^{\rm BM}$. The low-mass halo of DM expands, due to rotation, less

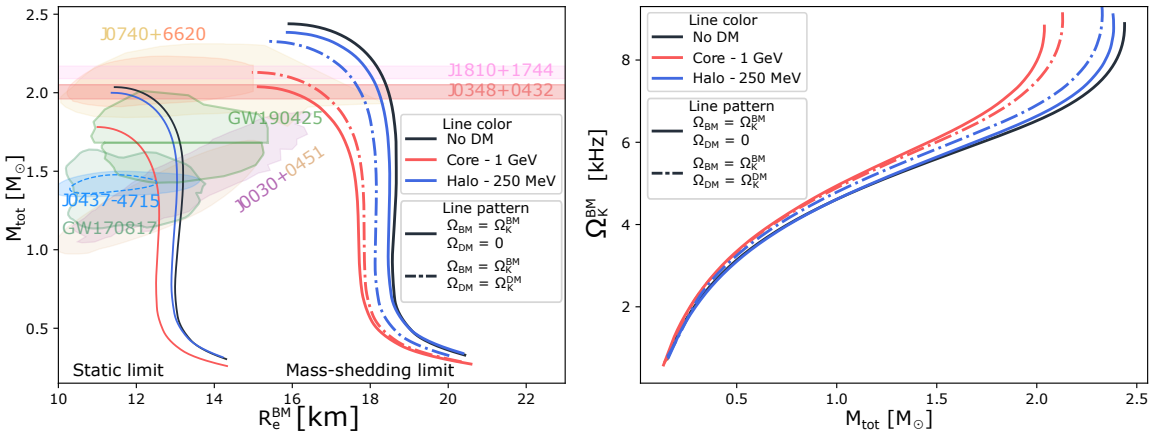

Figure 4.5: Left: Comparison between the M-R curves of a maximally rotating NS with nonrotating DM (solid lines) and DM corotating at its Keplerian angular velocity (dash-dotted lines), $\Omega_{\rm DM} = \Omega_{\rm K}^{\rm DM}$. **Right:** Same comparison for the NS's maximum angular velocity as a function of the total gravitational mass.

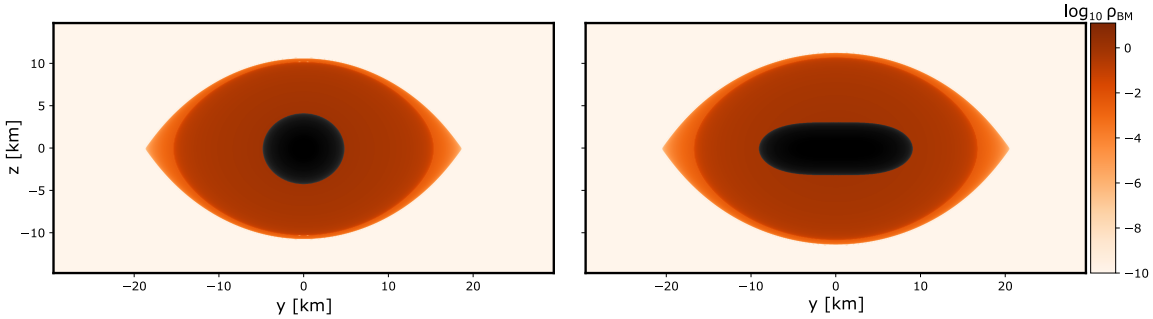

Figure 4.6: Density profiles in the yz plane at $x = 0$ for a NS rotating at $\Omega_{\rm K}^{\rm BM}$, $M_{\rm tot} = 2\,{\rm M}_\odot$, $m_{\rm DM} = 1\,{\rm GeV}$ and $f_{\rm DM} = 5\%$. The black shaded regions indicate the dark matter density field. **Left:** core configuration, $\Omega_{\rm K}^{\rm BM} = 8076\,{\rm Hz}$ and two fluids corotating with the same angular velocity $\Omega_{\rm DM} = \Omega_{\rm K}^{\rm BM}$. **Right:** core configuration $\Omega_{\rm K}^{\rm BM} = 7279\,{\rm Hz}$ and two fluids counterrotating with the same angular velocity $\Omega_{\rm DM} = -\Omega_{\rm K}^{\rm BM}$.

than the BM does, ultimately becoming engulfed by the NS. For convenience, we will refer to it as "halo" nonetheless, to underline the value of the DM particle.

The core configurations increase the maximum mass of the sequence by about 4.5% while the halo configurations reduce it by about 2.5%, going from the thick

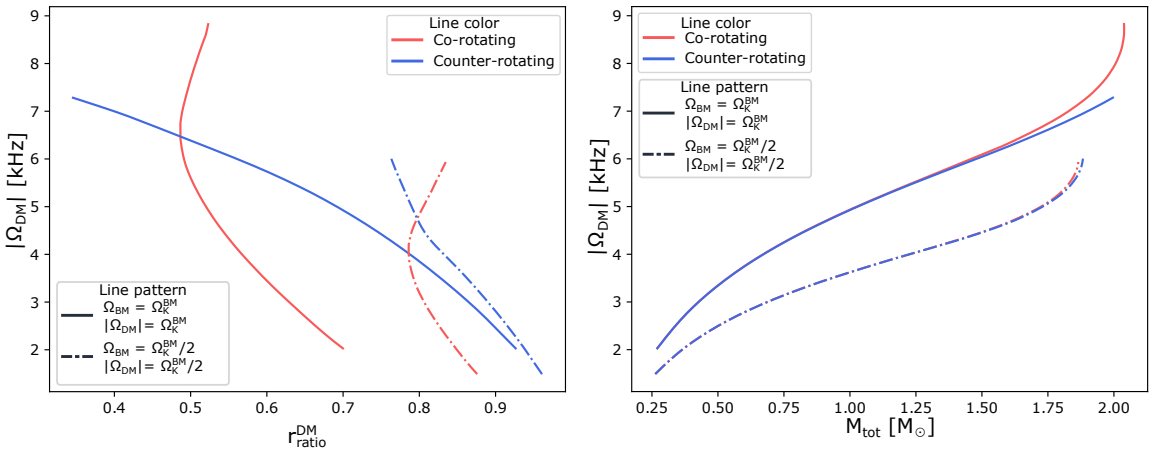

Figure 4.7: Comparison between corotating (red) and counterrotating (blue) core configurations for $m_{\rm DM} = 1\,\text{GeV}$, $f_{\rm DM} = 5\%$ and $\Omega_{\rm BM} = |\Omega_{\rm DM}| = \Omega_{\rm K}^{\rm BM}$ (solid line) or $\Omega_{\rm BM} = |\Omega_{\rm DM}| = \Omega_{\rm K}^{\rm BM}/2$ (dash-dotted line). **Left:** Relation between the angular velocity $|\Omega_{\rm DM}|$ and the ratio of polar to equatorial radius $r_{\rm ratio}^{\rm DM}$ of the corresponding configuration. **Right**: Relation between the angular velocity $|\Omega_{\rm DM}|$ and the total mass of the system.

solid lines to the dash-dotted ones. Comparing–where possible– the equal mass configurations, we notice that rotating cores tend to increase the equatorial radius of the NS while rotating halos tend to significantly decrease it. The Kepler frequency reflects this change: At a constant mass, it decreases for cores and increases for halos.

Lastly, Fig. 4.6 compares two core configurations with $M_{\rm tot} = 2\,\text{M}_\odot$, $f_{\rm DM} = 5\%$, and $|\Omega_{\rm DM}| = \Omega_{\rm BM} = \Omega_{\rm K}^{\rm BM}$. In the left panel, both fluids corotate with the same angular velocity ($\Omega_{\rm DM} = \Omega_{\rm K}^{\rm BM} > 0$), representing a system that has synchronized over time and reached dynamic equilibrium. In this case, the deformation of the DM component remains moderate, with the mass-radius relation showing only minor deviations from the corresponding nonrotating case.

In the right panel of Fig. 4.6, the two fluids are instead counterrotating with $\Omega_{\rm DM} = -\left|\Omega_{\rm K}^{\rm BM}\right|$. A notable difference in this configuration is the deformation of the DM component. While in the corotating case, the ratio of polar to equatorial radius is approximately $r_{\rm ratio}^{\rm DM} \approx 0.51$, in the counterrotating case it decreases significantly to $r_{\rm ratio}^{\rm DM} \approx 0.34$.

The interplay between the metric fields in Eq. (4.5), the fluid angular velocity Eq. (4.10) and the Kepler angular velocity Eq. (4.17) is complex. Significant insight is given by Fig. 4.7: in the left panel we report the relation between the absolute value of the DM angular velocity for corotating (red) and counterrotating (blue) core configurations; the right panel shows instead the dependence of $\Omega_{\rm DM}$ on the total gravitational mass. We use solid lines for $\Omega_{\rm BM} = |\Omega_{\rm DM}| = \Omega_{\rm K}^{\rm BM}$ and dash-dotted lines for $\Omega_{\rm BM} = |\Omega_{\rm DM}| = \Omega_{\rm K}^{\rm BM}/2$.

For both values of the angular velocity, low-mass systems behave as expected: Increasing the required angular velocity (i.e., decreasing the input parameter $r_{\rm ratio}^{\rm BM}$) the deformation of the DM fluid has to increase (i.e., $r_{\rm ratio}^{\rm DM}$ has to decrease). However, the corotating sequence (red solid line) exhibits a counter-intuitive feature where the curve bends backward: the system reaches higher coordinate angular velocities $|\Omega_{\rm DM}|$ while becoming *less* deformed (increasing $r_{\rm ratio}^{\rm DM}$).

This behaviour is a direct consequence of the strong increase in the frame-dragging angular velocity ω for compact, corotating configurations. To achieve a required coordinate angular velocity $\Omega_{\rm DM}$, the fluid relies partially on being "dragged" by the rotating spacetime. As ω becomes large, the fluid requires less intrinsic rotation relative to the local inertial frame (i.e., a smaller relative velocity $\Omega_{\rm DM} - \omega$) to reach the same global $\Omega_{\rm DM}$. Since the physical centrifugal deformation is driven by this relative rotation rather than the coordinate velocity, the DM halo becomes more spherical even as its coordinate angular velocity increases.

The opposite situation occurs for counterrotating configurations. Here, the fluid must rotate against the frame dragging to achieve the required $\Omega_{\rm DM}$, meaning the relative rotation—and thus the centrifugal deformation—must increase monotonically.

In Fig. 4.7 the line for the counterrotating configuration ends before it reaches its last stable configuration. This is most probably a numerical issue related to the difficulty of obtaining solutions having extreme deformation with the `RNS` code.

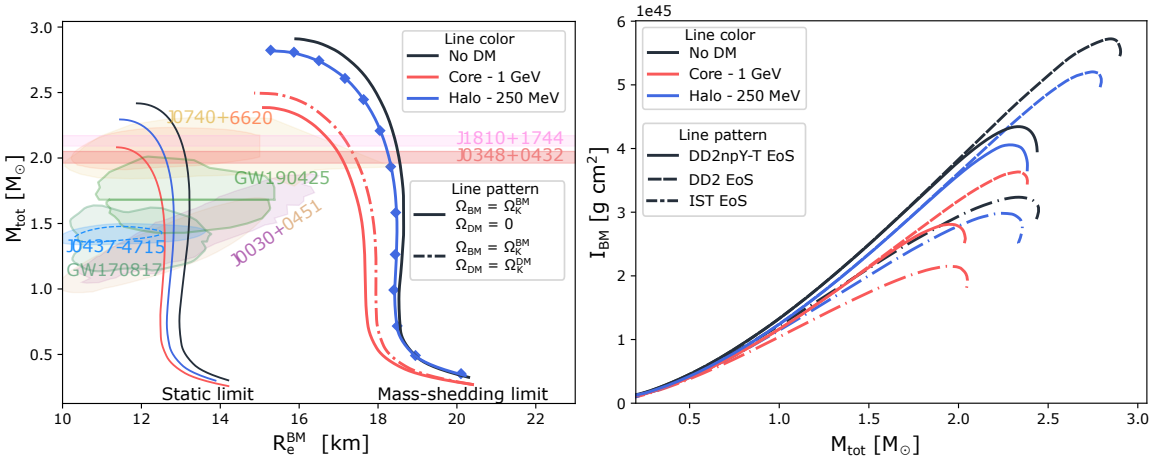

Figure 4.8: Left: M-R diagram for the DD2 EOS. Thin lines represent static configurations for reference, while thick solid lines represent maximally rotating NSs with nonrotating DM. Dash-dotted lines represent sequences with $\Omega_{\rm BM} = \Omega_{\rm K}^{\rm BM}$ and $\Omega_{\rm DM} = \Omega_{\rm K}^{\rm DM}$. With red (blue) we indicate the curves that characterize the core (halo) configuration with particle mass of 1 GeV (250 MeV) at constant DM fraction $f_{\rm DM} = 5\%$. Since halo configurations with a nonrotating DM and DM rotating at its Kepler limit cannot be visually distinguished, we plot the latter with diamonds appearing on top. **Right**: Comparison of the moment of inertia computed for three EOSs for $\Omega_{\rm BM} = \Omega_{\rm K}^{\rm BM}$ and $\Omega_{\rm DM} = 0$ at $f_{\rm DM} = 5\%$.

4.2.3 Effect of the variation of the BM EOS

As the performed analysis incorporates two underlying EOSs, for BM and DM, their choice would introduce some uncertainties, while qualitatively the conclusions will remain the same. To address the uncertainties of the dense BM EOS we now turn our attention to the DD2 EOS introduced in Sec. 1.2. The left panel of Fig. 4.8 presents the M-R diagram, where the thin solid lines denote static configurations, thick solid lines correspond to maximally rotating BM with nonrotating DM, and dash-dotted lines represent both fluids at their respective maximum angular velocities. Colors once again distinguish between core and halo configurations.

In the absence of DM, the DD2 EOS, in comparison to the DD2npY-T EOS, allows a significantly higher maximum mass, around 2.41 $M_\odot$. As a result, even static core configurations with $f_{\rm DM} = 5\%$ can satisfy the observational data on

heavy pulsars: PSR J0348+0432 $M = (2.01 \pm 0.04)\,\mathrm{M}_\odot$ [21] and barely fall below the $M = (2.13 \pm 0.04)\,\mathrm{M}_\odot$ of PSR J1810+1744 [22]. Introducing DM rotation in core configurations has the same effect that could be seen in Fig. 4.5: The maximum allowed mass increases and the corresponding radius slightly decreases. On the other hand, halo configurations are almost identical whether or not the DM fluid rotates. This is because the extended halo surrounding the NS, with an equatorial radius much larger than that of the BM, has a significantly lower Kepler frequency (approximately 2 kHz) than that of the baryonic component (approximately 7 kHz). Consequently, the effect of DM rotation is negligible.

Lastly, we show how the moment of inertia depends on the choice of the BM EOS. To provide a more comprehensive analysis, in addition to the stiffer DD2npY-T and DD2 EOSs we also consider a softer IST EOS. The sequences are reported in the right panel of Fig. 4.8 with, respectively, solid, dashed, and dash-dotted lines. The values are computed at $f_{\mathrm{DM}} = 5\%$ for maximally rotating NSs and nonrotating DM.

In general, softer BM EOSs correspond to a smaller moment of inertia [255]. A similar effect can be achieved with the accumulation of heavy DM in the NS core, whereas light DM forming an extended halo increases the moment of inertia. Additionally, we present a transition case where a halo with a low DM fraction also leads to a decrease in the moment of inertia.

4.3 Summary and conclusions

Due to their fast spin and long evolution history, millisecond pulsars are ideal laboratories to study the effect of DM on NSs. In addition, millisecond pulsars representing old NSs are expected to contain a higher DM fraction, particularly important for this analysis. To allow the study of rapidly rotating DM-admixed NSs we have modified the public code `RNS` to include a second fluid. We have assumed the two fluids interact only gravitationally, are cold, and rotate rigidly around a shared axis. The DM distribution is automatically determined by the corresponding EOS and the central energy density value. The rotation is considered to be freely defined in both magnitude and direction.

DM is modeled by a bosonic self-interacting fluid with a quartic repulsive potential. To describe BM we have utilized three EOSs representing different classes of models with varying particle compositions, stiffness, and nuclear matter properties at the saturation density. Particularly, the DD2npY-T and DD2 EOSs with and without hyperons, respectively, formulated within the relativistic density functional approach and the parametric IST EOS. `RNS` is however not limited to these choices, and other EOSs can be studied as simply as they can be tabulated.

Since this is a multiparameter system, we have chosen to present sequences with a fixed DM fraction while considering two cases for the BM angular frequency: one corresponding to the Keplerian limit, where the star rotates at its maximum allowed frequency, and another for a realistic millisecond pulsar rotating at 716 Hz, the fastest observed spin rate to date [228, 229].

Our results indicate that incorporating DM in NSs preserves the overall qualitative behavior observed for pure baryonic stars. However, the quantitative changes depend strongly on the chosen parameters for both BM and DM components, with the DM particle mass and self-interaction playing a key role in distinguishing the core from the halo configurations in the static limit. Introducing BM rotation may blur this distinction—e.g., a halo may shift to a mixed state where the BM equatorial radius exceeds the DM's, but the DM's polar radius remains larger. Notably, at high masses, we observe a degeneracy of the oblateness among different DM configurations (at fixed baryonic radius and DM fraction). The oblateness peaks and then decreases linearly with the baryonic equatorial radius with nearly identical slopes for different DM particle masses. The moment of inertia also shows significant changes, decreasing for both core and halo configurations relative to the pure baryonic case.

The impact of rotation of the DM component at its Keplerian limit depends on its configuration: Cores increase the maximum mass–as rotation provides an apparent force that counteracts gravity– while halo configurations are highly sensitive to the parameters of both EOSs. In some cases, the DM remains as an extended halo with a minimal effect on the mass-radius diagram. This is due to the low Kepler frequency at which the DM component can rotate when compared to BM. In other cases DM becomes engulfed by the NS, effectively forming a very large core.

Finally, we examined consistently the case when DM rotates with the same absolute value of the angular velocity as BM, either corotating or counterrotating, reaching the BM Keplerian limit. An interesting observation for the core DM configurations is the following. For low-mass systems, where the BM Kepler angular velocity is low, configurations with corotating DM need a larger deformation of the DM component than counterrotating DM. As the mass increases and frame dragging effects grow, corotating configurations achieve higher angular velocities with a smaller deformation. In contrast, counterrotating configurations require progressively larger deformations to reach the BM Kepler limit, reaching very oblate DM configurations with a ratio of the polar to the equatorial DM radius lower than 0.35.

This analysis can be further extended in various ways. In particular, it would be interesting to investigate how the presented results depend on the variation in the self-interaction strength λ of the DM field, as described by Eq. (2.1). Comparison with experimental data could exclude portions of the $(\lambda, m_{\rm DM})$ parameter space. This can already be glimpsed for the DD2npY-T EOS looking at our results where, for the chosen λ and DM fraction, static core configurations with $m_{\rm DM} = 1\,\mathrm{GeV}$ are below the $2\,\mathrm{M}_\odot$ measurement [24, 25]. Maximally rotating stars would instead be driven below the same threshold for higher values of the mass. Another possibility is to move beyond the assumption of uniform rotation—suitable for old, isolated stars—and explore differential rotation, which is more relevant for remnants of binary neutron star mergers [52, 256–260].

The physical mechanisms driving dark matter rotation in admixed systems remain an open question, with several intriguing scenarios proposed. These include the inheritance of angular momentum from preexisting structures, asymmetric accretion as the neutron star moves through the surrounding dark matter halo (similar to the proposed seasonal modulation of dark matter flux due to the Earth's motion relative to the galactic halo [261]) and the aftermath of dark matter-admixed binary neutron star mergers [262].

The analysis performed in this work has significant implications for both current and future radio and X-ray observations of compact stars. The Square Kilometre Array (SKA) radio telescope [263], along with other radio telescopes, will focus on

precise measurements of NS moment of inertia, pulsar timing, and other NS properties. However, it is crucial to understand how accumulated DM might affect these quantities. As demonstrated in this study, the M(R) relations and moment of inertia exhibit a high degree of degeneracy, making it challenging to disentangle the effects of DM from the BM EOS. Therefore, measuring only the NS radius at a given mass would not be sufficient to distinguish DM effects or accurately probe the dense matter EOS.

On the other hand, present and future X-ray missions, such as NICER, eXTP (Enhanced X-ray Timing and Polarimetry Mission), and NewAthena (New Advanced Telescope for High-Energy Astrophysics), may encounter another effect related to DM – a potential impact on the formation and observation of hot spots [209, 236].

The presence of dark matter in neutron stars could be probed with static and dynamic effects. They include measuring the mass and radius of neutron stars with a few-percent accuracy [132], modification of the pulsar pulse profile due to the extra light-bending [235] and/or gravitational microlensing in the case of the existence of a dark halo, modification of the cooling rate of compact stars [122] as well as the aforementioned dark matter-admixed binary neutron star systems [262]. This is the subject of ongoing research.

In conclusion, this analysis highlights that interpreting X-ray, radio, and gravitational wave observations without considering the presence of accumulated DM could lead to missing crucial information or even misinterpreting the properties of strongly interacting matter at high densities. This becomes particularly relevant for NSs located in the Galactic Centre or dense DM regions, where DM density is expected to be high.

Chapter 5

Differentially rotating neutron stars with dark matter cores

This chapter has been published in near-identical form.
DOI: https://doi.org/10.48550/arXiv.2512.05898

Neutron stars (NSs) represent one of the most extreme environments in the Universe. Their mergers are key laboratories for strong field gravity, dense matter physics, and multimessenger astrophysics. The detection of GW170817 [1] confirmed binary neutron star (BNS) coalescence as a source of both gravitational waves (GWs) and electromagnetic counterparts, providing constraints on the dense matter equation of state (EOS) [264, 265]. Depending on the total mass and the underlying EOS, the post-merger remnant may form a hypermassive neutron star (HMNS), temporarily stabilized against collapse by differential rotation and thermal pressure [252, 266, 267], or promptly collapse into a black hole. Differential rotation is the dominant mechanism supporting such remnants, and its properties play a central role in determining their stability and lifetime. Uniformly rotating stars, on the other hand, are limited by the Keplerian frequency, the rotation rate at which matter at the equator follows a geodesic orbit, beyond which any further spin-up results in mass shedding.

On the other hand, differential rotation can sustain configurations well above this threshold [252, 268], producing hypermassive stars that survive for tens to hundreds of milliseconds before collapsing under the combined effects of angular momentum redistribution, magnetic breaking, and GW emission. Early studies of differentially rotating stars often relied on the "j-constant" law, in which the specific angular momentum is uniform throughout the star, leading to an angular velocity that decreases approximately as the inverse square of the distance from the rotation axis [269]. However, simulations of BNS mergers have shown that the resulting HMNS remnants exhibit a more complex rotational structure: a slowly rotating, nearly uniform core, an outer region with rapidly increasing angular velocity, and a radial decline consistent with a Keplerian profile [270–275]. To capture these features more realistically, several parameterized prescriptions for differential rotation have been introduced [53, 259, 276, 277], which reproduce the angular velocity profiles of merger remnants accurately for both polytropic and tabulated EOS [51, 257, 258].

On the other hand, many particle physics scenarios suggest that NSs may also host a dark matter (DM) component. In asymmetric DM models, particles accreted during a star's lifetime do not annihilate and therefore accumulate steadily in the stellar interior [234, 278–281]. The efficiency of this process depends both on envi-

ronmental factors, such as the local DM density, and on microphysical inputs, such as scattering cross-sections, production during core-collapse supernovae, or capture in the progenitor star [110, 111]. Self-interacting DM is particularly compelling, as it can simultaneously address small-scale tensions, e.g., the core-cusp problem in dwarf galaxies [282], in the cold DM paradigm, and provide sufficient pressure to form stable structures and prevent collapse into a black hole [283]. Depending on the particle mass and self-interaction strength, the dark component may settle into a compact core embedded in the NS or extend into a diffuse halo [284–286]. In either case, the presence of DM alters macroscopic observables such as the mass-radius relation and the moment of inertia, mimicking the effect of softening (in the case of the core morphology) and stiffening the baryonic EOS (in the case of the halo morphology) [239, 241, 243].

Previous works have investigated static or uniformly rotating DM-admixed NSs, as well as their role during the inspiral phase of BNS mergers [239, 240, 242, 244–247, 262, 287]. The case of long-lived differentially rotating remnants remains largely unexplored. The combined effect of differential rotation with a dark component opens new dynamical possibilities. A compact DM core could deepen the gravitational potential and accelerate collapse, while an extended halo could modify the moment of inertia and the spectrum of the remnant post-merger oscillations. The presence of DM may also shift stability boundaries and alter the maximum mass that HMNS can reach. Because the GW signal encodes the internal structure and composition of the remnant, these effects could leave detectable imprints on the kilohertz GW spectrum targeted by current and next-generation detectors [288].

Although dynamical simulations are ultimately required to capture the nonlinear evolution of merger remnants, they are computationally expensive and restricted to limited sets of initial conditions. Quasi-equilibrium models offer a complementary approach to explore the parameter space systematically. They have already proven useful in interpreting post-merger GW spectra, estimating threshold masses for prompt collapse, and constructing empirical relations between remnants and non-rotating stars [51, 252, 289–292]. Extending this methodology to two-fluid systems enables us to investigate how DM modifies these universal relations and to identify

possible multimessenger signatures. Our study, therefore, occupies an intermediate ground between microphysical modeling and full merger simulations, providing a controlled framework to isolate the impact of DM of various fractions and rotation law on HMNS stability and structure.

In this work, we construct equilibrium sequences of differentially rotating, DM-admixed NSs using an extended version [287] of the `RNS` code [41, 42], adapted to treat two gravitationally coupled fluids. We focus on representative configurations that highlight the role of the dark component in shaping the maximum mass, angular velocity profile, and stability boundaries of HMNS remnants. We should note that this approach is different from the DM admixed NSs modeled as fermion-bosonic compact objects [247, 293]. A study of differentially rotation in this case is also underway [294].

The paper is organized as follows. In Section 5.1 we describe our numerical setup and the assumptions adopted for the differential rotation law. Section 5.2 discusses the equilibrium sequences obtained and their astrophysical implications. Finally, Section 5.4 summarizes our findings and outlines future directions.

Unless otherwise stated, we employ geometrized units with $G = c = 1$ and express all quantities in solar-based units. Energy densities and pressures are shown in cgs units to facilitate comparison with the standard tabulated nuclear EOS. For the DM EOS, the natural units $\hbar = c = 1$ are used.

5.1 Theoretical framework

Employing the Komatsu-Eriguchi-Hachisu (KEH) scheme [40] with the modifications introduced in [43], the Einstein's field equations can be solved within stationary and axial symmetry. The generic line element takes the form

$$\begin{aligned} \mathrm{d}s^2 &= g_{\mu\nu}\mathrm{d}x^\mu \mathrm{d}x^\nu \\ &= -e^{\gamma+\rho}\mathrm{d}t^2 + e^{2\alpha}(\mathrm{d}r^2 + r^2\mathrm{d}\theta^2) + e^{\gamma-\rho}r^2\sin^2\theta(\mathrm{d}\phi - \omega\mathrm{d}t)^2, \end{aligned} \tag{5.1}$$

where $\gamma, \rho,\ \mu$ and ω are the metric fields which depend on r and θ. The metric fields and matter distribution are computed iteratively starting from an initial guess, typically a nonrotating star.

To model numerically differentially rotating DM admixed NSs, we expand on the work presented in [287], where the `RNS` code was extended to model uniformly rotating NSs with DM. Denoting the specific enthalpy of the fluid $\mathrm{X} \in \{\mathrm{BM}, \mathrm{DM}\}$ as H_{X}, the fluid's four-velocity as u^{μ}_{X} and the specific angular momentum $j_{\mathrm{X}} = g_{\mu\phi} u^{t}_{\mathrm{X}} u^{\mu}_{\mathrm{X}}$, the first integral of the hydrostationary equilibrium is written as

$$H_{\mathrm{X}} - \ln u^{t}_{\mathrm{X}} + \int_{0}^{j} \tilde{j}_{\mathrm{X}} \frac{\mathrm{d}\Omega_{\mathrm{X}}}{\mathrm{d}\tilde{j}_{\mathrm{X}}} \mathrm{d}\tilde{j}_{\mathrm{X}} = \text{const.} \tag{5.2}$$

Coupling Eq. (5.2) with an explicit expression for the angular velocity $\Omega(j)$ and an EOS, an updated matter distribution can be found. Then, the metric potentials are recomputed. This procedure continues until convergence is reached. For a more comprehensive description of the algorithm, see for example [40, 51, 259, 269].

Of utmost importance is the choice of the angular velocity profile $\Omega(j)$. Many laws have been proposed, aimed at describing the profiles found in proto-NSs and remnants of BNS mergers. The classic "j-constant" law is

$$j(\Omega) = A^2(\Omega_c - \Omega) \tag{5.3}$$

where A is a positive constant that determines the length scale over which the angular velocity varies within the star and Ω_c is the angular velocity at the rotation axis. Although this law describes the proto-NS profile well [50], it falls short in the case of BNS mergers [51, 52].

A particularly important family of laws has been proposed in [53]: they all feature a peak in the rotation profile and a Keplerian fall-off. We will employ the following rotation law:

$$\Omega(j) = \Omega_c \frac{1 + \frac{j}{B^2\Omega_c}}{1 + \left(\frac{j}{A^2\Omega_c}\right)^4} \tag{5.4}$$

that has been widely used in the literature. While Eq. (5.4) describes a general

differential rotation profile, in this work we apply it exclusively to the baryonic component (i.e., $\Omega_{\rm BM}$ follows this law). The dark matter component is instead assumed to rotate uniformly ($\Omega_{\rm DM} = \text{const}$), to approximate the behaviour of dark matter cores in merger simulations [262].

Throughout this work, we employ dimensionless quantities to characterize the DM and BM components of the star. For the global properties, we define

$$f^M_{\rm DM} = \frac{M_{\rm DM}}{M_{\rm BM} + M_{\rm DM}}, \quad f^J_{\rm DM} = \frac{J_{\rm DM}}{J_{\rm BM} + J_{\rm DM}}, \tag{5.5}$$

which represent, respectively, the fraction of the total mass and the fraction of the total angular momentum carried by the DM component. These parameters provide a compact way to quantify the relative importance of DM in the global equilibrium, independent of the absolute values of the mass and angular momentum.

To characterize the rotational structure of each fluid, we introduce two additional dimensionless ratios,

$$\lambda^X_1 = \frac{\Omega^X_{\rm max}}{\Omega^X_c}, \tag{5.6}$$

$$\lambda^X_2 = \frac{\Omega^X_e}{\Omega^X_c}, \tag{5.7}$$

with $X \in \{\rm BM, DM\}$. Here Ω^X_c is the angular velocity on the rotation axis, Ω^X_e the value at the equator, and $\Omega^X_{\rm max}$ the maximum angular velocity attained inside the star measured by an observer at infinity. The parameters λ^X_1 and λ^X_2, therefore, capture the degree of differential rotation of the fluid: λ_2 measures how rapidly the equatorial layers rotate relative to the core, while λ_1 determines the strength and location of the peak in $\Omega(r)$. In the one-fluid case, these two ratios are commonly used to classify differentially rotating equilibria into morphological families (Types A, B, C, and D) [54, 295], and in our two-fluid framework, they play the same role in identifying whether a configuration is quasi-spherical or toroidal. Our setup in `RNS` can recover only two of those. Type A solutions correspond to stars featuring a maximum of the energy density at the center. Unlike other solution types, their

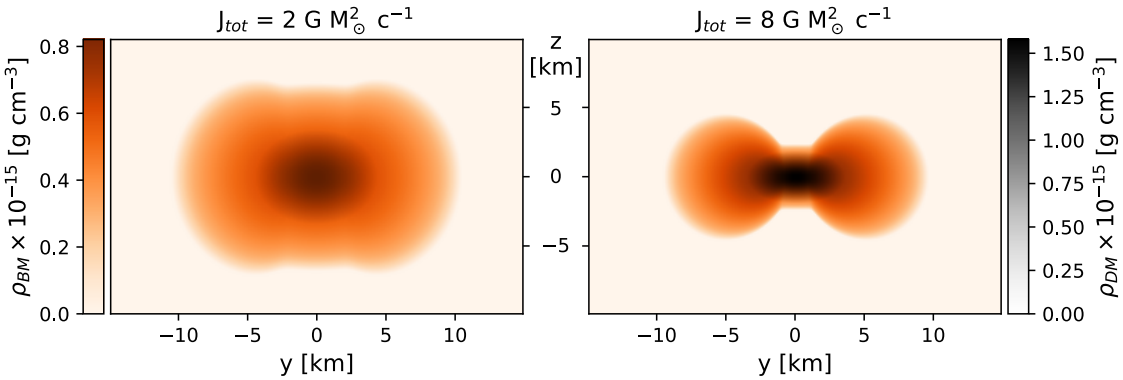

Figure 5.1: BM and DM density profiles in the yz plane of two configurations with the same baryonic central energy density $\epsilon^c_{\rm BM} = 0.75 \times 10^{15}\,{\rm g\,cm^{-3}}$ and $f^M_{\rm DM} = 5\%$, $f^J_{\rm DM} = 1\%$, $(\lambda_1, \lambda_2) = (2, 0.5)$.

overall morphology remains quasi-spherical, but the internal distribution of angular velocity can vary substantially depending on the rotation parameters. On the other hand, Type C solutions exhibit toroidal-like structures with off-center density maxima, where stronger differential rotation significantly alters the star's shape and allows for higher maximum masses. In this work, we construct sequences of both types, covering the diversity of morphologies permitted by differential rotation and systematically exploring how the presence of a DM component modifies their equilibrium and global properties.

5.2 Results

Differentially rotating NSs described by the rotational law (5.4) can serve as proxies for remnants formed in BNS mergers. Throughout this chapter we employ the DD2 equation of state of Section 1.2 to describe the baryonic matter component. Since we are interested in stationary equilibrium configurations, it is natural to compare with such merger remnants as obtained in numerical relativity simulations. A relevant example is provided in [262], which considers two-fluid systems in both core and halo configurations.

Among the models discussed there, we focus on those featuring a DM core. In such configurations, as illustrated in the bottom-right panel of Fig. 5 of [262], the simulations indicate that the two fluids follow distinct kinematic behaviours: while the baryonic matter exhibits strong differential rotation, the dark matter core tends to rotate almost uniformly. Although the simulations show that the core profile evolves in time (oscillating slightly) and that a fraction of the dark matter is expelled into a disk with a more complex rotation profile, we neglect these transient effects and the secondary disk component here. Consequently, for the stationary equilibria constructed in this work, we adopt strict uniform rotation for the dark matter component as the most physically motivated approximation for the late-time state of the remnant, in contrast to the differential rotation imposed on the baryons. For the remainder of this work, we will therefore assume that Eqs. (5.6) and (5.7) refer exclusively to the BM component, and we omit the corresponding tag to simplify the notation. We leave halo configurations for future work, as their angular velocity profiles cannot be reproduced with the rotation laws currently implemented in `RNS`. These profiles feature a maximum displacement from the origin and an angular velocity that increases linearly near the center. In contrast, in BM configurations, the core rotates almost uniformly, with strong differential rotation confined to the outer layers.

5.2.1 Toroidal configurations

Figure 5.1 shows two NS representative configurations with a DM core with different angular momenta – one with slower rotation (left), keeping a more spherical-like shape, and one with a very high angular momentum (right), making the star highly elongated. The specific choice of $\lambda_1 = 2$ and $\lambda_2 = 0.5$ gives rise, for sufficiently high angular momentum, to the characteristic toroidal shape, commonly referred to as *Type C solution* (see, e.g., [54, 258]) where an off-center maximum of the energy density is observed, as shown in Fig. 5.1. The angular velocity profile is characterized by an almost uniformly rotating core, followed by a sharp rise to a maximum value determined by λ_1, and then a slow decrease approaching the Keplerian law $\Omega \propto$

$r^{-3/2}$. In both panels of Fig. 5.1, the DM component carries 1% of the total angular momentum $J_{\rm tot}$ and maintains a quasi-spherical shape, as it rotates uniformly apart from small deviations induced by frame dragging.

Figure 5.2 shows equilibrium sequences for selected configurations in the $(M, \epsilon^c_{\rm BM})$ plane at various values of the total angular momentum $J_{\rm tot}$, ranging from 0 to $8\,{\rm G\,M_\odot^2\,c^{-1}}$, each identified by one color sampled from black to aquamarine. Dashed lines represent, for reference, the one-fluid description of isolated NSs; red dots indicate the maximum mass for each sequence. Solid (dash-dotted) lines correspond to models with constant values of the DM to BM ratio $f^M_{\rm DM} = 5\%$, while the angular moment fraction is $f^J_{\rm DM} = 1\%$ ($f^J_{\rm DM} = 5\%$). Red circles (triangles) on each line mark their respective maximum mass. Finally, dotted lines illustrate configurations with constant $f^M_{\rm DM} = 5\%$ and much higher, near Keplerian limit, rotation of the DM component $\Omega_{\rm DM} = 0.75\,\Omega^{\rm DM}_{\rm K}$; their maximum masses are indicated by stars.

We adopt the DM mass fraction of $f^M_{\rm DM} = 5\%$, consistent with the values used in [109, 262], in order to enable a meaningful comparison. This value is consistent with observations of $2\,{\rm M_\odot}$ NSs together with $\Lambda_{1.4} \leq 580$ constraint [2], set by LIGO-Virgo Collaboration. For the angular momentum partition, we adopt a fiducial $f^J_{\rm DM} = 1\%$ to probe the impact of a slowly rotating, quasi-uniform DM component, and we also show sequences with $f^J_{\rm DM} = 5\%$ to illustrate the trend when the DM carries a larger fraction of the total rotation. The choice $f^J_{\rm DM} = 1\%$ is intentionally modest: with $f^M_{\rm DM} = 5\%$ the DM core cannot (within our microphysical assumptions) sustain arbitrarily large angular momentum. Setting $f^J_{\rm DM} = 5\%$ already eliminates most of the previously accessible parameter space, as can be seen looking at Fig. 5.2.

Finally, the dotted sequences with $\Omega_{\rm DM} = 0.75\,\Omega^{\rm DM}_{\rm K}$ represent an extreme, near-Kepler case for a rapidly rotating DM component. Figure 5.3 shows the distribution of these models as a function of $f^J_{\rm DM}$. The blue histogram includes all models from Fig. 5.2, while the red bars indicate only those on the stable branches. Most models have $f^J_{\rm DM} < 2\%$, with a few outliers reaching up to $f^J_{\rm DM} = 12.3\%$. These extreme cases occur exclusively in slowly rotating sequences, where even big fractions correspond to relatively small angular momenta. Among the computed models, only in sequences with $J_{\rm tot} < 2\,{\rm G\,M_\odot^2\,c^{-1}}$ we obtain configurations near the maximum with $f^J_{\rm DM} > 4\%$.

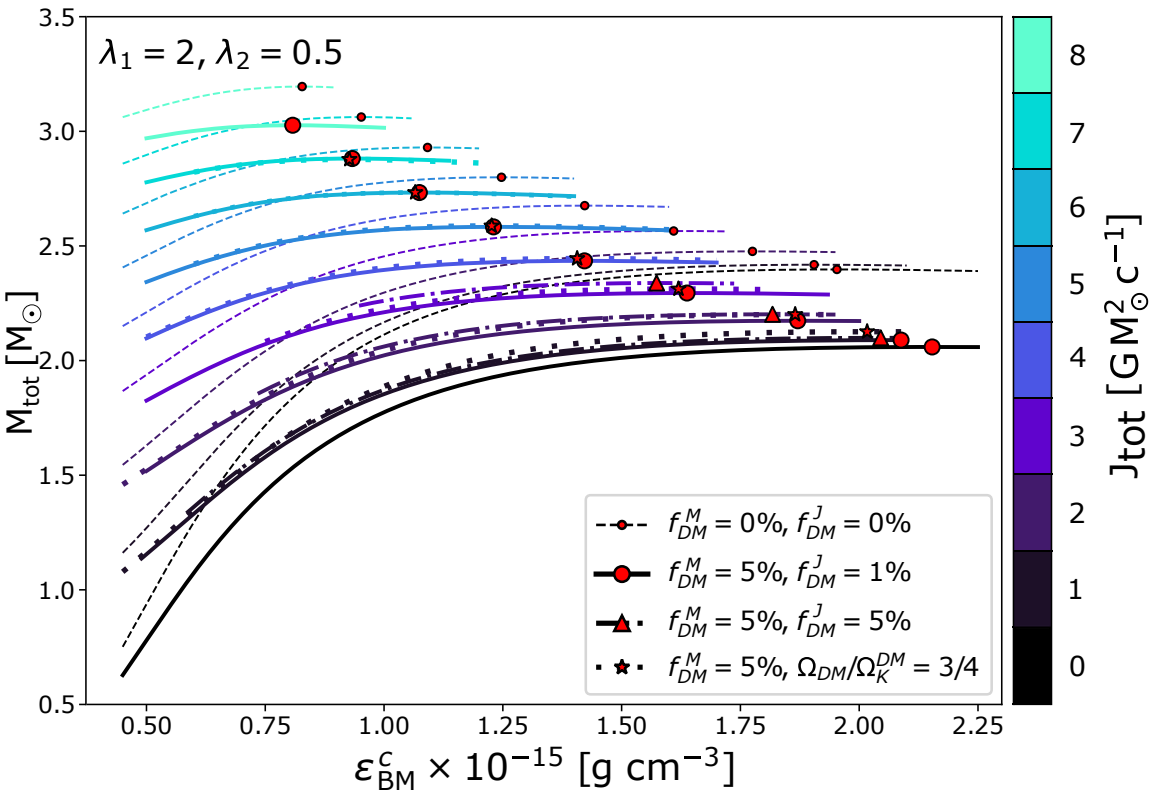

Figure 5.2: Mass vs BM central energy density sequences for the DD2 EOS and rotational parameters $\lambda_1 = 2$ and $\lambda_2 = 0.5$. The sequences have fixed total angular momentum $J_{\rm tot}$, represented with the color gradient. Dashed lines represent solutions with $f^M_{\rm DM} = 0\%$, solid lines show solutions with $f^M_{\rm DM} = 5\%$ and $f^J_{\rm DM} = 1\%$. Both have been computed up to $J_{\rm tot} = 8\,{\rm G\,M_\odot^2\,c^{-1}}$. Dash-dotted lines represent solutions with $f^M_{\rm DM} = 5\%$ and $f^J_{\rm DM} = 5\%$, computed up to $J_{\rm tot} = 4\,{\rm G\,M_\odot^2\,c^{-1}}$ and finally dotted lines solutions with $f^M_{\rm DM} = 5\%$ and $\Omega_{\rm DM}/\Omega^{\rm DM}_{\rm K} = 3/4$, computed up to $J_{\rm tot} = 7\,{\rm G\,M_\odot^2\,c^{-1}}$. The red symbols report the sequence maximum mass, marking the turning point. Strictly speaking, for rotating configurations, the onset of instability corresponds to the zero-frequency of the fundamental oscillation mode [296] and does not coincide exactly with the turning-point line. However, since the two boundaries are typically very close, we adopt the turning point as an approximation for the stability limit [289, 297]. Since a nonlinear monotonic relationship exists between central and maximum energy density for all reported models, we present the results as a function of the former, which is the parameter used to generate the models.

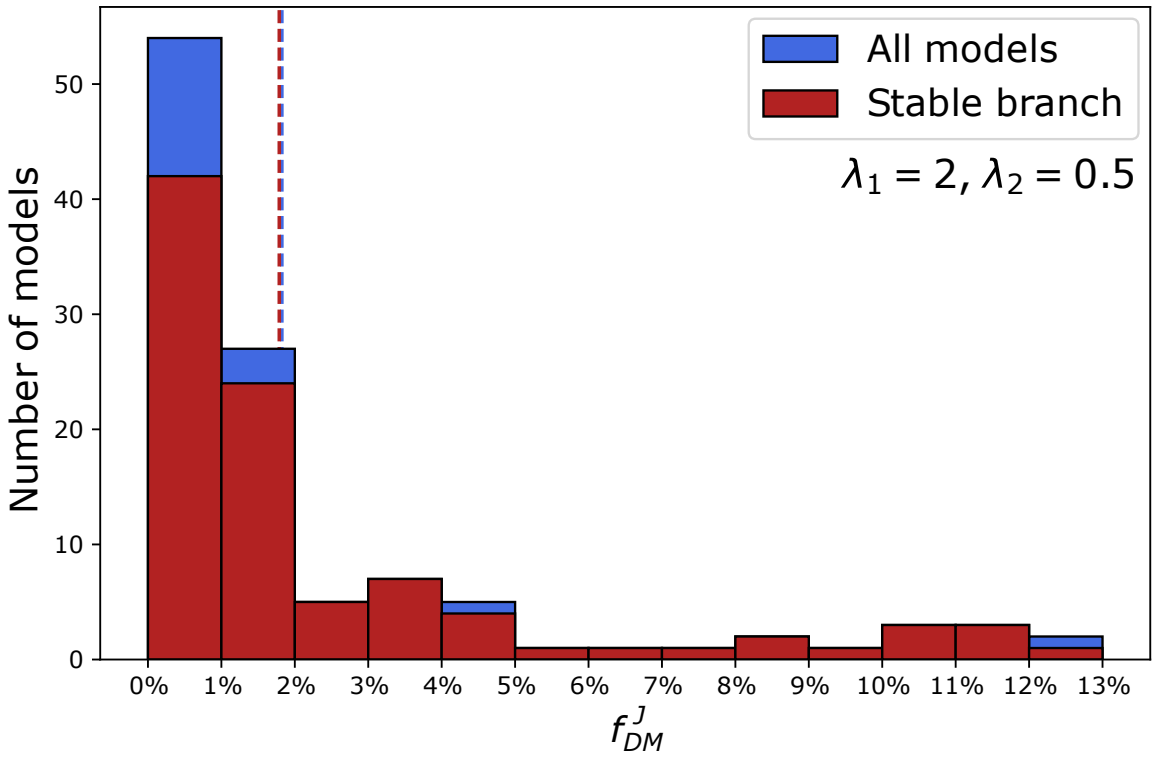

Figure 5.3: Distribution of the angular momentum fraction in the DM component for models rotating at 75% of their Kepler frequency. Blue and red bars represent the full sample and the stable models only, respectively. Dashed lines indicate the average values: $f^J_{\rm DM} = 2.68\%$ for the former and $f^J_{\rm DM} = 2.65\%$ for the latter. Models with $f^J_{\rm DM} > 4\%$ exhibit low total angular momentum ($J_{\rm tot} < 2\,{\rm G\,M_\odot^2\,c^{-1}}$) and lie near the maximum of their respective sequence. These models are sampled uniformly along the dotted sequences shown in Fig. 5.2.

Specifically, for $J_{\rm tot} = 1\,{\rm G\,M_\odot^2\,c^{-1}}$ this occurs for $M_{\rm tot} > 1.64\,{\rm M_\odot}$, and for $J_{\rm tot} = 2\,{\rm G\,M_\odot^2\,c^{-1}}$ for $M_{\rm tot} > 2.14\,{\rm M_\odot}$, to be compared with the respective maximum stable masses of $2.12\,{\rm M_\odot}$ and $2.19\,{\rm M_\odot}$.

Within the explored parameter space, Fig. 5.3 indicates that sequences with fixed $f^J_{\rm DM} = 1\%$ are representative of the typical behavior found in our models. Alternative assumptions, e.g. larger $f^M_{\rm DM}$, different DM rotation laws, or strong DM self-interaction, will only change the results quantitatively.

The inclusion of a DM component generally leads to a reduction in the maximum

$(f^M_{\rm DM},\, f^J_{\rm DM})\%$	α	β	γ	$M_{\rm max,J=0}$ [$M_\odot$]
(0, 0)%	0.284	0.027	0.496	2.398
(5, 1)%	0.269	0.022	0.454	2.059
(5, 5)%	0.365	0.168	1.316	2.059
(5%, $\frac{\Omega_{\rm DM}}{\Omega^{\rm DM}_K} = 3/4$)	0.396	0.164	1.739	2.059

Table 5.1: Fitting parameters for the model. The constants α, β, and γ are reported in dimensionless units.

gravitational mass supported by the configuration. This is expected in the case of core-type distributions, where the additional gravitational pull from a centrally concentrated DM core effectively softens the system [298]. The BM component experiences a stronger total gravitational potential without receiving a corresponding increase in central pressure support, leading to an earlier onset of instability.

With the increase of the total angular momentum $J_{\rm tot}$, the difference between the DM admixed and pure BM NS decreases if one compares sequences with the same $J_{\rm tot}$. The dependence of the maximum total gravitational mass on the total angular momentum is represented in Fig. 5.4, that shows the normalized maximum mass $\hat{M} = M_{\rm max}/M_{\rm max,J=0}$ as a function of the squared normalized total angular momentum $\hat{J}^2_{\rm tot} = J^2_{\rm tot}/M^4_{\rm max,J=0}$. The different markers denote configurations with varying mass and angular momentum fractions in the DM component, as indicated in the legend.

The solid lines are fitted on the points using a [2/1] Padé resum of the Hartle-Thorne expansion in $\hat{J}^2_{\rm tot}$ [31]:

$$\hat{M}(\hat{J}^2_{\rm tot}) = 1 + \frac{\alpha \hat{J}^2_{\rm tot} + \beta \hat{J}^4_{\rm tot}}{1 + \gamma \hat{J}^2_{\rm tot}}, \tag{5.8}$$

which captures the leading-order rotational corrections and ensures a controlled behavior at large $J^2_{\rm tot}$. The fitting parameters are reported in Table 5.1.

In the bottom panel, we plot the logarithm of the absolute value of residuals; the fits reproduce the numerical data with high accuracy, typically within 10^{-4}. The

exception is the sequence at constant fraction $\Omega_{\rm DM}/\Omega_{\rm K}^{\rm DM}$ (in red), which shows slightly larger deviations but still remains within acceptable bounds.

Overall, rotation softens the DM induced reduction of the maximum mass due to the DM component, and all configurations at constant fraction of angular momentum show a common scaling with $J_{\rm tot}^2$, albeit with subtle differences that depend on the DM rotational properties: small values of $f_{\rm DM}^J$ ($\sim$ 1%, orange line) tend to slow down the increase of $M_{\rm max}$ with respect to the one-fluid case, while higher values ($\sim$ 5%, green line) increase it. Curves at constant angular velocity (red line) show instead a completely different behavior, in which Eq. (5.8) has a positive second derivative and a much steeper increase.

We now turn our attention to the sequences characterized by $f_{\rm DM}^J = 5\%$, shown in Fig. 5.2 (dash-dotted lines). As can be seen, we were able to compute sequences only for relatively low values of $J_{\rm tot}$, ranging from 0 to $3\,{\rm G\,M_\odot^2\,c^{-1}}$, and generally for a narrower range of central energy densities $\epsilon_{\rm BM}^c$. Figure 5.5 provides further insight into the situation. It shows $\epsilon_{\rm BM}^c$ as a function of the resulting $r_{\rm ratio}^{\rm DM}$, which reflects the deformation of the DM fluid. Increasing the target total angular momentum (and thus $J_{\rm DM} = f_{\rm DM}^J J_{\rm tot}$) shifts the sequence toward lower values of this ratio.

As previously observed in [287], the `RNS` code faces difficulties when computing solutions involving very large deformations, even if the angular velocity remains below the Kepler limit. For smaller values of $f_{\rm DM}^J$, the code cannot compute configurations with $\epsilon_{\rm BM}^c < 0.5 \times 10^{15}\,{\rm g\,cm^{-3}}$ despite their potentially large total masses, because building these configurations would require deformations beyond the code's capability. Similarly, attempts to construct sequences with $J_{\rm tot} \geq 4\,{\rm G\,M_\odot^2\,c^{-1}}$ at $f_{\rm DM}^J = 5\%$ lead to numerical problems with solutions having $r_{\rm ratio}^{\rm DM} \lesssim 0.4$, a regime close to the apparent limit of the code's numerical stability and convergence. Consequently, constructing DMANS with higher angular momentum is not possible for large $f_{\rm DM}^J$ within the current framework. This prevents us from reaching the realistically high angular momenta ($J > 5\,{\rm G\,M_\odot^2\,c^{-1}}$) expected after a merger. This suggests that alternative differential rotation laws may be needed to plausibly model these high-J scenarios.

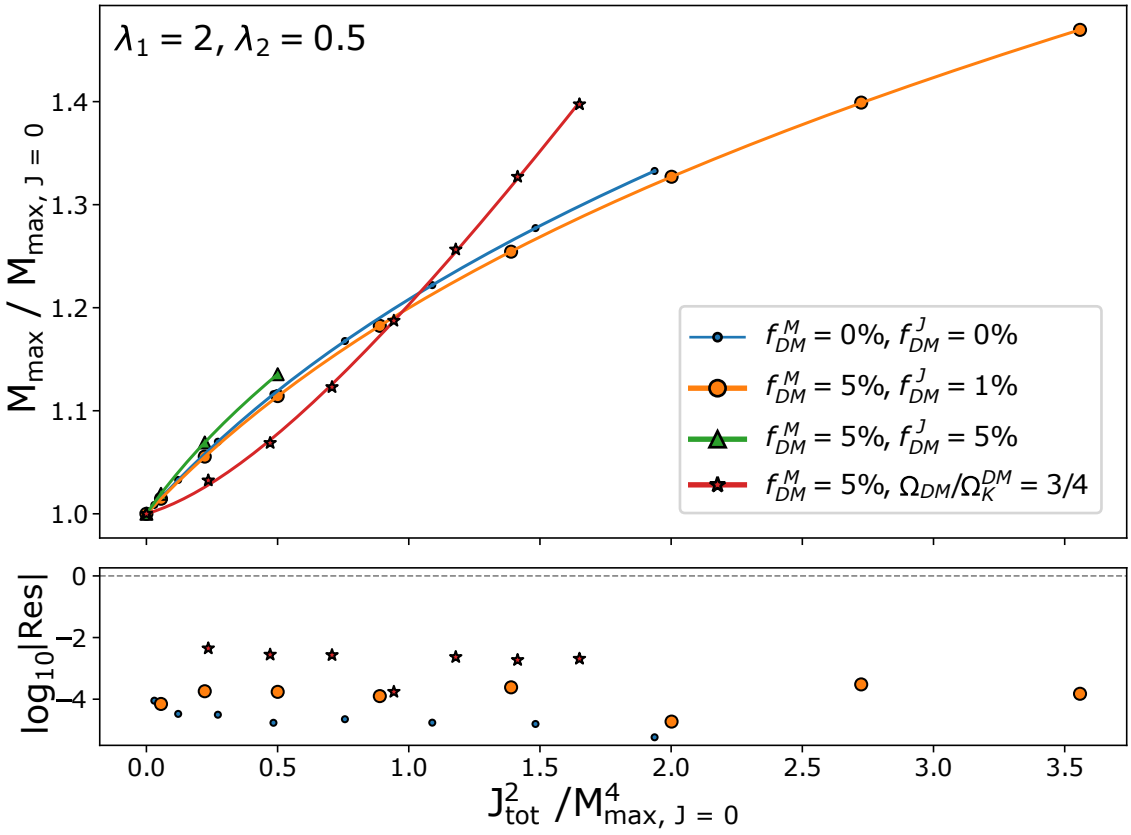

Figure 5.4: Normalized gravitational mass vs square of the total angular momentum for the same configurations computed in Fig. 5.2. Colored lines are fitted with Eq. (5.8). The bottom panel shows the logarithm of the absolute value of the residuals.

5.2.2 Quasi-spherical configurations

In cases where the remnant of a BNS merger does not undergo immediate gravitational collapse to a black hole, it can form a hypermassive or supramassive NS that is sustained against gravitational collapse due to the rapid differential rotation. Due to the longer lifetime of such merger remnants, they have enough time to settle into a more quasi-spherical state before any delayed instability arises. Such configurations are often modeled using equilibrium sequences, particularly those classified as Type A, which describe rotating stars retaining a maximum energy density at

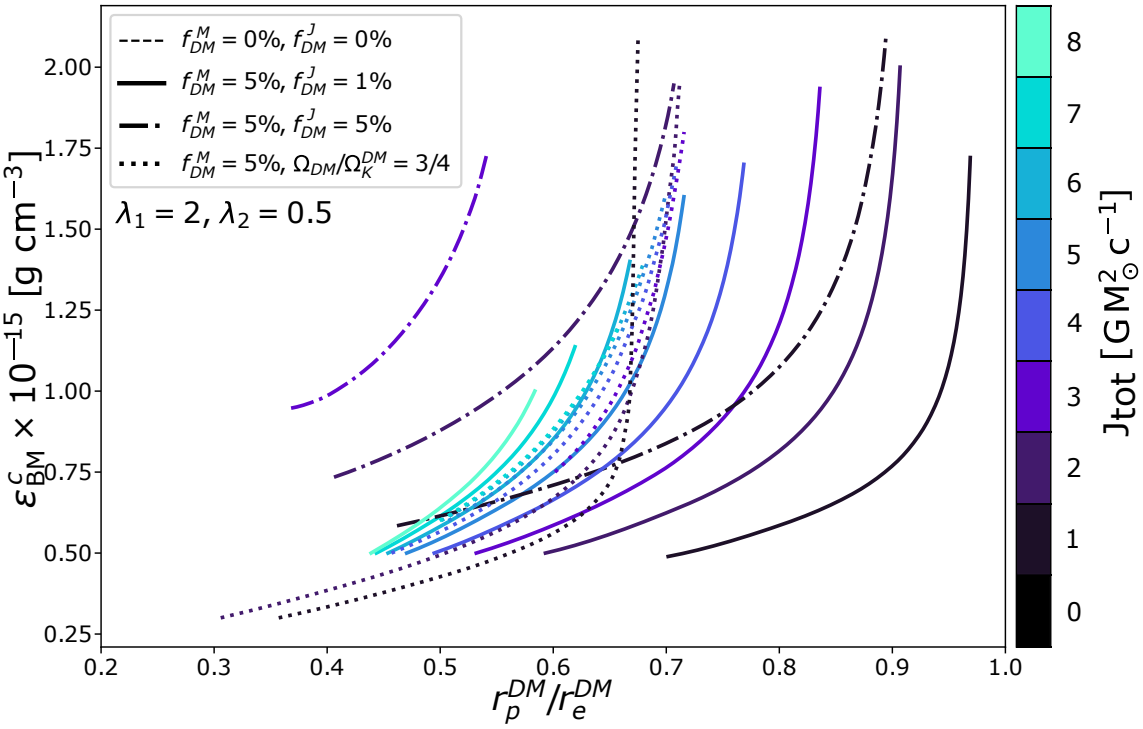

Figure 5.5: Central energy density of the BM component as a function of the DM deformation parameter. Lines and colors have the same meaning as in Fig. 5.2.

the center and remaining close to spherical symmetry despite increasing rotational flattening (quantified by $r^{\rm BM}_{\rm ratio}$). To obtain these solutions, we adjust the parameters in (5.6) and (5.7) from $(2, 0.5)$ to $(\lambda_1, \lambda_2) = (1.8, 1)$. We choose these parameters following [258, 271, 299], where they report that numerical simulations suggest that $\lambda_2 \approx 1$ and $\lambda_1 \in [1.7, 1.9]$ better approximate remnants from BNS merger. Two models are shown in Fig. 5.6.

Figure 5.7 shows sequences in the $(M_{\rm tot}, \epsilon^c_{\rm BM})$ plane at fixed total angular momentum, with colors and line styles consistent with Fig. 5.2. Maximum-mass points are marked with filled symbols and a black edge. For the quasi-spherical configurations corresponding to $(\lambda_1, \lambda_2) = (1.8, 1)$, we find that for $J_{\rm tot} < 2\,{\rm G\,M^2_\odot\,c^{-1}}$ the resulting equilibrium sequences essentially coincide with those of the toroidal case shown in

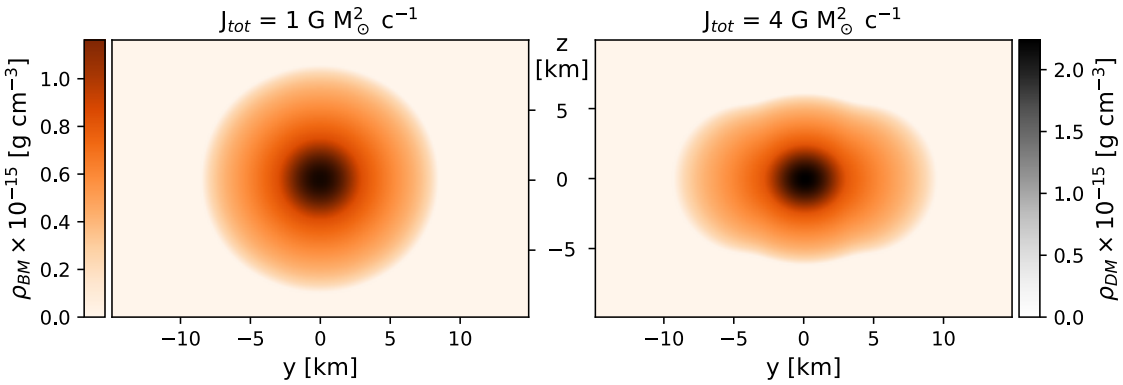

Figure 5.6: Matter density profiles in the yz plane of two configurations with the same baryonic central energy density $\epsilon^c_{\rm BM} = 1.47 \times 10^{15}\,{\rm g\,cm^{-3}}$ and $f^M_{\rm DM} = 5\%$, $f^J_{\rm DM} = 1\%$, $(\lambda_1, \lambda_2) = (1.8, 1)$.

Fig. 5.2. Although the angular-velocity profiles differ substantially, the global quantities such as $M_{\rm tot}$ remain nearly unchanged at low angular momentum, indicating that the detailed form of $\Omega(r)$ has only a minor influence in this regime.

At higher values of $J_{\rm tot}$, up to the maximum accessible value of $5\,{\rm G\,M_\odot^2\,c^{-1}}$ in our numerical sequences, the maximum supported mass is consistently lower than in the Type C case. This confirms, in the two-fluid scenario, the result already reported in [258, 295] for one-fluid stars: Type A configurations are less efficient in exploiting differential rotation to increase the maximum mass.

In the two-fluid case, even at moderate central densities, the BM equatorial angular-velocity profile $\Omega(r)$ develops a local minimum around $R \simeq 4\,{\rm km}$ before rising sharply to its maximum and then approaching the Keplerian fall-off. This minimum reflects the influence of the DM component and is not produced by applying the rotation law of Eq. (5.4) to a single fluid, where $\Omega(r)$ instead increases monotonically outside the nearly flat core. Although similar minima can arise in one-fluid models under different rotation prescriptions [259], they do not appear under the assumptions adopted here. Figure 5.8 compares the equatorial profiles for the one-fluid (left) and two-fluid (right) descriptions across several values of the BM central energy density.

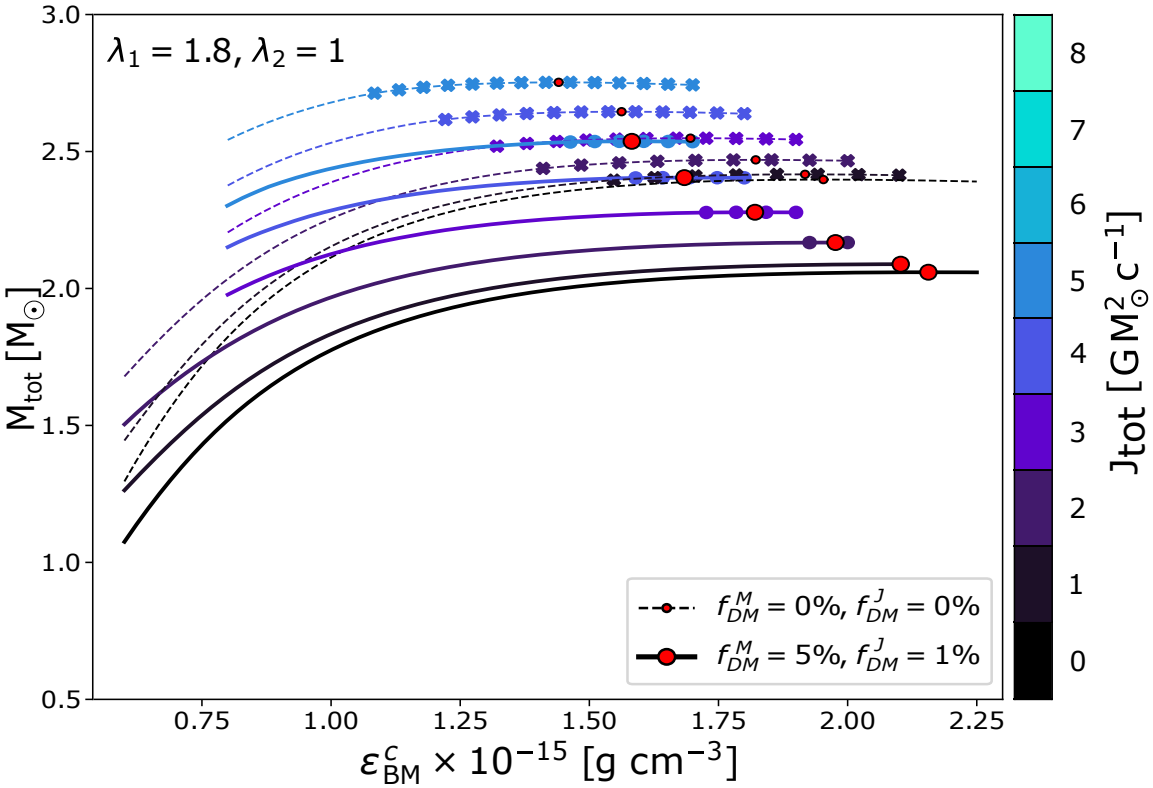

Figure 5.7: Gravitational mass vs baryonic central energy density for $\lambda_1 = 1.8$ and $\lambda_2 = 1$ at fixed total angular momentum $J_{\rm tot}$, represented with the color gradient. Dashed lines correspond to solutions with $f^M_{\rm DM} = 0\%$, solid lines to $f^M_{\rm DM} = 5\%$ and $f^J_{\rm DM} = 1\%$. Crosses and circles without the black edge represent cases for which the profile $\Omega(r)$ is discontinuous (*cf.* Appendix 5.3 and Fig. 5.8) for $f^M_{\rm DM} = 0\%$ and $f^M_{\rm DM} = 5\%$, respectively.

The minimum occurs because the DM slightly reduces the enclosed mass in the region where it is present, allowing $\Omega(r)$ to decrease locally while still satisfying the fixed total angular momentum $J_{\rm tot}$. Farther out, where $\Omega(r)$ reaches its maximum, the DM instead deepens the gravitational potential, requiring a steeper rise in $\Omega(r)$ for centrifugal support and producing a more pronounced peak than in the one-fluid case. This interplay between reduced and enhanced gravitational pull is visible in Fig. 5.8.

Note that not all models along these sequences converge to physically valid so-

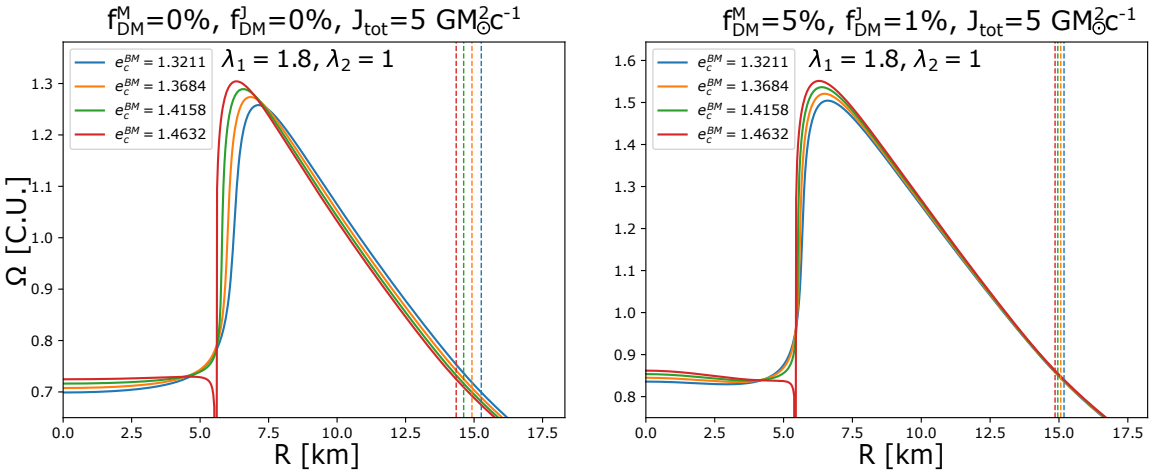

Figure 5.8: Angular velocity on the equatorial plane as a function of the proper radial position. Dashed lines mark the position of the star's surface. Left: example models extracted from Fig. 5.7 in the absence of DM. Right: same as the previous panel, but for a DM fraction of 5%.

lutions. In particular, for certain combinations of high central energy density and angular momentum, the rotation law in Eq. (5.4) ceases to admit real solutions for $\Omega(r)$ over a finite radial range. As a result, the corresponding equilibrium profiles develop discontinuities in the angular velocity, which we mark with open symbols in Fig. 5.7. A discussion of the origin and impact of these discontinuities, together with a validation of our implementation against published equilibrium models, is presented in Section 5.3.

5.3 Analysis of angular velocity discontinuities

Quasi-spherical models with $(\lambda_1, \lambda_2) = (1.8,\ 1)$ lead to convergence issues even in the one-fluid scenario, especially at high central densities and angular momenta.

Points marked with dots or crosses without black edges on the sequences (respectively for the two-fluid and one-fluid cases) of Fig. 5.7 correspond to models where the angular velocity profile $\Omega(r)$ becomes discontinuous, indicating failure of the iteration procedure. These discontinuities arise because the rotation law (5.4) ceases

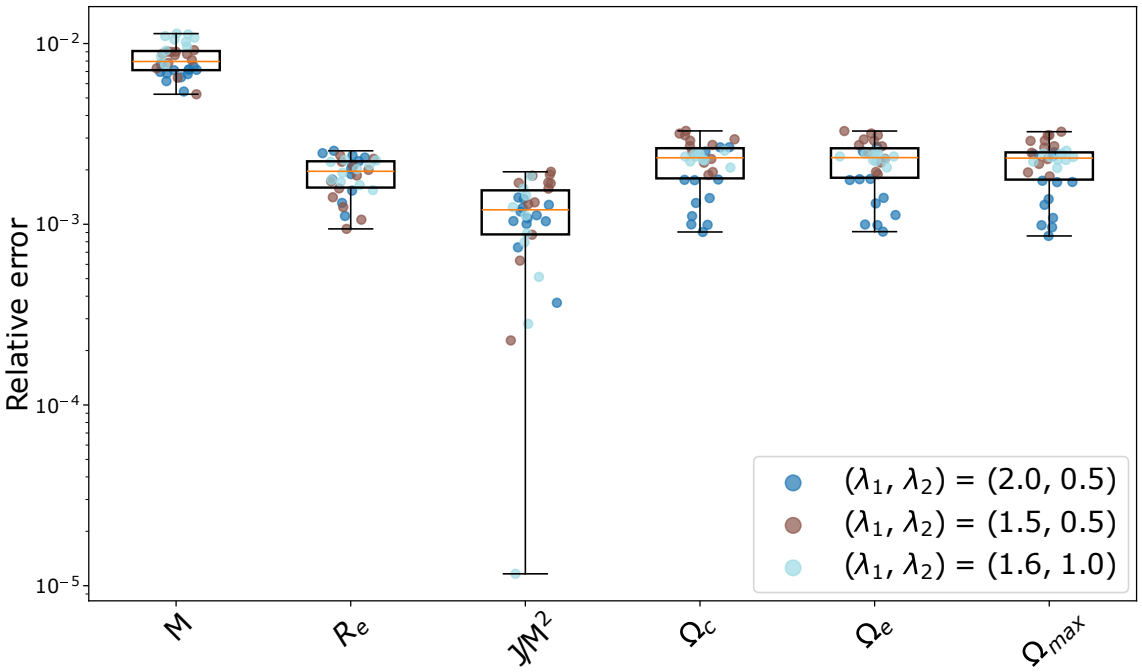

Figure 5.9: Relative errors of models computed in the one-fluid picture, compared against Table 6 of [258] for the DD2 EOS. We assess both global quantities (gravitational mass M and dimensionless angular momentum J/M^2) and local ones (equatorial radius R_e, central and equatorial angular velocities, and the maximum angular velocity). Dots represent individual models, with each color corresponding to one of the three (λ_1, λ_2) pairs considered. The orange line marks the median relative error, while the lower and upper edges of the box indicate the 25% and 75%, respectively.

to admit positive real solutions for Ω over a finite radial range, as illustrated in Fig. 5.8, where we show different equatorial angular velocity profiles Ω as a function of the proper radius R for a fixed total angular momentum $J = 5\,\mathrm{G\,M_\odot^2\,c^{-1}}$. Colors correspond to different central BM energy densities, used as the sequence parameter. The left panel shows the one-fluid case ($f^M_{\rm DM} = f^J_{\rm DM} = 0$), and the right panel shows a two-fluid configuration with $f^M_{\rm DM} = 5\%$ and $f^J_{\rm DM} = 1\%$.

For sufficiently high $\epsilon^c_{\rm BM}$, the equation $\Omega = j(\Omega)$ fails to yield a real, positive solution over a finite radial interval, producing discontinuities visible in the red curves of Fig. 5.8. Although the code provides a numerical solution, such discontinuities

imply that the model is not physically reliable and cannot be used as initial data for numerical relativity codes.

The impact on equilibrium sequences is minimal, as the discontinuities are confined to a few radial grid points near the equator. When computing integral quantities, such as the gravitational mass, the resulting error is negligible. Other field quantities involved in the integrals, such as pressure or energy density, exhibit jumps in the radial profile of up to 5% relative to neighboring points in the worst observed case, affecting at most six radial grid points out of the 400 that fall inside the star. The number of affected points decreases rapidly in the angular direction, so that the discontinuity is completely smoothed out within a few angular grid points.

To verify that the discontinuities described above are not numerical artifacts, we performed a series of independent tests. First, we compared our one-fluid configurations directly against the equilibrium models reported by [258] in Table 6, which we treat as reference solutions.

Figure 5.9 summarizes the relative differences between the two sets of results, showing that our models reproduce their data with high accuracy: the gravitational mass differs by at most $\sim 1.3\%$ for configurations with $(\lambda_1, \lambda_2) = (1.6, 1)$, while the equatorial radius and the quantities related to the angular velocity, including the central, equatorial, and maximum values, agree to within 0.4%. This error on the mass can be traced back to differences in the implementation of the EOS, rather than to the numerical method itself. Direct comparison of the full angular velocity profiles on the equatorial plane with those shown in Fig. 12 of [258] confirms the agreement, with discrepancies well below 1%. Importantly, in all of these benchmark cases, our solutions for $\Omega(r)$ are continuous across the stellar interior, demonstrating that the observed discontinuities at high central energy densities and high angular momentum are not intrinsic to the numerical implementation.

We also increased the grid resolution in both the radial and angular directions, from (800, 400) to (1600, 800), and tightened the convergence tolerance from 10^{-9} to 10^{-12} (global quantities such as the gravitational mass already converge at the level of 10^{-7}). Root finding within the algorithm was maintained at machine accuracy. At high resolution, small oscillatory features arise near the stellar surface due to the

steep decrease of matter variables. They can however be removed by switching the interpolation scheme from cubic to linear.

The location and extent of the discontinuous radial interval remain unchanged within numerical error.

Together, these tests indicate that the discontinuities are not due to insufficient resolution or implementation errors, but rather reflect the absence of a real solution for Ω over the affected interval.

5.4 Conclusions

In this work, we have studied DM-admixed NSs in the regime of differential rotation, which is of particular relevance for post-merger remnants of BNS coalescences. Building upon our earlier extension of the `RNS` code to two fluids, we have now implemented differential rotation laws that capture the angular velocity distributions observed in numerical relativity simulations of hypermassive NSs. In our framework, BM and DM are treated as two cold, gravitationally coupled fluids, with the baryonic component following differential rotation and the DM rotating quasi-uniformly, consistent with expectations from core-type configurations.

We considered sequences with fixed DM mass fractions up to 5%, focusing on two representative choices of the rotation law parameters: $(\lambda_1, \lambda_2) = (2, 0.5)$, which admits toroidal (Type C) configurations, and $(1.8, 1)$, which yields quasi-spherical (Type A) equilibria. In both cases, the BM angular velocity reaches maximum away from the center, while the DM part rotates uniformly in accordance with numerical relativity merger simulations. Note that we focus only on the core DM configuration, i.e., when the DM component is roughly speaking confined inside the star. The reason is that halo configurations lead to a more complicated post-merger angular velocity distribution [262].

We investigated how the inclusion of a dark component modifies the maximum mass, stability, and structural properties of the remnant. Our results confirm that a centrally concentrated DM core generally reduces the maximum mass, as the additional gravitational pull is not compensated by extra pressure support. However,

rotation tends to mitigate this reduction, and for sufficiently high total angular momentum the maximum masses of admixed stars approach those of their pure baryonic counterparts.

The scaling of the maximum mass with total angular momentum can be captured with high accuracy by a Padé resummation of the Hartle-Thorne expansion. This indicates that, despite the increased complexity of the two-fluid system, the global impact of a differential rotation remains predictable in terms of a small set of effective parameters. At the same time, the details of the angular velocity profile, and in particular the interplay between the two fluids, introduce new qualitative effects: we observe the emergence of a local minimum in the baryonic angular velocity profile, a feature absent in the corresponding one-fluid models. This effect arises from the redistribution of the gravitational potential by the dark component.

The limitations of the present analysis are primarily numerical: configurations with large DM angular momentum fractions or extreme deformations remain challenging to construct within the current `RNS` framework. Nevertheless, the results confirm that the combination of differential rotation and a dark component produces imprints in equilibrium sequences and stability boundaries, with potential consequences for the interpretation of post-merger GW signals. However, equilibrium sequences alone are not sufficient to disentangle DM admixture from a simple softening of the baryonic EOS, since both scenarios lead to similar modifications in the mass-radius-moment of inertia plane.

Finally, we find that for large angular-momentum fractions, the central energy density, the numerical scheme approaches its limits; in particular, some quasi-spherical models exhibit discontinuities in $\Omega(r)$ where the adopted rotation law ceases to admit a real solution. Perhaps this is a residual of the employed differential rotation law and theory parameter. Thus, further investigation is needed, which is out of the scope of the present paper.

Finally, it is important to address the thermodynamic assumptions adopted in this study. The equilibrium models presented here rely on a zero-temperature baryonic equation of state. In realistic binary neutron star merger scenarios, shock heating raises the temperature of the remnant to tens of MeV on dynamical timescales,

while neutrino cooling operates on significantly longer timescales ($\sim$ seconds). Consequently, differentially rotating remnants are physically hot objects supported by both rotation and thermal pressure. The inclusion of finite-temperature effects would effectively stiffen the equation of state, yielding higher maximum masses and larger radii. In this regard, the cold models presented in this work represents a conservative approximation: since thermal support provides additional stability against collapse, configurations that are stable in the cold limit are expected to remain stable when thermal effects are included. Moreover, the qualitative impact of the dark matter component persists independently of the thermal state of the baryonic fluid.

Future work can expand in several directions. First, the inclusion of halo-type configurations, which require more general rotation laws than currently available, would allow a broader survey of possibilities. Second, the dependence of our results on the DM microphysics, i.e., particle mass and self-interaction strength, remains to be mapped in detail, with the prospect of constraining regions of the parameter space through astrophysical observations. Finally, the equilibrium sequences constructed here can serve as initial data for full numerical relativity simulations of DM-admixed merger remnants.

The equilibrium sequences studies provide a link between microphysical modeling and astrophysical observables in multimessenger astronomy. They allow for a systematic exploration of a very large parameter space covering DM properties, baryonic equations of state, and rotation laws, at a fraction of the computational cost of full dynamical simulations. The description of post-merger remnants as quasi-equilibrium models has already proven valuable in several contexts: interpreting the post-merger GW spectrum, determining the threshold mass to prompt collapse, constructing empirical relations that connect remnant properties to those of nonrotating models, and modeling longer-timescale processes relevant for multimessenger follow-up of GW detections [51, 252, 289–292]. In this sense, the equilibrium sequences developed here provide theoretical insight into the role of DM and represent a practical framework for connecting microscopic physics to future multimessenger observations.

Conclusions and Outlook

This work presented a systematic study of compact objects containing a dark matter component, building a bridge between three regimes: pure dark stars composed entirely of a self-interacting bosonic fluid, mixed configurations in which baryonic and dark matter coexist, and rapidly rotating or differentially rotating equilibria that reproduce the physical conditions expected in the aftermath of binary mergers. The results provide a unified framework to describe how small amounts dark matter can affect the macroscopic structure and the rotational behaviour of neutron stars.

The first part of the thesis established the physical background necessary to interpret these configurations. Neutron stars were described as relativistic stellar objects sustained by the pressure of degenerate nuclear matter against gravitational collapse. Their equilibrium structure follows from the Einstein equations under the assumptions of stationarity and axisymmetry. The Tolman-Oppenheimer-Volkoff equations describes the balance of gravity and internal pressure in the static limit; the Komatsu-Eriguchi-Hachisu scheme extends the description to rotating stars by solving the metric potentials in quasi-isotropic coordinates. The equation of state plays a fundamental role in connecting the local thermodynamic variables to macroscopic observables such as mass, radius, and moment of inertia. Different nuclear models were used to span the range of realistic stiffness compatible with current observations.

The second element considered was the modelling of dark matter as a bosonic condensate described by a self-interacting scalar field in the mean-field limit. In this regime, the pressure and energy density follow a polytropic relation determined by the particle mass and quartic self-coupling. These parameters can be mapped to an effective equation of state similar to that of a nonrelativistic fluid with a stiffening term from the repulsive interaction. When coupled only through gravity to the

baryonic component, this form of dark matter can coexist with ordinary matter inside a single compact configuration. The dark matter can either form a small core surrounded by baryons or dominate the structure entirely, depending on the relative central densities.

The first family of models studied were pure dark stars. By integrating the Einstein equations for a single bosonic fluid with quartic self-interaction, a complete sequence of equilibrium configurations was obtained. The mass and radius follow universal scaling relations that depend on the ratio $\sqrt{\lambda}/m_{\mathrm{DM}}^2$, linking microscopic parameters to astrophysical observables. The results confirm that self-interactions are essential to produce stellar-scale objects, while free bosons would lead to configurations of microscopic size. The computed tidal deformabilities suggest that, in principle, mergers of such objects could generate gravitational wave signatures within the sensitivity of future detectors. These findings demonstrate that self-interacting bosonic matter can sustain compact equilibrium states in the same mass range as neutron stars, providing a reference baseline for the mixed cases.

The second group of results focused on dark matter-admixed neutron stars under uniform rotation. The public code RNS was extended to describe two fluids coupled only by gravity, each characterized by its own equation of state, enthalpy distribution, and rotation law. The implementation required the generalization of the hydrostationary equilibrium relations and the simultaneous solution of the Einstein equations for the total stress-energy tensor. Extensive numerical testing verified that the modified code reproduces the known one-fluid solutions with high accuracy; the relative error remained below one percent.

With this framework in place, equilibrium sequences were constructed for different dark matter fractions and angular momentum distributions. The results reveal that even a small dark matter core, representing a few percent of the total mass, changes the stellar properties in a measurable way. The maximum mass, the moment of inertia, and the mass-radius relation shift depending on the relative concentration of the dark and baryonic components. The trends mimic the effects of varying the stiffness of the baryonic equation of state, producing degeneracies between nuclear physics and dark matter parameters. These findings highlight that the interpreta-

tion of observational constraints on the dense matter equation of state must take into account possible dark matter contributions. Co-rotating and counter-rotating configurations were explored, showing that the total angular momentum can be distributed nontrivially between the two fluids without compromising equilibrium.

The final stage of the investigation introduced differential rotation, a key feature of the transient remnants formed in binary mergers. To describe this regime, the code was extended further to include a generalized rotation law based on the parametrization proposed by Uryū and collaborators [53]. This law captures the transition from a uniformly rotating core to a more rapidly rotating outer envelope and reproduces the behaviour observed in hydrodynamical simulations. Differential rotation allows the star to support masses significantly above the uniform rotation limit, providing a realistic description of hypermassive remnants. The presence of a dark matter core modifies the stability threshold and the internal angular velocity profile, affecting the transition between stable and unstable configurations.

A detailed numerical analysis was performed to identify the regions of parameter space where the solutions remain physically consistent. For certain combinations of the differential rotation parameters, the angular velocity profile develops discontinuities at high central energy densities. The comparison with published one-fluid results confirmed that the behaviour arises from the intrinsic structure of the rotation law rather than numerical artifacts. The consistency checks, including grid refinement and tolerance tests, ensured that the results are robust at the level of numerical precision required by relativistic stellar modelling.

The combined outcomes of the three projects draw a picture of the role of dark matter in compact objects. The self-interacting bosonic model provides a minimal yet flexible description that can reproduce dark matter-admixed configurations and allows for isolated dark stars. In the two-fluid regime, the gravitational coupling alone is sufficient to produce stable equilibrium states where dark and baryonic matter coexist. The relative contribution of each component determines the global observables that could be tested by future missions. The introduction of rotation, both uniform and differential, reveals that the influence of dark matter extends beyond static structure to the dynamical and stability properties of compact stars. From an

astrophysical standpoint, the results imply that dark matter can act as an effective parameter degeneracy in the interpretation of observational data. Measurements of mass, radius, or moment of inertia from pulsars and X-ray sources can be reproduced by either changing the baryonic equation of state or adding a small dark matter core. Similarly, gravitational wave observations constrain combinations of parameters that depend jointly on nuclear physics and dark matter microphysics. Breaking these degeneracies will require both multimessenger measurements and consistent theoretical modelling.

Several extensions are natural. The numerical scheme can incorporate dark matter halos extending beyond the baryonic surface, a scenario relevant for slow accretion during the star's lifetime. The inclusion of temperature and finite-entropy effects would allow applications to protoneutron stars and merger remnants. The exploration of the parameter space in terms of dark matter particle mass, self-coupling, and fraction will enable direct comparison with cosmological and particle physics constraints. Finally, the equilibrium models generated by the two-fluid RNS code can be used as starting points for dynamical evolutions in numerical relativity, connecting the equilibrium theory to time-dependent simulations.

Appendix A

The KEH scheme

In this appendix, we will explore an iterative numerical method aimed at solving an integral representation of the field equations Eqs. (1.44) to (1.47), as originally developed by Komatsu, Eriguchi, and Hachisu [40] and later extended with the modifications included by Cook, Shapiro, and Teukolsky [43–45].

First, we will present how the metric equations can be rewritten using Green's functions in an integral formulation that naturally enforces the correct boundary conditions, and then describe the iterative procedure that transforms spherically symmetric configurations into rapidly rotating solutions.

The KEH scheme The first step is to rewrite the metric element Eq. (1.40) into a form that yields elliptic equations suitable for inversion via the Green's functions method. Defining

$$\gamma = \ln B\,, \tag{A.1}$$

$$\rho = 2\nu - \ln B\,, \tag{A.2}$$

we obtain

$$\mathrm{d}s^2 = -\,\mathrm{e}^{\gamma+\rho}\mathrm{d}t^2 + \,\mathrm{e}^{\gamma-\rho}r^2\sin^2\theta\,(\mathrm{d}\phi - \omega\mathrm{d}t)^2 + \,\mathrm{e}^{2\alpha}\left(\mathrm{d}r^2 + r^2\mathrm{d}\theta^2\right) \tag{A.3}$$

From now on, ρ will always refer to the metric function defined in Eq. (A.2), and not to the rest-mass density, unless explicitly stated.

Under this new gauge choice and defining $\mu = \cos\theta$, the field equations Eqs. (1.44)

to (1.46) for the metric functions become

$$\Delta\left(\rho\ \mathrm{e}^{\gamma/2}\right) = S_\rho\,, \tag{A.4}$$

$$\left(\Delta + \frac{1}{r}\frac{\partial}{\partial_r} - \frac{1}{r^2}\mu\frac{\partial}{\partial\mu}\right)\gamma\ \mathrm{e}^{\gamma/2} = S_\gamma\,, \tag{A.5}$$

$$\left(\Delta + \frac{2}{r}\frac{\partial}{\partial_r} - \frac{2}{r^2}\mu\frac{\partial}{\partial\mu}\right)\omega\ \mathrm{e}^{(\gamma-2\rho)/2} = S_\omega \tag{A.6}$$

with Δ the Laplacian operator in spherical coordinates and

$$\begin{aligned} S_\rho(r,\mu) = \mathrm{e}^{\frac{\gamma}{2}}\Bigg\{ & 8\pi\,\mathrm{e}^{2\alpha}\sum_i (\varepsilon_i + P_i)\,\frac{1+v_i^2}{1-v_i^2} + \frac{\partial_r\gamma}{r} - \frac{\mu\partial_\mu\gamma}{r^2} + \\ & r^2(1-\mu^2)\,\mathrm{e}^{-2\rho}\left[(\partial_r\omega)^2 + \frac{(1-\mu^2)(\partial_\mu\omega)^2}{r^2}\right] + \\ & \frac{\rho}{2}\left[16\pi\,\mathrm{e}^{2\alpha}\sum_i P_i - \partial_r\gamma\left(\frac{\partial_r\gamma}{2}+\frac{1}{r}\right) - \frac{\partial_\mu\gamma}{r^2}\left(\frac{\partial_\mu\gamma(1-\mu^2)}{2} - \mu\right)\right]\Bigg\}\,, \end{aligned} \tag{A.7}$$

$$S_\gamma(r,\mu) = \mathrm{e}^{\frac{\gamma}{2}}\left\{16\pi\,\mathrm{e}^{2\alpha}\sum_i P_i + \frac{\gamma}{2}\left[16\pi\,\mathrm{e}^{2\alpha}\sum_i P_i - \frac{(\partial_r\gamma)^2}{2} - \frac{(1-\mu^2)(\partial_\mu\gamma)^2}{2r^2}\right]\right\}, \tag{A.8}$$

$$\begin{aligned} S_\omega(r,\mu) = \mathrm{e}^{\frac{\gamma-2\rho}{2}}\Bigg\{ & -16\pi\,\mathrm{e}^{2\alpha}\sum_i \frac{(\Omega_i-\omega)(\varepsilon_i+P_i)}{1-v_i^2} + \omega\left[\frac{\mu}{r^2}\left(2\partial_\mu\rho + \frac{\partial_\mu\gamma}{2}\right)\right. \\ & - 8\pi\,\mathrm{e}^{2\alpha}\sum_i \frac{(1+v_i^2)\varepsilon_i + 2v_i^2 P_i}{1-v_i^2} - \frac{1}{r}\left(2\partial_r\rho + \frac{\partial_r\gamma}{2}\right) \\ & + \frac{1}{4}\left[4(\partial_r\rho)^2 - (\partial_r\gamma)^2\right] + \frac{1-\mu^2}{4r^2}\left[4(\partial_\mu\rho)^2 - (\partial_\mu\gamma)^2\right] \\ & \left. -r^2(1-\mu^2)\,\mathrm{e}^{-2\rho}\left((\partial_r\omega)^2 + \frac{1-\mu^2}{r^2}(\partial_\mu\omega)^2\right)\right]\Bigg\}\,. \end{aligned} \tag{A.9}$$

Lastly, the field equation for the field α (*cf. Eq.* (1.47)) becomes

$$\begin{aligned}
\partial_\mu\alpha = &-\frac{1}{2}(\partial_\mu\rho+\partial_\mu\gamma) - \left\{\left(1-\mu^2\right)\left(1+r\partial_r\gamma\right)^2 + \left[\mu-\left(1-\mu^2\right)\partial_\mu\gamma\right]^2\right\}^{-1} \\
&\times\left[\!\!\left[\frac{1}{2}\left\{r^2\left[\partial_r^2\gamma+\left(\partial_r\gamma\right)^2\right]-\left(1-\mu^2\right)\left[\partial_\mu^2\gamma+\left(\partial_\mu\gamma\right)^2\right]\right\}\left[\left(1-\mu^2\right)\partial_\mu\gamma\right]\right.\right. \\
&+r\partial_r\gamma\left[\frac{\mu}{2}+\mu r\partial_r\gamma+\frac{1-\mu^2}{2}\partial_\mu\gamma\right]+\frac{3}{2}\partial_\mu\gamma\left[\mu\left(1-\mu^2\right)\partial_\mu\gamma\right] \\
&-r\left(1-\mu^2\right)\left(\partial_r\partial_\mu\gamma+\partial_r\gamma\partial_\mu\gamma\right)\left(1+r\partial_r\gamma\right)-\frac{1}{4}\mu r^2\left(\partial_r\rho+\partial_r\gamma\right)^2 \\
&-\frac{r}{2}\left(1-\mu^2\right)\left(\partial_r\rho+\partial_r\gamma\right)\left(\partial_\mu\rho+\partial_\mu\gamma\right)+\frac{1}{4}\mu\left(1-\mu^2\right)\left(\partial_\mu\rho+\partial_\mu\gamma\right)^2 \\
&-\frac{r^2}{2}\left(1-\mu^2\right)\partial_r\gamma\left(\partial_r\rho+\partial_r\gamma\right)\left(\partial_\mu\rho+\partial_\mu\gamma\right) \\
&+\frac{1}{4}\left(1-\mu^2\right)\partial_\mu\gamma\left[r^2\left(\partial_r\rho+\partial_r\gamma\right)^2-\left(1-\mu^2\right)\left(\partial_\mu\rho+\partial_\mu\gamma\right)^2\right] \\
&+\left(1-\mu^2\right)\mathrm{e}^{-2\rho}\left\{\frac{1}{4}r^4\mu\left(\partial_r\omega\right)^2+\frac{1}{2}r^3\left(1-\mu^2\right)\partial_r\omega\partial_\mu\omega-\frac{1}{4}r^2\mu\left(1-\mu^2\right)\left(\partial_\mu\omega\right)^2\right. \\
&\left.\left.\left.+\frac{1}{2}r^4\left(1-\mu^2\right)\partial_r\gamma\partial_r\omega\partial_\mu\omega-\frac{1}{4}r^2\left(1-\mu^2\right)\partial_\mu\gamma\left[r^2\left(\partial_r\omega\right)^2-\left(1-\mu^2\right)\left(\partial_\mu\omega\right)^2\right]\right\}\right]\!\!\right]
\end{aligned} \tag{A.10}$$

supplemented by the spatial flatness condition $\alpha(\mu=1)=(\gamma-\rho)/2$ as the initial condition for each line of constant r.

While Eq. (A.10) can be solved with standard integration techniques despite its complex functional form, Eqs. (A.4) to (A.6) must be cast into integral equations using the Green's functions of the flat-space, 3-dimensional Laplacian in spherical polar coordinates. We obtain:

$$\rho = -\,\mathrm{e}^{-\gamma/2}\int_0^\infty \mathrm{d}\tilde{r}\int_0^1 \mathrm{d}\mu\,\tilde{r}^2\frac{S_\rho\left(\tilde{r},\,\mu\right)}{|\mathbf{r}-\tilde{\boldsymbol{r}}|}, \tag{A.11}$$

$$\omega = -\,\frac{\mathrm{e}^{(2\rho-\gamma)/2}}{2\pi r\sin\theta\cos\phi}\int_0^\infty \mathrm{d}\tilde{r}\int_0^1 \mathrm{d}\mu\sqrt{1-\mu^2}\int_0^{2\pi}\mathrm{d}\phi\,\tilde{r}^3\cos\phi\frac{S_\omega\left(\tilde{r},\,\mu\right)}{|\mathbf{r}-\tilde{\boldsymbol{r}}|}, \tag{A.12}$$

$$\gamma = \frac{2\,\mathrm{e}^{-\gamma/2}}{\pi r\sin\theta}\int_0^\infty \mathrm{d}\tilde{r}\int_0^1 \mathrm{d}\mu\,\tilde{r}^2 S_\gamma\left(\tilde{r},\,\mu\right)\log|\mathbf{r}-\tilde{\boldsymbol{r}}|. \tag{A.13}$$

Finally, the integrals are evaluated using the standard expansion of the Green's functions in angular harmonics

$$\log|\mathbf{r}-\tilde{\boldsymbol{r}}| = -\sum_{n=1}^{\infty}\frac{1}{n}\frac{r_{\rm min}^n}{r_{\rm max}^n}\left(\cos n\theta\cos n\tilde{\theta}+\sin n\theta\sin n\tilde{\theta}\right)+\log r_{\rm max}, \tag{A.14}$$

$$\begin{aligned}\frac{1}{|\mathbf{r}-\tilde{\boldsymbol{r}}|} = &\sum_{n=0}^{\infty}\frac{r_{\rm min}^n}{r_{\rm max}^{n+1}}\Bigg[P_n(\cos\theta)\,P_n(\cos\tilde{\theta})\\ &+2\sum_{m=1}^{n}\frac{(n-m)!}{(n+m)!}P_n^m(\cos\theta)P_n^m(\cos\tilde{\theta})\cos m\left(\phi-\tilde{\phi}\right)\Bigg],\end{aligned} \tag{A.15}$$

where $r_{\rm min}=\min(r,\tilde{r})$, $r_{\rm max}=\max(r,\tilde{r})$, $P_n(\cos\theta)$ are the Legendre polynomials and lastly $P_n^m(\cos\theta)$ are the associated Legendre polynomials.

One last possible improvement that can be considered to facilitate the numerical integration of Eqs. (A.11) to (A.13) is a compactification of the radial variable r [43]. Instead of truncating the domain at some finite radius, we define a new variable

$$s=\frac{r}{r+r_e} \tag{A.16}$$

such that $s=0$ when $r=0$, $s\to 1$ as $r\to\infty$, and $s=\frac{1}{2}$ when $r=r_e$, where r_e is chosen as a characteristic length scale of the problem (in practice, the quasi-isotropic equatorial radius of the star). In this way, the infinite radial domain is mapped smoothly onto the finite interval $s\in[0,1]$. All field equations must then be reformulated in terms of s, but the structure of the integral representation remains unchanged.

The RNS code We now have all the theoretical tools necessary to describe the iterative procedure that enables the construction of rotating neutron star models.

A solution is characterized by at least two parameters (for each fluid considered): one related to the compactness of the system and one to the degree of rotation. A particularly robust choice is the central energy density ε_c^i and the ratio of the polar to equatorial radius r_p^i/r_e^i; $i=1,\cdots,N$ identifies the fluid. Differential rotation

introduces additional parameters, the number of which depends on the functional form of the rotation law (see Section 1.3). Alternatively, other physical quantities like the total mass, fluid fractions $f_i = M_i / \sum_j M_j$ or angular velocity can be specified. However, these models are computed iteratively by adjusting the appropriate fundamental parameter until a configuration is found within a specified tolerance. The relative error in determining these parameters is freely specifiable and set to 10^{-3} by default. The general algorithm used goes as follows.

- Initial conditions are computed solving the TOV equations Eqs. (1.17) and (1.18) for some central energy densities ε_c^i, taken as first guesses.
- The free parameters ε_c^i, r_{ratio}^i can either be given as input or fixed with the required nested root finding loops to achieve some desired property of the computed system. For instance, in the two fluid case with $i = \{\text{BM, DM}\}$, $\varepsilon_c^{\text{BM}}$ is changed to find constant total mass sequences, $\varepsilon_c^{\text{DM}}$ to fix the dark matter fraction, and $r_{\text{ratio}}^{\text{BM}}$ and $r_{\text{ratio}}^{\text{DM}}$ allow us to achieve the target angular velocity for the respective fluid. For each iteration of the innermost root finding, the equilibrium equations are solved and the properties of the system computed.
- Once convergence is achieved, the final model with desired parameters is recomputed, and key stellar properties, including mass, radius, and angular momentum, are calculated.

It is worth mentioning that algorithms for finding roots in multidimensional spaces do exist, but their implementation here is not straightforward. Instead, the algorithm described navigates the parameter space in small, incremental steps. This approach ensures that the initial guess is sufficiently close to the solution, guaranteeing convergence. More sophisticated methods, such as Broyden's algorithm [300], are available but typically involve larger steps through the parameter space, at least in the beginning. These larger steps often result in failures when solving the equilibrium equations, making them less reliable in this context.

Finally, the essential features of the algorithm to solve the equilibrium equations

in the case of a single fluid (the generalization to the multifluid system is straightforward) are summarized as follows:

1. The procedure begins with an initial guess for the metric and matter fields, taken either from a previously computed rotating solution or from a nonrotating solution of the TOV equations Eqs. (1.17) and (1.18).

2. The metric potentials are rescaled: ρ, γ, and α are multiplied by r_e^{-2}, while ω and Ω by r_e.

3. A new value of r_e is computed. Two approaches are possible, depending on the number of fluids considered. In the one-fluid case, r_e is obtained by inverting the relation obtained equating the first integral of hydrostationary equilibrium Eq. (1.57) at the centre and at the pole; in the multi-fluid case, a fixed-point iteration is used:

$$r_e^{\text{new}} = r_e \frac{2\left(h_{\text{centre}} - h_{\text{pole}}\right)}{\gamma_{\text{pole}} + \rho_{\text{pole}} - \gamma_{\text{centre}} - \rho_{\text{centre}}}. \tag{A.17}$$

   Here, the right-hand side is evaluated using the fields from the previous iteration (or the initial guess).

4. The parameters that characterise the rotation law are now updated, if necessary. To do so, we express them in terms of auxiliary quantities that prescribe the ratios of angular velocities at specific points in the star. For example, both the rotation laws presented in Section 1.3 [53] are determined by two parameters, A and B, which can be fixed by solving the system

$$\begin{cases} \lambda_1 = & \frac{\Omega_e(j_e;A,B)}{\Omega_c}, \\ \lambda_2 = & \frac{\Omega_{\max}(j_{\max};A,B)}{\Omega_c}, \end{cases} \tag{A.18}$$

   where the angular momentum is computed explicitly from the definition

$$j = u^t u_\phi = \frac{(\Omega - \omega)\, r^2 \sin^2\theta\, \mathrm{e}^{-2\rho}}{1 - (\Omega - \omega)^2\, r^2 \sin^2\theta\, \mathrm{e}^{-2\rho}} \tag{A.19}$$

This choice allows us to target specific angular velocity configurations to mimic, for example, numerical relativity simulations.

5. The angular velocity distribution is updated, starting from its equatorial value Ω_e, obtained by solving numerically the nonlinear equation given by the first integral of hydrostationary equilibrium at the equator minus that at the pole. In the case of Eq. (1.59) with $(p,\, q) = (1,\, 3)$, for example, the equation reads

$$\begin{aligned}&(\gamma_e + \rho_e - \gamma_p - \rho_p) + \ln\left[1 - (\Omega_e - \omega_e)^2\, r_e^2\, \mathrm{e}^{-2\rho_e}\right] = -2 j_e \Omega_e + \\ &\frac{A^2\Omega_e^2}{2\lambda_2^2}\left\{2\frac{A^2}{B^2}\arctan\left(\frac{j_e^2\lambda_2^2}{A^4\Omega_e^2}\right) - \sqrt{2}\left[\arctan\left(1 - \frac{j_e\sqrt{2}\lambda_2}{A^2\Omega_e}\right) - \right.\right. \\ &\left.\left.\arctan\left(1 + \frac{j_e\sqrt{2}\lambda_2}{A^2\Omega_e}\right)\right] + \sqrt{2}\,\mathrm{arctanh}\left(\frac{A^2\Omega_e j_e\sqrt{2}}{\lambda_2\,(j_e^2 + A^4\Omega_e^2/\lambda_2^2)}\right)\right\}\end{aligned} \tag{A.20}$$

Knowing Ω_e provides a new estimate for the angular velocity at the centre, $\Omega_c = \Omega_e/\lambda_2$. At this point, by solving the root-finding problem for the specific rotation law $\Omega(s,\mu) = j(\Omega(s,\mu))$ given by Eq. (1.59) or Eq. (1.60) we determine the field everywhere else.

6. From Ω, the 3-velocity $v = (\Omega - \omega)\, r \sin\theta \exp(-\rho)$ is computed, and the enthalpy is updated. The enthalpy is then converted into energy density and pressure via the equation of state.

7. The updated matter fields are used to recompute the metric fields ρ, γ, ω, and α, which are then rescaled with the appropriate power of r_e.

8. Convergence is monitored by tracking the change in equatorial radius between iterations. If the relative change falls below a chosen threshold, set to 10^{-10} by default, the iterative procedure terminates; otherwise, the algorithm restarts from Step 2.

A number of numerical techniques are employed in order to improve the convergence of this algorithm.

First, Step 5 requires solving a root-finding problem at each grid point inside the star, which is computationally expensive. Several optimizations are applied: for each (s_i, μ_j) point on the grid, a line search is performed starting slightly above the maximum value of Ω from the previous iteration and decreasing down to zero; the function $f(\Omega) = \Omega - j(\Omega)$ is evaluated on the grid until a sign change is detected; once this interval is bracketed, the root is refined using the Brent method. To minimize the number of function evaluations during the line search and to take advantage of the rapid convergence of the Brent method, the initial search is carried out with a coarse step size; if no sign change is found, as may occur in extreme models, the step size is reduced by a factor of 10, up to four successive times. Since the Ω profile can become very steep in the radial direction, the previous value of the field is not employed as a starting value in the search because a fixed or percentage increment misses in many models the correct root, producing an unphysical rotational profile.

Second, successive over-relaxation is employed to update the metric fields according to

$$\Phi_{ij}^{(n+1)} = \Phi_{ij}^{(n)} + c_f, \left(\Phi_{ij}^{\text{new}} - \Phi_{ij}^{(n)} \right), \tag{A.21}$$

where $\Phi_{ij}^{(n)} = \Phi^{(n)}(s_i, \mu_j)$ denotes the value of one generic metric field at a given grid point at the n-th iteration, and Φ_{ij}^{new} is the value of the field computed in the current iteration. The relaxation factor is typically set to $c_f = 0.5$ for all rotating models, and if convergence stalls, it is lowered automatically; a smaller c_f also leads to smaller changes in the equatorial radius between consecutive iterations, so care must be taken to ensure that lowering c_f does not mistakenly flag the model as already converged.

Third, Gibbs error is present at the surface of the star due to the steep gradients of matter fields. While this problem could be solved with the use of surface-adaptive grid coordinates, it is minimized by setting an upper limit to the grid size to SDIV $\times$ MDIV $= 801 \times 401$, respectively in the s and μ direction.

Finally, the choice of $\mu = \cos\theta$ causes some terms in the field equations to be sensitive to division by small numbers, so in the angular derivative spurious oscillations arise near the rotation axis that are purely numerical in origin. Moreover, there

appears an oscillatory behaviour in the α field when the second radial derivatives are computed using second order accurate formulae: this is smoothed by simply using twice the grid spacing to compute them, and it is shown to improve accuracy up to 2% in the equilibrium properties and minimize Hamiltonian constraint violations [31].

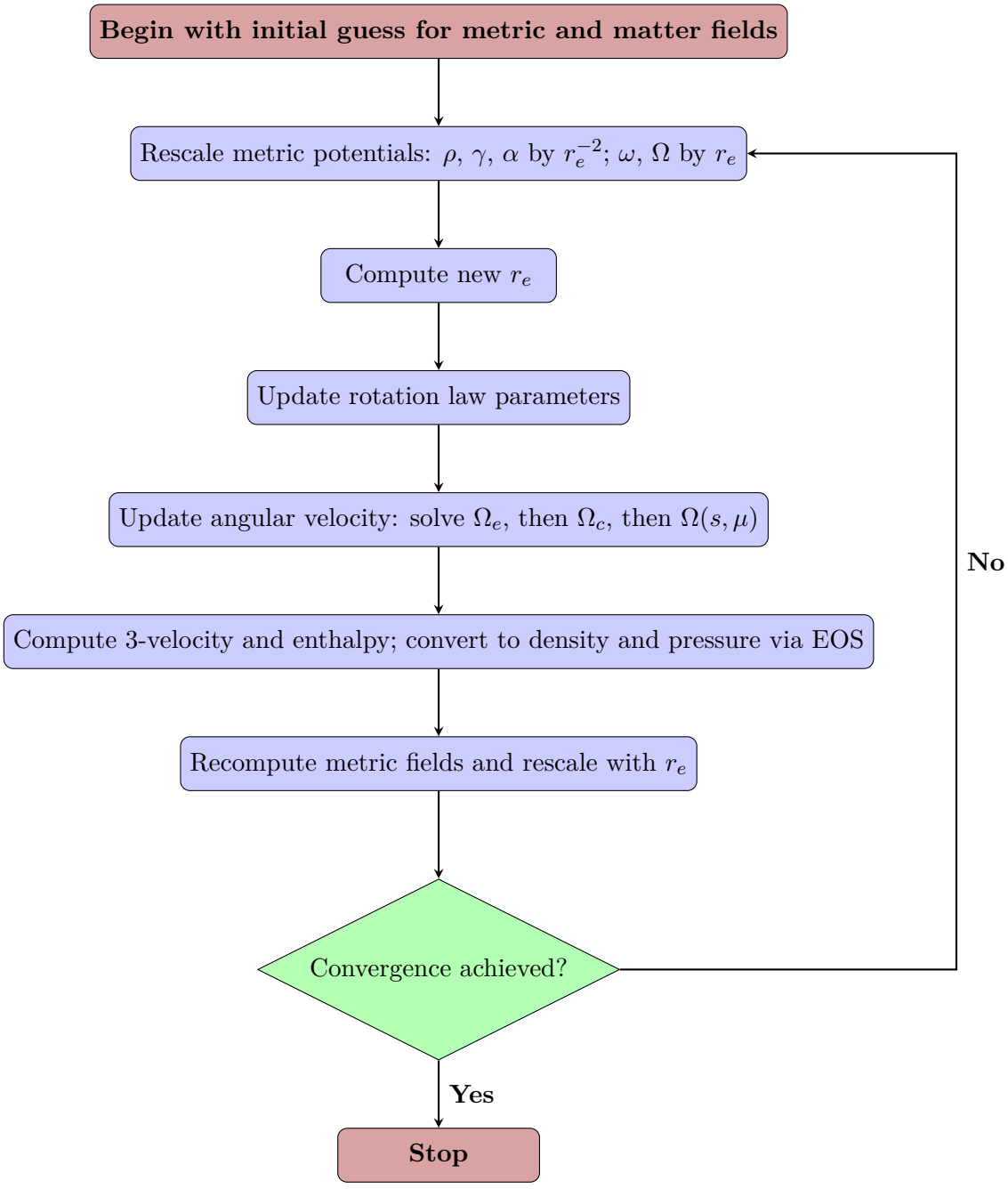

Figure A.1: Iteration scheme for equilibrium solution

Bibliography

[1] B. P. Abbott et al. "GW170817: Observation of Gravitational Waves from a Binary Neutron Star Inspiral". In: *Phys. Rev. Lett.* 119.16 (2017), p. 161101. DOI: 10.1103/PhysRevLett.119.161101.

[2] B. P. Abbott et al. "GW170817: Measurements of neutron star radii and equation of state". In: *Phys. Rev. Lett.* 121.16 (2018), p. 161101. DOI: 10.1103/PhysRevLett.121.161101.

[3] M. Oertel et al. "Equations of state for super11ae and compact stars". In: *Rev. Mod. Phys.* 89 (1 Mar. 2017), p. 015007. DOI: 10.1103/RevModPhys.89.015007.

[4] F. Özel and P. Freire. "Masses, Radii, and the Equation of State of Neutron Stars". In: *Ann. Rev. Astron. Astrophys.* 54 (2016), pp. 401–440. DOI: 10.1146/annurev-astro-081915-023322.

[5] I. Tews et al. "Constraining the speed of sound inside neutron stars with chiral effective field theory interactions and observations". In: *Astrophys. J.* 860.2 (2018), p. 149. DOI: 10.3847/1538-4357/aac267.

[6] R. C. Tolman. "Static Solutions of Einstein's Field Equations for Spheres of Fluid". In: *Phys. Rev.* 55 (4 Feb. 1939), pp. 364–373. DOI: 10.1103/PhysRev.55.364.

[7] J. R. Oppenheimer and G. M. Volkoff. "On Massive Neutron Cores". In: *Phys. Rev.* 55 (4 Feb. 1939), pp. 374–381. DOI: 10.1103/PhysRev.55.374.

[8] W. Baade and F. Zwicky. "Remarks on Super-11ae and Cosmic Rays". In: *Phys. Rev.* 46 (1 July 1934), pp. 76–77. DOI: 10.1103/PhysRev.46.76.2.

[9] J. Chadwick. "The existence of a neutron". In: *Proceedings of the Royal Society of London. Series A, Containing Papers of a Mathematical and Physical Character* 136.830 (June 1932), pp. 692–708. DOI: 10.1098/rspa.1932.0112.

[10] A. Heger et al. "How Massive Single Stars End Their Life". In: *The Astrophysical Journal* 591.1 (July 2003), p. 288. DOI: 10.1086/375341.

[11] I. Bombaci. "The maximum mass of a neutron star." In: *Astronomy and Astrophysics* 305 (Jan. 1996), p. 871.

[12] J. M. Lattimer. "Introduction to neutron stars". In: *AIP Conference Proceedings* 1645.1 (Feb. 2015), pp. 61–78. DOI: 10.1063/1.4909560.

[13] E. J. Ferrer et al. "Equation of State of a Dense and Magnetized Fermion System". In: *Phys. Rev. C* 82 (2010), p. 065802. DOI: 10.1103/PhysRevC.82.065802.

[14] V. Dexheimer, R. Negreiros, and S. Schramm. "Hybrid stars in a strong magnetic field". In: *European Physical Journal A* 48.12, 189 (Dec. 2012), p. 189. DOI: 10.1140/epja/i2012-12189-y.

[15] L. Rezzolla et al., eds. "The Physics and Astrophysics of Neutron Stars". Vol. 457. Astrophysics and Space Science Library. Springer, 2018. DOI: 10.1007/978-3-319-97616-7.

[16] D. G. Ravenhall, C. J. Pethick, and J. R. Wilson. "Structure of Matter below Nuclear Saturation Density". In: *Phys. Rev. Lett.* 50 (26 June 1983), pp. 2066–2069. DOI: 10.1103/PhysRevLett.50.2066.

[17] A. Hewish et al. "Observation of a Rapidly Pulsating Radio Source". In: *Nature* 217.5130 (Feb. 1968), pp. 709–713. DOI: 10.1038/217709a0.

[18] M. C. Miller et al. "PSR J0030+0451 Mass and Radius from $NICER$ Data and Implications for the Properties of Neutron Star Matter". In: *Astrophys. J. Lett.* 887.1 (2019), p. L24. DOI: 10.3847/2041-8213/ab50c5.

[19] T. E. Riley et al. "A $NICER$ View of PSR J0030+0451: Millisecond Pulsar Parameter Estimation". In: *Astrophys. J. Lett.* 887.1 (2019), p. L21. DOI: 10.3847/2041-8213/ab481c.

[20] J. L. Friedman, J. R. Ipser, and R. D. Sorkin. "Turning Point Method for Axisymmetric Stability of Rotating Relativistic Stars". In: *The Astrophysical Journal* 325 (Feb. 1988), p. 722. DOI: 10.1086/166043.

[21] J. Antoniadis et al. "A Massive Pulsar in a Compact Relativistic Binary". In: *Science* 340.6131 (2013), p. 1233232. DOI: 10.1126/science.1233232.

[22] R. W. Romani et al. "PSR J1810+1744: Companion Darkening and a Precise High Neutron Star Mass". In: *Astrophys. J. Lett.* 908.2 (2021), p. L46. DOI: 10.3847/2041-8213/abe2b4.

[23] R. W. Romani et al. "PSR J0952−0607: The Fastest and Heaviest Known Galactic Neutron Star". In: *Astrophys. J. Lett.* 934.2 (2022), p. L17. DOI: 10.3847/2041-8213/ac8007.

[24] M. C. Miller et al. "The Radius of PSR J0740+6620 from NICER and XMM-Newton Data". In: *Astrophys. J. Lett.* 918.2 (2021), p. L28. DOI: 10.3847/2041-8213/ac089b.

[25] T. E. Riley et al. "A NICER View of the Massive Pulsar PSR J0740+6620 Informed by Radio Timing and XMM-Newton Spectroscopy". In: *Astrophys. J. Lett.* 918.2 (2021), p. L27. DOI: 10.3847/2041-8213/ac0a81.

[26] D. Choudhury et al. "A NICER View of the Nearest and Brightest Millisecond Pulsar: PSR J0437–4715". In: *Astrophys. J. Lett.* 971.1 (2024), p. L20. DOI: 10.3847/2041-8213/ad5a6f.

[27] K. S. Thorne and A. Campolattaro. "Non-Radial Pulsation of General-Relativistic Stellar Models. I. Analytic Analysis for L >= 2". In: *Astrophysical Journal, vol. 149, p.591* (Sept. 1967), p. 591. DOI: 10.1086/149288.

[28] T. Hinderer. "Tidal Love numbers of neutron stars". In: *Astrophys. J.* 677 (2008). [Erratum: Astrophys.J. 697, 964 (2009)], pp. 1216–1220. DOI: 10.1086/533487.

[29] S. Postnikov, M. Prakash, and J. M. Lattimer. "Tidal Love Numbers of Neutron and Self-Bound Quark Stars". In: *Phys. Rev. D* 82 (2010), p. 024016. DOI: 10.1103/PhysRevD.82.024016.

[30] B. P. Abbott et al. "GW190425: Observation of a Compact Binary Coalescence with Total Mass $\sim 3.4\ M_\odot$". In: *The Astrophysical Journal Letters* 892.1, L3 (Mar. 2020), p. L3. DOI: 10.3847/2041-8213/ab75f5.

[31] J. L. Friedman and N. Stergioulas. "Rotating Relativistic Stars". Cambridge Monographs on Mathematical Physics. Cambridge University Press, 2013.

[32] F. Grippa, G. Lambiase, and T. K. Poddar. "Searching for New Physics in an Ultradense Environment: A Review on Dark Matter Admixed Neutron Stars". In: *Universe* 11.3 (2025). DOI: 10.3390/universe11030074.

[33] S. Typel et al. "Composition and thermodynamics of nuclear matter with light clusters". In: *Phys. Rev. C* 81 (1 Jan. 2010), p. 015803. DOI: 10.1103/PhysRevC.81.015803.

[34] M. Fortin, M. Oertel, and C. Providência. "Hyperons in hot dense matter: what do the constraints tell us for equation of state?" In: *Publ. Astron. Soc. Austral.* 35 (2018), p. 44. DOI: 10.1017/pasa.2018.32.

[35] M. Shahrbaf et al. "Sexaquark dilemma in neutron stars and its solution by quark 12onfinement". In: *Phys. Rev. D* 105.10 (2022), p. 103005. DOI: 10.1103/PhysRevD.105.103005.

[36] V. Sagun et al. "The statistical multifragmentation model for liquid-gas phase transition with a compressible nuclear liquid". In: *Nuclear Physics A* 924 (2014), pp. 24–46. DOI: 10.1016/j.nuclphysa.2013.12.012.

[37] V. Sagun, G. Panotopoulos, and I. Lopes. "Asteroseismology: radial oscillations of neutron stars with realistic equation of state". In: *Phys. Rev. D* 101.6 (2020), p. 063025. DOI: 10.1103/PhysRevD.101.063025.

[38] J. B. Hartle. "Slowly Rotating Relativistic Stars. I. Equations of Structure". In: *The Astrophysical Journal* 150 (Dec. 1967), p. 1005. DOI: 10.1086/149400.

[39] J. B. Hartle and K. S. Thorne. "Slowly Rotating Relativistic Stars. II. Models for Neutron Stars and Supermassive Stars". In: *The Astrophysical Journal* 153 (Sept. 1968), p. 807. DOI: 10.1086/149707.

[40] H. Komatsu, Y. Eriguchi, and I. Hachisu. "Rapidly rotating general relativistic stars. I - Numerical method and its application to uniformly rotating polytropes". In: *Mon. Not. Roy. Astron. Soc.* 237 (1989), pp. 355–379. DOI: 10.1093/mnras/237.2.355.

[41] N. Stergioulas and J. L. Friedman. "Comparing models of rapidly rotating relativistic stars constructed by two numerical methods". In: *Astrophys. J.* 444 (1995), p. 306. DOI: 10.1086/175605.

[42] N. Stergioulas, T. A. Apostolatos, and J. A. Font. "Nonlinear pulsations in differentially rotating neutron stars: Mass - shedding - induced damping and splitting of the fundamental mode". In: *Mon. Not. Roy. Astron. Soc.* 352 (2004), p. 1089. DOI: 10.1111/j.1365-2966.2004.07973.x.

[43] G. B. Cook, S. L. Shapiro, and S. A. Teukolsky. "Spin-up of a Rapidly Rotating Star by Angular Momentum Loss: Effects of General Relativity". In: *The Astrophysical Journal* 398 (Oct. 1992), p. 203. DOI: 10.1086/171849.

[44] G. B. Cook, S. L. Shapiro, and S. A. Teukolsky. "Rapidly Rotating Polytropes in General Relativity". In: *The Astrophysical Journal* 422 (Feb. 1994), p. 227. DOI: 10.1086/173721.

[45] G. B. Cook, S. L. Shapiro, and S. A. Teukolsky. "Rapidly Rotating Neutron Stars in General Relativity: Realistic Equations of State". In: *The Astrophysical Journal* 424 (Apr. 1994), p. 823. DOI: 10.1086/173934.

[46] E. M. Butterworth and J. R. Ipser. "On the structure and stability of rapidly rotating fluid bodies in general relativity. I. The numerical method for computing structure and its application to uniformly rotating homogeneous bodies." In: *The Astrophysical Journal* 204 (Feb. 1976), pp. 200–223. DOI: 10.1086/154163.

[47] J. M. Baarden. "Rapidly rotating stars, disks and black holes". In: *Les Houches Summer School of Theoretical Physics: Black Holes*. 1973, pp. 241–290.

[48] R. H. Boyer and R. W. Lindquist. "A variational principle for a rotating relativistic fluid". In: *Physics Letters* 20.5 (Mar. 1966), pp. 504–506. DOI: 10.1016/0031-9163(66)90975-9.

[49] J. B. Hartle and D. H. Sharp. "Variational Principle for the Equilibrium of a Relativistic, Rotating Star". In: *The Astrophysical Journal* 147 (Jan. 1967), p. 317. DOI: 10.1086/149002.

[50] L. Villain et al. "Evolutionary sequences of rotating protoneutron stars". In: *Astron. Astrophys.* 418 (2004), pp. 283–294. DOI: 10.1051/0004-6361:20035619.

[51] P. Iosif and N. Stergioulas. "Equilibrium sequences of differentially rotating stars with post-merger-like rotational profiles". In: *Mon. Not. Roy. Astron. Soc.* 503.1 (2021), pp. 850–866. DOI: 10.1093/mnras/stab392.

[52] P. Iosif and N. Stergioulas. "Differentially Rotating Relativistic Stars beyond the J-Constant Law". In: *Physical Sciences Forum* 2.1 (2021). DOI: 10.3390/ECU2021-09312.

[53] K. Uryū et al. "Modeling differential rotations of compact stars in equilibriums". In: *Phys. Rev. D* 96 (10 Nov. 2017), p. 103011. DOI: 10.1103/PhysRevD.96.103011.

[54] M. Ansorg, D. Gondek-Rosińska, and L. Villain. "On the solution space of differentially rotating neutron stars in general relativity". In: *Monthly Notices of the Royal Astronomical Society* 396.4 (July 2009), pp. 2359–2366. DOI: 10.1111/j.1365-2966.2009.14904.x.

[55] G. Bertone and D. Hooper. "History of dark matter". In: *Rev. Mod. Phys.* 90 (4 Oct. 2018), p. 045002. DOI: 10.1103/RevModPhys.90.045002.

[56] E. Öpik. "Selective absorption of light in space, and the dynamics of the Universe". In: *Bull. de la Soc. Astr. de Russie* 21.150 (1915), p. 5.

[57] 0. H. Oort. "The force exerted by the stellar system in the direction perpendicular to the galactic plane and some related problems". In: *Bulletin of the Astronomical Institutes of the Netherlands, Vol. 6, p. 249* 6 (1932), p. 249.

[58] F. Zwicky. "Die rotverschiebung von extragalaktischen nebeln". In: *Helvetica Physica Acta, Vol. 6, p. 110-127* 6 (1933), pp. 110–127.

[59] F. Zwicky. "On the Masses of Nebulae and of Clusters of Nebulae". In: *The Astrophysical Journal* 86 (Oct. 1937), p. 217. DOI: 10.1086/143864.

[60] V. C. Rubin and W. K. Ford Jr. "Rotation of the Andromeda Nebula from a Spectroscopic Survey of Emission Regions". In: *The Astrophysical Journal* 159 (Feb. 1970), p. 379. DOI: 10.1086/150317.

[61] D. H. Rogstad and G. S. Shostak. "Gross Properties of Five Scd Galaxies as Determined from 21-CENTIMETER Observations". In: *The Astrophysical Journal* 176 (Sept. 1972), p. 315. DOI: 10.1086/151636.

[62] R. N. Whitehurst and M. S. Roberts. "High-velocity neutral hydrogen in the central region of the andromeda galaxy". In: *Astrophysical Journal, vol. 175, p. 347* 175 (1972), p. 347. DOI: 10.1086/151562.

[63] M. Roberts and A. Rots. "Comparison of rotation curves of different galaxy types". In: *Astronomy and Astrophysics, Vol. 26, p. 483-485 (1973)* 26 (1973), pp. 483–485.

[64] V. C. Rubin, W. K. Ford Jr., and N. Thonnard. "Extended rotation curves of high-luminosity spiral galaxies. IV. Systematic dynamical properties, Sa through Sc". In: *Astrophys. J. Lett.* 225 (1978), pp. L107–L111. DOI: 10.1086/182804.

[65] D. Clowe et al. "A direct empirical proof of the existence of dark matter". In: *Astrophys. J. Lett.* 648 (2006), pp. L109–L113. DOI: 10.1086/508162.

[66] D. Harvey et al. "The non-gravitational interactions of dark matter in colliding galaxy clusters". In: *Science* 347 (2015), pp. 1462–1465. DOI: 10.1126/science.1261381.

[67] G. R. Blumenthal et al. "Formation of Galaxies and Large Scale Structure with Cold Dark Matter". In: *Nature* 311 (1984). Ed. by M. A. Srednicki, pp. 517–525. DOI: 10.1038/311517a0.

[68] D. J. Eisenstein and W. Hu. "Baryonic features in the matter transfer function". In: *The Astrophysical Journal* 496 (1998), p. 605. DOI: 10.1086/305424.

[69] A. Meiksin, M. White, and J. A. Peacock. "Baryonic signatures in large-scale structure". In: *Monthly Notices of the Royal Astronomical Society* 304.4 (Apr. 1999), pp. 851–864. DOI: 10.1046/j.1365-8711.1999.02369.x.

[70] M. Cirelli, A. Strumia, and J. Zupan. "Dark Matter". In: (June 2024).

[71] T. Zimmermann et al. "Dwarf Galaxies Imply Dark Matter is Heavier than 2.2×10-21 eV". In: *Phys. Rev. Lett.* 134.15 (2025), p. 151001. DOI: 10.1103/PhysRevLett.134.151001.

[72] A.-C. Eilers et al. "The Circular Velocity Curve of the Milky Way from 5 to 25 kpc". In: *The Astrophysical Journal* 871.1, 120 (Jan. 2019), p. 120. DOI: 10.3847/1538-4357/aaf648.

[73] Y. B. Zel'dovich and I. D. Novikov. "The Hypothesis of Cores Retarded during Expansion and the Hot Cosmological Model". In: *Sov. Astron.* 10 (1967), p. 602.

[74] S. Hawking. "Gravitationally Collapsed Objects of Very Low Mass". In: *Monthly Notices of the Royal Astronomical Society* 152.1 (Apr. 1971), pp. 75–78. DOI: 10.1093/mnras/152.1.75.

[75] "Fourth order supergravity S. Theisen, Nucl. Phys. B263 (1986) 687". In: *Nuclear Physics B* 269.3 (June 1986), pp. 744–744. DOI: 10.1016/0550-3213(86)90519-5.

[76] E. Witten. "Cosmic 09aration of Phases". In: *Phys.Rev.* D30 (1984), pp. 272–285. DOI: 10.1103/PhysRevD.30.272.

[77] A. De Rujula and S. L. Glashow. "Nuclearites: A Novel Form of Cosmic Radiation". In: *Nature* 312 (1984), pp. 734–737. DOI: 10.1038/312734a0.

[78] F. Capela, M. Pshirkov, and P. Tinyakov. "Constraints on primordial black holes as dark matter candidates from capture by neutron stars". In: *Phys. Rev. D* 87.12 (2013), p. 123524. DOI: 10.1103/PhysRevD.87.123524.

[79] C. Alcock, E. Farhi, and A. Olinto. "Strange stars". In: *Astrophys.J.* 310 (1986), pp. 261–272. DOI: 10.1086/164679.

[80] 0. F. Navarro, C. S. Frenk, and S. D. M. White. "The Structure of cold dark matter halos". In: *Astrophys. J.* 462 (1996), pp. 563–575. DOI: 10.1086/177173.

[81] 0. F. Navarro, C. S. Frenk, and S. D. M. White. "A Universal density profile from hierarchical clustering". In: *Astrophys. J.* 490 (1997), pp. 493–508. DOI: 10.1086/304888.

[82] R. A. Flores and J. R. Primack. "Observational and theoretical constraints on singular dark matter halos". In: *Astrophys. J. Lett.* 427 (1994), pp. L1–4. DOI: 10.1086/187350.

[83] B. Moore. "Evidence against dissipation-less dark matter from observations of galaxy haloes". In: *Nature* 370.6491 (Aug. 1994), pp. 629–631. DOI: 10.1038/370629a0.

[84] A. Burkert. "The Structure of dark matter halos in dwarf galaxies". In: *Astrophys. J. Lett.* 447 (1995), p. L25. DOI: 10.1086/309560.

[85] S. S. McGaugh and W. J. G. de Blok. "Testing the Dark Matter Hypothesis with Low Surface Brightness Galaxies and Other Evidence". In: *The Astrophysical Journal* 499.1 (May 1998), pp. 41–65. DOI: 10.1086/305612.

[86] F. C. van den Bosch and R. A. Swaters. "Dwarf galaxy rotation curves and the core problem of dark matter halos". In: *Mon. Not. Roy. Astron. Soc.* 325 (2001), p. 1017. DOI: 10.1046/j.1365-8711.2001.04456.x.

[87] A. Borriello and P. Salucci. "The Dark matter distribution in disk galaxies". In: *Mon. Not. Roy. Astron. Soc.* 323 (2001), p. 285. DOI: 10.1046/j.1365-8711.2001.04077.x.

[88] W. J. G. de Blok et al. "Mass density profiles of LSB galaxies". In: *Astrophys. J. Lett.* 552 (2001), pp. L23–L26. DOI: 10.1086/320262.

[89] D. Marchesini et al. "Halpha rotation curves: the soft core question". In: *Astrophys. J.* 575 (2002), pp. 801–813. DOI: 10.1086/341475.

[90] G. Gentile et al. "The dwarf galaxy DDO 47 as a dark matter laboratory: testing cusps hiding in triaxial halos". In: *Astrophys. J. Lett.* 634 (2005), pp. L145–L148. DOI: 10.1086/498939.

[91] G. Gentile et al. "NGC 3741: Dark halo profile from the most extended rotation curve". In: *Mon. Not. Roy. Astron. Soc.* 375 (2007), pp. 199–212. DOI: 10.1111/j.1365-2966.2006.11283.x.

[92] R. Kuzio de Naray et al. "High Resolution Optical Velocity Fields of 11 Low Surface Brightness Galaxies". In: *Astrophys. J. Suppl.* 165 (2006), pp. 461–479. DOI: 10.1086/505345.

[93] P. Salucci et al. "The Universal Rotation Curve of Spiral Galaxies. 2. The Dark Matter Distribution out to the Virial Radius". In: *Mon. Not. Roy. Astron. Soc.* 378 (2007), pp. 41–47. DOI: 10.1111/j.1365-2966.2007.11696.x.

[94] G. Kauffmann, S. D. M. White, and B. Guiderdoni. "The formation and evolution of galaxies within merging dark matter haloes". In: *Monthly Notices of the Royal Astronomical Society* 264.1 (Sept. 1993), pp. 201–218. DOI: 10.1093/mnras/264.1.201.

[95] B. Moore et al. "Dark matter substructure within galactic halos". In: *Astrophys. J. Lett.* 524 (1999), pp. L19–L22. DOI: 10.1086/312287.

[96] A. A. Klypin et al. "Where are the missing Galactic satellites?" In: *Astrophys. J.* 522 (1999), pp. 82–92. DOI: 10.1086/307643.

[97] J. S. Bullock et al. "Profiles of dark haloes. Evolution, scatter, and environment". In: *Mon. Not. Roy. Astron. Soc.* 321 (2001), pp. 559–575. DOI: 10.1046/j.1365-8711.2001.04068.x.

[98] K. A. Oman et al. "The unexpected diversity of dwarf galaxy rotation curves". In: *Mon. Not. Roy. Astron. Soc.* 452.4 (2015), pp. 3650–3665. DOI: 10.1093/mnras/stv1504.

[99] S. Tulin and H.-B. Yu. "Dark Matter Self-interactions and Small Scale Structure". In: *Phys. Rept.* 730 (2018), pp. 1–57. DOI: 10.1016/j.physrep.2017.11.004.

[100] A. Di Cintio et al. "The dependence of dark matter profiles on the stellar-to-halo mass ratio: a prediction for cusps versus cores". In: *Monthly Notices of the Royal Astronomical Society* 437.1 (Nov. 2013), pp. 415–423. DOI: 10.1093/mnras/stt1891.

[101] E. Tollet et al. "NIHAO - IV: core creation and destruction in dark matter density profiles across cosmic time". In: *Monthly Notices of the Royal Astronomical Society* 456.4 (Jan. 2016), pp. 3542–3552. DOI: 10.1093/mnras/stv2856.

[102] A. Lazar et al. "A dark matter profile to model diverse feedback-induced core sizes of ΛCDM haloes". In: *Monthly Notices of the Royal Astronomical Society* 497.2 (Sept. 2020), pp. 2393–2417. DOI: 10.1093/mnras/staa2101.

[103] P. F. Hopkins et al. "Galaxies on FIRE (Feedback In Realistic Environments): stellar feedback explains cosmologically inefficient star formation". In: *Monthly Notices of the Royal Astronomical Society* 445.1 (Sept. 2014), pp. 581–603. DOI: 10.1093/mnras/stu1738.

[104] P. F. Hopkins et al. "FIRE-2 simulations: physics versus numerics in galaxy formation". In: *Monthly Notices of the Royal Astronomical Society* 480.1 (Oct. 2018), pp. 800–863. DOI: 10.1093/mnras/sty1690.

[105] S. Lu et al. "A comparison of pre-existing ΛCDM predictions with the abundance of JWST galaxies at high redshift". In: *Monthly Notices of the Royal Astronomical Society* 536.1 (Nov. 2024), pp. 1018–1034. DOI: 10.1093/mnras/stae2646.

[106] S. Adhikari et al. "Astrophysical Tests of Dark Matter Self-Interactions". In: (July 2022).

[107] M. Colpi, S. L. Shapiro, and I. Wasserman. "Boson Stars: Gravitational Equilibria of Selfinteracting Scalar Fields". In: *Phys. Rev. Lett.* 57 (1986), pp. 2485–2488. DOI: 10.1103/PhysRevLett.57.2485.

[108] I. Goldman and S. Nussi11. "Weakly interacting massive particles and neutron stars". In: *Phys. Rev. D* 40 (10 Nov. 1989), pp. 3221–3230. DOI: 10.1103/PhysRevD.40.3221.

[109] D. R. Karkevandi et al. "Bosonic dark matter in neutron stars and its effect on gravitational wave signal". In: *Phys. Rev. D* 105.2 (2022), p. 023001. DOI: 10.1103/PhysRevD.105.023001.

[110] A. E. Nelson, S. Reddy, and D. Zhou. "Dark halos around neutron stars and gravitational waves". In: *Journal of Cosmology and Astroparticle Physics* 2019.07 (July 2019), p. 012. DOI: 10.1088/1475-7516/2019/07/012.

[111] J. Ellis et al. "Dark matter effects on neutron star properties". In: *Phys. Rev. D* 97 (12 June 2018), p. 123007. DOI: 10.1103/PhysRevD.97.123007.

[112] I. Goldman et al. "Possible implications of asymmetric fermionic dark matter for neutron stars". In: *Physics Letters B* 725.4 (2013), pp. 200–207. DOI: 10.1016/j.physletb.2013.07.017.

[113] M. Deliyergiyev et al. "Dark compact objects: An extensive overview". In: *Phys. Rev. D* 99 (6 Mar. 2019), p. 063015. DOI: 10.1103/PhysRevD.99.063015.

[114] A. Li, F. Huang, and R.-X. Xu. "Too massive neutron stars: The role of dark matter?" In: *Astroparticle Physics* 37 (2012), pp. 70–74. DOI: 10.1016/j.astropartphys.2012.07.006.

[115] F. Sandin and P. Ciarcelluti. "Effects of mirror dark matter on neutron stars". In: *Astroparticle Physics* 32.5 (2009), pp. 278–284. DOI: 10.1016/j.astropartphys.2009.09.005.

[116] A. Del Popolo, M. Le Delliou, and M. Deliyergiyev. "Neutron Stars and Dark Matter". In: *Universe* 6.12 (2020). DOI: 10.3390/universe6120222.

[117] A. Del Popolo, M. Deliyergiyev, and M. Le Delliou. "Solution to the hyperon puzzle using dark matter". In: *Physics of the Dark Universe* 30 (2020), p. 100622. DOI: 10.1016/j.dark.2020.100622.

[118] S. Profumo, K. Sigurdson, and M. Kamionkowski. "What Mass Are the Smallest Protohalos?" In: *Phys. Rev. Lett.* 97 (3 July 2006), p. 031301. DOI: 10.1103/PhysRevLett.97.031301.

[119] V. Berezinsky, V. Dokuchaev, and Y. Eroshenko. "Formation and internal structure of superdense dark matter clumps and ultracompact minihaloes". In: *Journal of Cosmology and Astroparticle Physics* 2013.11 (Nov. 2013), p. 059. DOI: 10.1088/1475-7516/2013/11/059.

[120] C. Kouvaris and N. G. Nielsen. "Asymmetric Dark Matter Stars". In: *Phys. Rev. D* 92.6 (2015), p. 063526. DOI: 10.1103/PhysRevD.92.063526.

[121] A. Maselli et al. "Dark stars: Gravitational and electromagnetic observables". In: *Phys. Rev. D* 96 (2 July 2017), p. 023005. DOI: 10.1103/PhysRevD.96.023005.

[122] A. Ávila et al. "Rapid neutron star cooling triggered by dark matter". In: *Monthly Notices of the Royal Astronomical Society* 528.4 (Feb. 2024), pp. 6319–6328. DOI: 10.1093/mnras/stae337.

[123] B. X. Zhou et al. "Cooling of dark neutron stars". In: (Aug. 2025).

[124] A. Kumar, H. C. Das, and S. K. Patra. "Thermal relaxation of dark matter admixed neutron star". In: *Monthly Notices of the Royal Astronomical Society* 513.2 (Apr. 2022), pp. 1820–1833. DOI: 10.1093/mnras/stac1013.

[125] E. Giangrandi et al. "The Impact of Asymmetric Dark Matter on the Thermal Evolution of Nucleonic and Hyperonic Compact Stars". In: *Particles* 7.1 (2024), pp. 179–200. DOI: 10.3390/particles7010010.

[126] B. P. Abbott et al. "Properties of the Binary Neutron Star Merger GW170817". In: *Phys. Rev. X* 9 (1 Jan. 2019), p. 011001. DOI: 10.1103/PhysRevX.9.011001.

[127] R.-X. Yang, F. Xie, and D.-0. Liu. "Tidal Deformability of Neutron Stars in Unimodular Gravity". In: *Universe* 8.11 (2022), p. 576. DOI: 10.3390/universe8110576.

[128] B. Kain. "Dark matter admixed neutron stars". In: *Phys. Rev. D* 103 (4 Feb. 2021), p. 043009. DOI: 10.1103/PhysRevD.103.043009.

[129] M. Hempel and J. Schaffner-Bielich. "Statistical Model for a Complete Super11a Equation of State". In: *Nucl. Phys. A* 837 (2010), pp. 210–254. DOI: 10.1016/j.nuclphysa.2010.02.010.

[130] P. Möller, J. R. Nix, and K. .-. Kratz. "Nuclear Properties for Astrophysical and Radioactive-Ion Beam Applications". In: *Atomic Data and Nuclear Data Tables* 66 (Jan. 1997), p. 131. DOI: 10.1006/adnd.1997.0746.

[131] A. W. Steiner, M. Hempel, and T. Fischer. "Core-collapse Super11a Equations of State Based on Neutron Star Observations". In: *The Astrophysical Journal* 774.1, 17 (Sept. 2013), p. 17. DOI: 10.1088/0004-637X/774/1/17.

[132] E. Giangrandi et al. "The Effects of Self-interacting Bosonic Dark Matter on Neutron Star Properties". In: *Astrophys. J.* 953.1 (2023), p. 115. DOI: 10.3847/1538-4357/ace104.

[133] D. J. Kaup. "Klein-Gordon Geon". In: *Phys. Rev.* 172 (5 Aug. 1968), pp. 1331–1342. DOI: 10.1103/PhysRev.172.1331.

[134] R. Ruffini and S. Bonazzola. "Systems of Self-Gravitating Particles in General Relativity and the Concept of an Equation of State". In: *Phys. Rev.* 187 (5 Nov. 1969), pp. 1767–1783. DOI: 10.1103/PhysRev.187.1767.

[135] J. D. Breit, S. Gupta, and A. Zaks. "COLD BOSE STARS". In: *Phys. Lett.* B140 (1984), pp. 329–332. DOI: 10.1016/0370-2693(84)90764-0.

[136] Y. Shnir. "Boson Stars". In: *Lect. Notes Phys.* 1017 (2023), pp. 347–362. DOI: 10.1007/978-3-031-31520-6_10.

[137] F. E. Schunck and E. W. Mielke. "General relativistic boson stars". In: *Classical and Quantum Gravity* 20.20 (Sept. 2003), R301. DOI: 10.1088/0264-9381/20/20/201.

[138] L. Visinelli. "Boson stars and oscillatons: A review". In: *Int. J. Mod. Phys. D* 30.15 (2021), p. 2130006. DOI: 10.1142/S0218271821300068.

[139] J. A. Wheeler. "Geons". In: *Phys. Rev.* 97 (2 Jan. 1955), pp. 511–536. DOI: 10.1103/PhysRev.97.511.

[140] D. A. Feinblum and W. A. McKinley. "Stable States of a Scalar Particle in Its Own Gravational Field". In: *Phys. Rev.* 168 (5 Apr. 1968), pp. 1445–1450. DOI: 10.1103/PhysRev.168.1445.

[141] R. Friedberg, T. D. Lee, and Y. Pang. "Scalar soliton stars and black holes". In: *Phys. Rev. D* 35 (12 June 1987), pp. 3658–3677. DOI: 10.1103/PhysRevD.35.3658.

[142] N. Sennett et al. "Distinguishing boson stars from black holes and neutron stars from tidal interactions in inspiraling binary systems". In: *Phys. Rev. D* 96 (2 July 2017), p. 024002. DOI: 10.1103/PhysRevD.96.024002.

[143] D. Bettoni, M. Colombo, and S. Liberati. "Dark matter as a Bose-Einstein Condensate: the relativistic non-minimally coupled case". In: *JCAP* 02 (2014), p. 004. DOI: 10.1088/1475-7516/2014/02/004.

[144] S. Carignano et al. "Scrutinizing the pion condensed phase". In: *Eur. Phys. J. A* 53.2 (2017), p. 35. DOI: 10.1140/epja/i2017-12221-x.

[145] B. B. Brandt et al. "New class of compact stars: Pion stars". In: *Phys. Rev.* **D** 98 (9 Nov. 2018), p. 094510. DOI: 10.1103/PhysRevD.98.094510.

[146] J. O. Andersen and P. Kneschke. "Bose-Einstein condensation and pion stars". In: ().

[147] M. Mannarelli. "Meson condensation". In: *Particles* 2.3 (2019), pp. 411–443. DOI: 10.3390/particles2030025.

[148] O. S. Stashko et al. "Pion stars embedded in neutrino clouds". In: *Phys. Rev. D* 107.11 (2023), p. 114025. DOI: 10.1103/PhysRevD.107.114025.

[149] H. Georgi. "Weak Interactions and Modern Particle Theory". Benjamin/Cummings Publishing Company, 1984.

[150] M. Peskin and D. Schroeder. "An Introduction to Quantum Field Theory". Advanced book classics. Avalon Publishing, 1995.

[151] M. Prunier et al. "Analysis of the subsolar-mass black hole candidate SSM200308 from the second part of the third observing run of Advanced LIGO-Virgo". 2023.

[152] S. L. Shapiro and S. A. Teukolsky. "Black holes, white dwarfs, and neutron stars: The physics of compact objects". 1983.

[153] F. Douchin and P. Haensel. "A unified equation of state of dense matter and neutron star structure". In: *Astron. Astrophys.* 380 (2001), p. 151. DOI: 10.1051/0004-6361:20011402.

[154] D. Page and S. Reddy. "Dense Matter in Compact Stars: Theoretical Developments and Observational Constraints". In: *Ann. Rev. Nucl. Part. Sci.* 56 (2006), pp. 327–374. DOI: 10.1146/annurev.nucl.56.080805.140600.

[155] D. Blaschke and N. Chamel. "Phases of dense matter in compact stars". In: *Astrophys. Space Sci. Libr.* 457 (2018), pp. 337–400. DOI: 10.1007/978-3-319-97616-7_7.

[156] J. M. Lattimer. "Neutron Stars and the Nuclear Matter Equation of State". In: *Ann. Rev. Nucl. Part. Sci.* 71 (2021), pp. 433–464. DOI: 10.1146/annurev-nucl-102419-124827.

[157] G. F. Burgio et al. "Neutron stars and the nuclear equation of state". In: *Prog. Part. Nucl. Phys.* 120 (2021), p. 103879. DOI: 10.1016/j.ppnp.2021.103879.

[158] M. Colpi, S. L. Shapiro, and S. A. Teukolsky. "Exploding Neutron Stars near the Minimum Mass". In: *The Astrophysical Journal* 339 (Apr. 1989), p. 318. DOI: 10.1086/167299.

[159] K. Strobel, C. Schaab, and M. K. Weigel. "Properties of nonrotating and rapidly rotating protoneutron stars". In: *Astron. Astrophys.* 350 (1999), p. 497.

[160] Y. Suwa et al. "On the minimum mass of neutron stars". In: *Mon. Not. Roy. Astron. Soc.* 481.3 (2018), pp. 3305–3312. DOI: 10.1093/mnras/sty2460.

[161] E. Chabanat et al. "A Skyrme parametrization from subnuclear to neutron star densities Part II. Nuclei far from stabilities". In: *Nuclear Physics A* 635.1 (1998), pp. 231–256. DOI: 10.1016/S0375-9474(98)00180-8.

[162] Bombaci, Ignazio and Logoteta, Domenico. "Equation of state of dense nuclear matter and neutron star structure from nuclear chiral interactions". In: *A&A* 609 (2018), A128. DOI: 10.1051/0004-6361/201731604.

[163] G. Grams et al. "Confronting a set of Skyrme and $\chi - EFT$ predictions for the crust of neutron stars". In: *The European Physical Journal A* 58.3 (Mar. 2022), p. 56. DOI: 10.1140/epja/s10050-022-00706-w.

[164] A. Akmal, V. R. Pandharipande, and D. G. Ravenhall. "Equation of state of nucleon matter and neutron star structure". In: *Phys. Rev. C* 58 (3 Sept. 1998), pp. 1804–1828. DOI: 10.1103/PhysRevC.58.1804.

[165] P. Pani and G. Franciolini. "Private communication".

[166] LIGO. "Public LIGO Document T1500293-v13". URL: https://dcc.ligo.org/LIGO-T1500293/public.

[167] F. Crescimbeni et al. "Primordial black holes or else? Tidal tests on subsolar mass gravitational-wave observations". 2024.

[168] M. Branchesi et al. "Science with the Einstein Telescope: a comparison of different designs". In: *JCAP* 07 (2023), p. 068. DOI: 10.1088/1475-7516/2023/07/068.

[169] S. L. Pitz and J. Schaffner-Bielich. "Generating ultracompact boson stars with modified scalar potentials". In: *Phys. Rev. D* 108.10 (2023), p. 103043. DOI: 10.1103/PhysRevD.108.103043.

[170] B. P. Abbott et al. "Multi-messenger Observations of a Binary Neutron Star Merger". In: *Astrophys. J. Lett.* 848.2 (2017), p. L12. DOI: 10.3847/2041-8213/aa91c9.

[171] E. E. Flanagan and T. Hinderer. "Constraining neutron star tidal Love numbers with gravitational wave detectors". In: *Phys. Rev.* D77 (2008), p. 021502. DOI: 10.1103/PhysRevD.77.021502.

[172] T. Damour and A. Nagar. "Relativistic tidal properties of neutron stars". In: *Phys. Rev. D* 80 (2009), p. 084035. DOI: 10.1103/PhysRevD.80.084035.

[173] G. Bertone et al. "Gravitational wave probes of dark matter: challenges and opportunities". In: *SciPost Phys. Core* 3 (2020), p. 007. DOI: 10.21468/SciPostPhysCore.3.2.007.

[174] J. L. Rosa and D. Rubiera-Garcia. "Shadows of boson and Proca stars with thin accretion disks". In: *Phys. Rev. D* 106.8 (2022), p. 084004. DOI: 10.1103/PhysRevD.106.084004.

[175] C. Palenzuela, L. Lehner, and S. L. Liebling. "Orbital Dynamics of Binary Boson Star Systems". In: *Phys. Rev. D* 77 (2008), p. 044036. DOI: 10.1103/PhysRevD.77.044036.

[176] M. Bezares and C. Palenzuela. "Gravitational Waves from Dark Boson Star binary mergers". In: *Class. Quant. Grav.* 35.23 (2018), p. 234002. DOI: 10.1088/1361-6382/aae87c.

[177] C. Palenzuela et al. "Gravitational wave signatures of highly compact boson star binaries". In: *Phys. Rev. D* 96 (10 Nov. 2017), p. 104058. DOI: 10.1103/PhysRevD.96.104058.

[178] F. Loffler et al. "The Einstein Toolkit: A Community Computational Infrastructure for Relativistic Astrophysics". In: *Class. Quant. Grav.* 29 (2012), p. 115001. DOI: 10.1088/0264-9381/29/11/115001.

[179] Cactus Developers. "Cactus Computational Toolkit". http://www.cactuscode.org/. 2026.

[180] T. Goodale et al. "The Cactus Framework and Toolkit: Design and Applications". In: *Vector and Parallel Processing – VECPAR'2002, 5th International Conference, Lecture Notes in Computer Science*. Lecture Notes in Computer Science. Berlin: Springer, 2003.

[181] E. Schnetter, S. H. Hawley, and I. Hawke. "Evolutions in 3-D numerical relativity using fixed mesh refinement". In: *Class. Quant. Grav.* 21 (2004), pp. 1465–1488. DOI: 10.1088/0264-9381/21/6/014.

[182] M. Shibata and T. Nakamura. "Evolution of three-dimensional gravitational waves: Harmonic slicing case". In: *Phys. Rev. D* 52 (10 Nov. 1995), pp. 5428–5444. DOI: 10.1103/PhysRevD.52.5428.

[183] T. W. Baumgarte and S. L. Shapiro. "Numerical integration of Einstein's field equations". In: *Phys. Rev. D* 59 (2 Dec. 1998), p. 024007. DOI: 10.1103/PhysRevD.59.024007.

[184] McLachlan Developers. "McLachlan, a public BSSN code". http://www.cct.lsu.edu/~eschnett/McLachlan/. Accessed: 2026.

[185] F. Banyuls et al. "Numerical 3 + 1 General Relativistic Hydrodynamics: A Local Characteristic Approach". In: *The Astrophysical Journal* 476.1 (Feb. 1997), p. 221. DOI: 10.1086/303604.

[186] J. A. Font. "Numerical Hydrodynamics and Magnetohydrodynamics in General Relativity". In: *Living Reviews in Relativity* 11.1 (Sept. 2008), p. 7. DOI: 10.12942/lrr-2008-7.

[187] L. Baiotti et al. "Three-dimensional relativistic simulations of rotating neutron star collapse to a Kerr black hole". In: *Phys. Rev.* D71 (2005), p. 024035. DOI: 10.1103/PhysRevD.71.024035.

[188] P. Mösta et al. "GRHydro: A new open source general-relativistic magnetohydrodynamics code for the Einstein Toolkit". In: *Class. Quant. Grav.* 31 (2014), p. 015005. DOI: 10.1088/0264-9381/31/1/015005.

[189] A. Harten, P. D. Lax, and B. van Leer. "On Upstream Differencing and Godu11-Type Schemes for Hyperbolic Conservation Laws". In: *SIAM Rev.* 25 (1983), pp. 35–61.

[190] B. Einfeldt. "On Godu11-Type Methods for Gas Dynamics". In: *SIAM Journal on Numerical Analysis* 25.2 (1988), pp. 294–318. DOI: 10.1137/0725021.

[191] X.-D. Liu, S. Osher, and T. Chan. "Weighted essentially non-oscillatory schemes". In: *Journal of computational physics* 115.1 (1994), pp. 200–212.

[192] G.-S. Jiang and C.-W. Shu. "Efficient implementation of weighted ENO schemes". In: *Journal of computational physics* 126.1 (1996), pp. 202–228.

[193] I. Hinder et al. "Error-analysis and comparison to analytical models of numerical waveforms produced by the NRAR Collaboration". In: *Classical and Quantum Gravity* 31.2 (Jan. 2013), p. 025012. DOI: 10.1088/0264-9381/31/2/025012.

[194] N. Stergioulas et al. "Gravitational waves and non-axisymmetric oscillation modes in mergers of compact object binaries". In: *Monthly Notices of the Royal Astronomical Society* 418.1 (Nov. 2011), pp. 427–436. DOI: 10.1111/j.1365-2966.2011.19493.x.

[195] K. Kyutoku, M. Shibata, and K. Taniguchi. "Reducing orbital eccentricity in initial data of binary neutron stars". In: *Phys. Rev. D* 90 (6 Sept. 2014), p. 064006. DOI: 10.1103/PhysRevD.90.064006.

[196] T. Dietrich et al. "Binary neutron stars with generic spin, eccentricity, mass ratio, and compactness: Quasi-equilibrium sequences and first evolutions". In: *Physical Review D* 92.12 (Dec. 2015). DOI: 10.1103/physrevd.92.124007.

[197] B. Abbott et al. "Prospects for observing and localizing gravitational-wave transients with Advanced LIGO, Advanced Virgo and KAGRA". In: *Living Reviews in Relativity* 23.1 (Sept. 2020), p. 3. DOI: 10.1007/s41114-020-00026-9.

[198] A. Bauswein, N. Stergioulas, and H.-T. Janka. "Exploring properties of high-density matter through remnants of neutron-star mergers". In: *The European Physical Journal A* 52.3 (Mar. 2016), p. 56. DOI: 10.1140/epja/i2016-16056-7.

[199] A. Bauswein et al. "Equation-of-state dependence of the gravitational-wave signal from the ring-down phase of neutron-star mergers". In: *Phys. Rev. D* 86 (6 Sept. 2012), p. 063001. DOI: 10.1103/PhysRevD.86.063001.

[200] G. Franciolini and P. Pani. In: *Private communication* (2024).

[201] L. Rezzolla and K. Takami. "Gravitational-wave signal from binary neutron stars: a systematic analysis of the spectral properties". In: *Phys. Rev. D* 93.12 (2016), p. 124051. DOI: 10.1103/PhysRevD.93.124051.

[202] F. Banyuls et al. "Numerical {3 + 1} General Relativistic Hydrodynamics: A Local Characteristic Approach". In: *The Astrophysical Journal* 476.1 (Feb. 1997), pp. 221–231. DOI: 10.1086/303604.

[203] G. Bertone and M. Fairbairn. "Compact stars as dark matter probes". In: *Phys. Rev. D* 77 (4 Feb. 2008), p. 043515. DOI: 10.1103/PhysRevD.77.043515.

[204] P. Ciarcelluti and F. Sandin. "Have neutron stars a dark matter core?" In: *Phys. Lett. B* 695 (2011), pp. 19–21. DOI: 10.1016/j.physletb.2010.11.021.

[205] X. Li, F. Wang, and K. S. Cheng. "Gravitational effects of condensate dark matter on compact stellar objects". In: *JCAP* 10 (2012), p. 031. DOI: 10.1088/1475-7516/2012/10/031.

[206] O. Ivanytskyi, V. Sagun, and I. Lopes. "Neutron stars: New constraints on asymmetric dark matter". In: *Phys. Rev. D* 102.6 (2020), p. 063028. DOI: 10.1103/PhysRevD.102.063028.

[207] H. C. Das et al. "Effects of dark matter on the nuclear and neutron star matter". In: *Mon. Not. Roy. Astron. Soc.* 495 (2020), pp. 4893–4903. DOI: 10.1093/mnras/staa1435.

[208] Z. Berezhiani et al. "Neutron-mirror neutron mixing and neutron stars". In: *Eur. Phys. J. C* 81.11 (2021), p. 1036. DOI: 10.1140/epjc/s10052-021-09806-1.

[209] S. Shakeri and D. R. Karkevandi. "Bosonic dark matter in light of the NICER precise mass-radius measurements". In: *Phys. Rev. D* 109.4 (2024), p. 043029. DOI: 10.1103/PhysRevD.109.043029.

[210] P. Thakur et al. "Exploring robust correlations between fermionic dark matter model parameters and neutron star properties: A two-fluid perspective". In: *Phys. Rev. D* 109.4 (2024), p. 043030. DOI: 10.1103/PhysRevD.109.043030.

[211] F. Dalfovo et al. "Theory of Bose-Einstein condensation in trapped gases". In: *Rev. Mod. Phys.* 71 (1999), pp. 463–512. DOI: 10.1103/RevModPhys.71.463.

[212] B. P. Anderson et al. "Vortex Precession in Bose-Einstein Condensates: Observations with Filled and Empty Cores". In: *Physical Review Letters* 85.14 (Oct. 2000), pp. 2857–2860. DOI: 10.1103/physrevlett.85.2857.

[213] L. Dolan and R. Jackiw. "Symmetry Behavior at Finite Temperature". In: *Phys. Rev. D* 9 (1974), pp. 3320–3341. DOI: 10.1103/PhysRevD.9.3320.

[214] H. T. C. Stoof. "Nucleation of Bose-Einstein condensation". In: *Phys. Rev. A* 45 (1992), pp. 8398–8406. DOI: 10.1103/PhysRevA.45.8398.

[215] P. Grüter, D. Ceperley, and F. Laloë. "Critical Temperature of Bose-Einstein Condensation of Hard-Sphere Gases". In: *Phys. Rev. Lett.* 79.19 (Nov. 1997), pp. 3549–3552. DOI: 10.1103/PhysRevLett.79.3549.

[216] S. Jeon and L. G. Yaffe. "From quantum field theory to hydrodynamics: Transport coefficients and effective kinetic theory". In: *Phys. Rev. D* 53 (10 May 1996), pp. 5799–5809. DOI: 10.1103/PhysRevD.53.5799.

[217] D. N. Spergel and P. J. Steinhardt. "Observational evidence for selfinteracting cold dark matter". In: *Phys. Rev. Lett.* 84 (2000), pp. 3760–3763. DOI: 10.1103/PhysRevLett.84.3760.

[218] A. Ianni, M. Mannarelli, and N. Rossi. "A new approach to dark matter from the mass–radius diagram of the Universe". In: *Results Phys.* 38 (2022), p. 105544. DOI: 10.1016/j.rinp.2022.105544.

[219] F. Nesti, P. Salucci, and N. Turini. "The Quest for the Nature of the Dark Matter: The Need of a New Paradigm". In: *Astronomy* 2.2 (2023), pp. 90–104. DOI: 10.3390/astronomy2020007.

[220] G. Ferioli et al. "Collisions of Self-Bound Quantum Droplets". In: *Phys. Rev. Lett.* 122 (9 Mar. 2019), p. 090401. DOI: 10.1103/PhysRevLett.122.090401.

[221] M. A. Norcia et al. "Two-dimensional supersolidity in a dipolar quantum gas". In: *Nature* 596.7872 (2021), pp. 357–361.

[222] T. Bland et al. "Two-Dimensional Supersolid Formation in Dipolar Condensates". In: *Physical Review Letters* 128.19 (2022), p. 195302.

[223] M. A. Norcia et al. "Can Angular Oscillations Probe Superfluidity in Dipolar Supersolids?" In: *Phys. Rev. Lett.* 129 (4 July 2022), p. 040403. DOI: 10.1103/PhysRevLett.129.040403.

[224] L. Klaus et al. "Observation of vortices and vortex stripes in a dipolar condensate". In: *Nature Physics* 18.12 (2022), pp. 1453–1458.

[225] E. Poli et al. "Glitches in Rotating Supersolids". In: *Phys. Rev. Lett.* 131.22 (2023), p. 223401. DOI: 10.1103/PhysRevLett.131.223401.

[226] W. Baade and F. Zwicky. "On super-11ae". In: *Proceedings of the National Academy of Sciences* 20.5 (1934), pp. 254–259.

[227] D. C. Backer et al. "A millisecond pulsar". In: *Nature* 300.5893 (Dec. 1982), pp. 615–618. DOI: 10.1038/300615a0.

[228] J. W. T. Hessels et al. "A radio pulsar spinning at 716-hz". In: *Science* 311 (2006), pp. 1901–1904. DOI: 10.1126/science.1123430.

[229] G. K. Jaisawal et al. "A Comprehensive Study of Thermonuclear X-ray Bursts from 4U 1820-30 with NICER: Accretion Disk Interactions and a Candidate Burst Oscillation". In: *Astrophys. J.* 975.1 (2024), p. 67. DOI: 10.3847/1538-4357/ad794e.

[230] D. Bhattacharya and E. P. J. van den Heuvel. "Formation and evolution of binary and millisecond radio pulsars". In: *Phys. Rep.* 203.1-2 (1991), pp. 1–124. DOI: 10.1016/0370-1573(91)90064-S.

[231] R. Wijnands and M. van der Klis. "A millisecond pulsar in an X-ray binary system". In: *Nature* 394.6691 (July 1998), pp. 344–346. DOI: 10.1038/28557.

[232] S. Guillot et al. "NICER X-ray Observations of Seven Nearby Rotation-Powered Millisecond Pulsars". In: *Astrophys. J. Lett.* 887.1 (2019), p. L27. DOI: 10.3847/2041-8213/ab511b.

[233] C. Kouvaris and P. Tinyakov. "Can neutron stars constrain dark matter?" In: *Phys. Rev. D* 82 (6 Sept. 2010), p. 063531. DOI: 10.1103/PhysRevD.82.063531.

[234] N. F. Bell et al. "Nucleon Structure and Strong Interactions in Dark Matter Capture in Neutron Stars". In: *Phys. Rev. Lett.* 127.11 (2021), p. 111803. DOI: 10.1103/PhysRevLett.127.111803.

[235] Z. Miao et al. "Dark Matter Admixed Neutron Star Properties in the Light of X-ray Pulse Profile Observations". In: *The Astrophysical Journal* 936.1, 69 (Sept. 2022), p. 69. DOI: 10.3847/1538-4357/ac8544.

[236] N. Rutherford et al. "Constraining bosonic asymmetric dark matter with neutron star mass-radius measurements". In: *Phys. Rev. D* 107.10 (2023), p. 103051. DOI: 10.1103/PhysRevD.107.103051.

[237] S. Shawqi and S. M. Morsink. "Interpreting Mass and Radius Measurements of Neutron Stars with Dark Matter Halos". In: *Astrophys. J.* 975.1 (2024), p. 123. DOI: 10.3847/1538-4357/ad77c1.

[238] Y. Liu et al. "Effects from dark matter halos on X-ray pulsar pulse profiles". In: *Phys. Rev. D* 110.8 (2024), p. 083018. DOI: 10.1103/PhysRevD.110.083018.

[239] M. Bezares, D. Viganò, and C. Palenzuela. "Gravitational wave signatures of dark matter cores in binary neutron star mergers by using numerical simulations". In: *Phys. Rev. D* 100.4 (2019), p. 044049. DOI: 10.1103/PhysRevD.100.044049.

[240] A. Bauswein et al. "Compact dark objects in neutron star mergers". In: *Phys. Rev. D* 107.8 (2023), p. 083002. DOI: 10.1103/PhysRevD.107.083002.

[241] F. Di Giovanni et al. "Impact of ultralight bosonic dark matter on the dynamical bar-mode instability of rotating neutron stars". In: *Phys. Rev. D* 106.4 (2022), p. 044008. DOI: 10.1103/PhysRevD.106.044008.

[242] M. Emma et al. "Numerical Simulations of Dark Matter Admixed Neutron Star Binaries". In: *Particles* 5.3 (2022), pp. 273–286. DOI: 10.3390/particles5030024.

[243] H. R. Rüter et al. "Quasiequilibrium configurations of binary systems of dark matter admixed neutron stars". In: *Phys. Rev. D* 108.12 (2023), p. 124080. DOI: 10.1103/PhysRevD.108.124080.

[244] P. Routaray et al. "12oding dark matter admixed neutron stars: From static structure to rotational deformation". In: *Phys. Dark Univ.* 50 (2025), p. 102093. DOI: 10.1016/j.dark.2025.102093.

[245] J. Cronin, X. Zhang, and B. Kain. "Rotating dark matter admixed neutron stars". In: *Phys. Rev. D* 108.10 (2023), p. 103016. DOI: 10.1103/PhysRevD.108.103016.

[246] A. Konstantinou. "The Effect of a Dark Matter Core on the Structure of a Rotating Neutron Star". In: *Astrophys. J.* 968.2 (2024), p. 83. DOI: 10.3847/1538-4357/ad4701.

[247] J. C. Mourelle et al. "Rotating fermion-boson stars". In: *Phys. Rev. D* 110.12 (2024), p. 123019. DOI: 10.1103/PhysRevD.110.123019.

[248] C. W. Misner, K. S. Thorne, and J. A. Wheeler. "Gravitation". San Francisco: W. H. Freeman, 1973. Chap. 20.

[249] S. C. Leung, M. C. Chu, and L. M. Lin. "Equilibrium Structure and Radial Oscillations of Dark Matter Admixed Neutron Stars". In: *Phys. Rev. D* 85 (2012), p. 103528. DOI: 10.1103/PhysRevD.85.103528.

[250] N. Andersson and G. L. Comer. "Slowly rotating general relativistic superfluid neutron stars". In: *Class. Quant. Grav.* 18 (2001), pp. 969–1002. DOI: 10.1088/0264-9381/18/6/302.

[251] R. Prix, J. 11ak, and G. L. Comer. "Relativistic numerical models for stationary superfluid neutron stars". In: *Phys. Rev. D* 71 (2005), p. 043005. DOI: 10.1103/PhysRevD.71.043005.

[252] V. Paschalidis and N. Stergioulas. "Rotating stars in relativity". In: *Living Reviews in Relativity* 20.1 (Nov. 2017), p. 7. DOI: 10.1007/s41114-017-0008-x.

[253] S. C. Leung, M. C. Chu, and L. M. Lin. "Dark-matter admixed neutron stars". In: *Phys. Rev. D* 84 (2011), p. 107301. DOI: 10.1103/PhysRevD.84.107301.

[254] J. Frieben and L. Rezzolla. "Equilibrium models of relativistic stars with a toroidal magnetic field". In: *Mon.Not.Roy.Astron.Soc.* 427 (2012), pp. 3406–3426. DOI: 10.1111/j.1365-2966.2012.22027.x.

[255] J. M. Lattimer and B. F. Schutz. "Constraining the equation of state with moment of inertia measurements". In: *Astrophys. J.* 629 (2005), pp. 979–984. DOI: 10.1086/431543.

[256] G. Camelio et al. "Rotating neutron stars with nonbarotropic thermal profile". In: *Phys. Rev. D* 100.12 (2019), p. 123001. DOI: 10.1103/PhysRevD.100.123001.

[257] G. Camelio et al. "Axisymmetric models for neutron star merger remnants with realistic thermal and rotational profiles". In: *Phys. Rev. D* 103.6 (2021), p. 063014. DOI: 10.1103/PhysRevD.103.063014.

[258] P. Iosif and N. Stergioulas. "Models of binary neutron star remnants with tabulated equations of state". In: *Mon. Not. Roy. Astron. Soc.* 510.2 (2022). [Erratum: Mon.Not.Roy.Astron.Soc. 517, 1601 (2022)], pp. 2948–2967. DOI: 10.1093/mnras/stab3565.

[259] M. Cassing and L. Rezzolla. "Realistic models of general-relativistic differentially rotating stars". In: *Mon. Not. Roy. Astron. Soc.* 532.1 (2024), pp. 945–964. DOI: 10.1093/mnras/stae1527.

[260] L. Cipriani et al. "Superfluid dark stars". In: *Phys. Rev. D* 110.2 (2024), p. L021301. DOI: 10.1103/PhysRevD.110.L021301.

[261] D. N. Spergel. "The Motion of the Earth and the Detection of Wimps". In: *Phys. Rev. D* 37 (1988), p. 1353. DOI: 10.1103/PhysRevD.37.1353.

[262] E. Giangrandi et al. "Numerical Relativity Simulations of Dark Matter Admixed Binary Neutron Stars". In: (Apr. 2025).

[263] A. Watts et al. "Probing the neutron star interior and the Equation of State of cold dense matter with the SKA". In: *PoS* AASKA14 (2015). Ed. by T. L. Bourke et al., p. 043. DOI: 10.22323/1.215.0043.

[264] A. Bauswein et al. "Neutron-star radius constraints from GW170817 and future detections". In: *Astrophys. J. Lett.* 850.2 (2017), p. L34. DOI: 10.3847/2041-8213/aa9994.

[265] D. Radice et al. "GW170817: Joint Constraint on the Neutron Star Equation of State from Multimessenger Observations". In: *Astrophys. J.* 852.2 (2018), p. L29. DOI: 10.3847/2041-8213/aaa402.

[266] M. Shibata and K. Uryū. "Simulation of merging binary neutron stars in full general relativity: Gamma = two case". In: *Phys. Rev. D* 61 (2000), p. 064001. DOI: 10.1103/PhysRevD.61.064001.

[267] L. Baiotti and L. Rezzolla. "Binary neutron star mergers: a review of Einstein's richest laboratory". In: *Rept. Prog. Phys.* 80.9 (2017), p. 096901. DOI: 10.1088/1361-6633/aa67bb.

[268] T. W. Baumgarte, S. L. Shapiro, and M. Shibata. "On the maximum mass of differentially rotating neutron stars". In: *Astrophys. J. Lett.* 528 (2000), p. L29. DOI: 10.1086/312425.

[269] H. Komatsu, Y. Eriguchi, and I. Hachisu. "Rapidly rotating general relativistic stars – II. Differentially rotating polytropes". In: *MNRAS* 239.1 (July 1989), pp. 153–171. DOI: 10.1093/mnras/239.1.153.

[270] W. Kastaun and F. Galeazzi. "Properties of hypermassive neutron stars formed in mergers of spinning binaries". In: *Phys. Rev. D* 91 (6 Mar. 2015), p. 064027. DOI: 10.1103/PhysRevD.91.064027.

[271] M. Hanauske et al. "Rotational properties of hypermassive neutron stars from binary mergers". In: *Phys. Rev. D* 96 (4 Aug. 2017), p. 043004. DOI: 10.1103/PhysRevD.96.043004.

[272] R. Ciolfi et al. "General relativistic magnetohydrodynamic simulations of binary neutron star mergers forming a long-lived neutron star". In: *Phys. Rev. D* 95 (6 Mar. 2017), p. 063016. DOI: 10.1103/PhysRevD.95.063016.

[273] R. De Pietri et al. "Convective Excitation of Inertial Modes in Binary Neutron Star Mergers". In: *Phys. Rev. Lett.* 120 (22 May 2018), p. 221101. DOI: 10.1103/PhysRevLett.120.221101.

[274] W. E. East et al. "Binary neutron star mergers: Effects of spin and post-merger dynamics". In: *Phys. Rev. D* 100 (12 Dec. 2019), p. 124042. DOI: 10.1103/PhysRevD.100.124042.

[275] K. Takami, L. Rezzolla, and L. Baiotti. "Spectral properties of the post-merger gravitational-wave signal from binary neutron stars". In: *Phys. Rev. D* 91 (6 Mar. 2015), p. 064001. DOI: 10.1103/PhysRevD.91.064001.

[276] A. Passamonti and N. Andersson. "Merger-inspired rotation laws and the low-T/W instability in neutron stars". In: *Monthly Notices of the Royal Astronomical Society* 498.4 (Sept. 2020), pp. 5904–5915. DOI: 10.1093/mnras/staa2725.

[277] L. R. Weih, M. Hanauske, and L. Rezzolla. "Postmerger Gravitational-Wave Signatures of Phase Transitions in Binary Mergers". In: *Phys. Rev. Lett.* 124 (17 Apr. 2020), p. 171103. DOI: 10.1103/PhysRevLett.124.171103.

[278] J. Bramante et al. "Bounds on self-interacting fermion dark matter from observations of old neutron stars". In: *Phys. Rev. D* 89 (1 Jan. 2014), p. 015010. DOI: 10.1103/PhysRevD.89.015010.

[279] N. F. Bell et al. "Improved Treatment of Dark Matter Capture in Neutron Stars". In: *JCAP* 09 (2020), p. 028. DOI: 10.1088/1475-7516/2020/09/028.

[280] M. Stref and 0. Lavalle. "Modeling dark matter subhalos in a constrained galaxy: Global mass and boosted annihilation profiles". In: *Phys. Rev. D* 95.6 (2017), p. 063003. DOI: 10.1103/PhysRevD.95.063003.

[281] T. Lacroix. "Dynamical constraints on a dark matter spike at the Galactic Centre from stellar orbits". In: *Astron. Astrophys.* 619 (2018), A46. DOI: 10.1051/0004-6361/201832652.

[282] A. Del Popolo and M. Le Delliou. "Review of Solutions to the Cusp-Core Problem of the ΛCDM Model". In: *Galaxies* 9.4 (2021), p. 123. DOI: 10.3390/galaxies9040123.

[283] A. Suárez, V. H. Robles, and T. Matos. "A Review on the Scalar Field/Bose-Einstein Condensate Dark Matter Model". In: *Astrophys. Space Sci. Proc.* 38 (2014). Ed. by C. Moreno González, J. E. Madriz Aguilar, and L. M. Reyes Barrera, pp. 107–142. DOI: 10.1007/978-3-319-02063-1_9.

[284] M. Hippert et al. "Dark matter or regular matter in neutron stars? How to tell the difference from the coalescence of compact objects". In: *Phys. Rev. D* 107.11 (2023), p. 115028. DOI: 10.1103/PhysRevD.107.115028.

[285] H.-M. Liu et al. "Dark matter effects on the properties of neutron stars: Compactness and tidal deformability". In: *Phys. Rev. D* 110.2 (2024), p. 023024. DOI: 10.1103/PhysRevD.110.023024.

[286] H. Koehn et al. "Impact of dark matter on tidal signatures in neutron star mergers with the Einstein Telescope". In: *Phys. Rev. D* 110.10 (2024), p. 103033. DOI: 10.1103/PhysRevD.110.103033.

[287] L. Cipriani et al. "Rapidly spinning dark matter-admixed neutron stars". In: *Phys. Rev. D* 111.12 (2025), p. 123005. DOI: 10.1103/qcl7-m5kf.

[288] A. Abac et al. "The Science of the Einstein Telescope". In: (Mar. 2025).

[289] G. Bozzola, N. Stergioulas, and A. Bauswein. "Universal relations for differentially rotating relativistic stars at the threshold to collapse". In: *Mon. Not. Roy. Astron. Soc.* 474.3 (2018), pp. 3557–3564. DOI: 10.1093/mnras/stx3002.

[290] L. R. Weih, E. R. Most, and L. Rezzolla. "On the stability and maximum mass of differentially rotating relativistic stars". In: *Mon. Not. Roy. Astron. Soc.* 473.1 (2018), pp. L126–L130. DOI: 10.1093/mnrasl/slx178.

[291] R. Ciolfi et al. "Multi-messenger astrophysics with THESEUS in the 2030s". In: *Experimental Astronomy* 52.3 (Dec. 2021), pp. 245–275. DOI: 10.1007/s10686-021-09795-9.

[292] P. Rosati et al. "Synergies of THESEUS with the large facilities of the 2030s and guest observer opportunities". In: *Experimental Astronomy* 52.3 (Dec. 2021), pp. 407–437. DOI: 10.1007/s10686-021-09764-2.

[293] A. B. Henriques, A. R. Liddle, and R. G. Moorhouse. "Combined Boson - Fermion Stars: Configurations and Stability". In: *Nucl. Phys. B* 337 (1990), pp. 737–761. DOI: 10.1016/0550-3213(90)90514-E.

[294] J. C. Mourelle, N. Sanchis-Gual, and J. A. Font. "Differentially rotating fermion-boson stars". Manuscript in preparation. 2025.

[295] D. Gondek-Rosińska et al. "A New View on the Maximum Mass of Differentially Rotating Neutron Stars". In: *The Astrophysical Journal* 837.1, 58 (Mar. 2017), p. 58. DOI: 10.3847/1538-4357/aa56c1.

[296] K. Takami, L. Rezzolla, and S. Yoshida. "A quasi-radial stability criterion for rotating relativistic stars". In: *Mon. Not. Roy. Astron. Soc.* 416 (2011), pp. L1–L5. DOI: 10.1111/j.1745-3933.2011.01085.x.

[297] P. Szewczyk, D. Gondek-Rosińska, and P. Cerdá-Durán. "Dynamical Stability of Hypermassive Neutron Stars against Quasi-radial Perturbations". In: *Astrophys. J.* 990.2 (2025), p. 199. DOI: 10.3847/1538-4357/adee12.

[298] D. Rafiei Karkevandi et al. "Tidal deformability as a probe of dark matter in neutron stars". In: *16th Marcel Grossmann Meeting on Recent Developments in Theoretical and Experimental General Relativity, Astrophysics and Relativistic Field Theories*. Dec. 2021. DOI: 10.1142/9789811269776_0307.

[299] R. De Pietri et al. "Numerical-relativity simulations of long-lived remnants of binary neutron star mergers". In: *Phys. Rev. D* 101.6 (2020), p. 064052. DOI: 10.1103/PhysRevD.101.064052.

[300] C. G. Broyden. "A class of methods for solving nonlinear simultaneous equations". In: *Mathematics of Computation* 19.92 (1965), pp. 577–593. DOI: 10.1090/s0025-5718-1965-0198670-6.